The Impact of Primary Marine Aerosol on Atmospheric Chemistry, Radiation and Climate: A CCSM Model Development Study

Applicant/Institution: University of Virginia
Dept. of Environmental Sciences

Address: Clark Hall
291 McCormick Rd
PO Box 400123
Charlottesville, VA 22904-4123

Principal Investigator: William C. Keene

Address: Dept. of Environmental Sciences
Clark Hall
291 McCormick Rd
PO Box 400123
University of Virginia
Charlottesville, VA 22904-4123

Telephone Number: (434) 924-0586

E-mail: wck@virginia.edu

DOE/Office of Science Program Office: Biological & Environmental Research

Abstract: This project examined the potential large-scale influence of marine aerosol cycling on atmospheric chemistry, physics and radiative transfer. Measurements indicate that the size-dependent generation of marine aerosols by wind waves at the ocean surface and the subsequent production and cycling of halogen-radicals are important but poorly constrained processes that influence climate regionally and globally. A reliable capacity to examine the role of marine aerosol in the global-scale atmospheric system requires that the important size-resolved chemical processes be treated explicitly. But the treatment of multiphase chemistry across the breadth of chemical scenarios encountered throughout the atmosphere is sensitive to the initial conditions and the precision of the solution method. This study examined this sensitivity, constrained it using high-resolution laboratory and field measurements, and deployed it in a coupled chemical-microphysical 3-D atmosphere model. First, laboratory measurements of fresh, unreacted marine aerosol were used to formulate a sea-state based marine aerosol source parameterization that captured the initial organic, inorganic, and physical conditions of the aerosol population. Second, a multiphase chemical mechanism, solved using the Max Planck Institute for Chemistry's MECCA (Module Efficiently Calculating the Chemistry of the Atmosphere) system, was benchmarked across a broad set of observed chemical and physical conditions in the marine atmosphere. Using these results, the mechanism was systematically reduced to maximize computational speed. Finally, the mechanism was coupled to the 3-mode modal aerosol version of the NCAR Community Atmosphere Model (CAM v3.6.33). Decadal-scale simulations with CAM v.3.6.33, were run both with and without reactive-halogen chemistry and with and without explicit treatment of particulate organic carbon in the marine aerosol source function. Simulated results were interpreted (1) to evaluate influences of marine aerosol production on the microphysical properties of aerosol populations and clouds over the ocean and the corresponding direct and indirect effects on radiative transfer; (2) atmospheric burdens of reactive halogen species and their impacts on O_3, NO_x, OH, DMS, and particulate non-sea-salt SO_4^{2-}; and (3) the global production and influences of marine-derived particulate organic carbon. The model reproduced major characteristics of the marine aerosol system and demonstrated the potential sensitivity of global, decadal-scale climate metrics to multiphase marine-derived components of Earth's troposphere. Due to the combined computational burden of the coupled system, the currently available computational resources were the limiting factor preventing the adequate statistical analysis of the overall impact that multiphase chemistry might have on climate-scale radiative transfer and climate.

This document is organized into two parts representing two project phases: (1) System development & testing, and (2) model results.

1 Part 1: Implementation of the chemistry module MECCA (v2.5) in the modal aerosol version of

2 the Community Atmosphere Model component (v3.6.33) of the Community Earth System Model

3

4 M.S. Long (mlong@seas.harvard.edu)

5   School of Engineering and Applied Sciences, Harvard University, Cambridge, MA, USA

6 W.C. Keene (wck@virginia.edu)

7   Department of Environmental Sciences, University of Virginia, Charlottesville, VA

8 22904, USA

9 R. Easter (Richard.Easter@pnnl.gov)

10   Atmospheric Sciences and Global Change Division, Pacific Northwest National

11 Laboratory

12 R. Sander (rolf.sander@mpic.de)

13   Air Chemistry Department, Max-Planck Institute of Chemistry, 55020 Mainz, Germany

14 A. Kerkweg (astrid.kerkweg@uni-mainz.de)

15   Institute for Atmospheric Physics, University of Mainz, 55099 Mainz, Germany

16 D. Erickson (ericksondj@ornl.gov)

17   Computer Science and Mathematics Division, Oak Ridge National Laboratory,

18   Oak Ridge, TN USA

19 X. Liu (xiaohong.liu@pnnl.gov)

20   Atmospheric Science and Global Change Division, Pacific Northwest National

21 Laboratory,

22   Richland, Washington, USA

23 S. Ghan (Steve.Ghan@pnnl.gov)

24   Atmospheric Science and Global Change Division, Pacific Northwest National

25 Laboratory,

26   Richland, Washington, USA

27

28 Abstract

29   A coupled atmospheric chemistry and climate system model was developed using the modal

30 aerosol version of the National Center for Atmospheric Research Community Atmosphere

31 Model (modal-CAM; v3.6.33) and the Max Planck Institute for Chemistry's Module Efficiently

32 Calculating the Chemistry of the Atmosphere (MECCA; v2.5) to provide enhanced resolution of

33 multiphase processes, particularly those involving inorganic halogens, and associated impacts on

34 atmospheric composition and climate. Three Rosenbrock solvers (Ros-2, Ros-3, RODAS-3)

35 were tested in conjunction with the basic load balancing options available to modal CAM (1) to

36 establish an optimal configuration of the implicitly-solved multiphase chemistry module that

37 maximizes both computational speed and repeatability of Ros-2 and RODAS-3 results versus

38 Ros-3, and (2) to identify potential implementation strategies for future versions of this and

39 similar coupled systems. RODAS-3 was faster than Ros-2 and Ros-3 with good reproduction of

40 Ros-3 results, while Ros-2 was both slower and substantially less reproducible relative to Ros-3

41 results. Modal-CAM with MECCA chemistry was a factor of 15 slower than modal-CAM using

42 standard chemistry. MECCA chemistry integration times demonstrated a systematic frequency

43 distribution for all three solvers, and revealed that the change in run-time performance was due

44 to a change in the frequency distribution chemical integration times; the peak frequency was

45 similar for all solvers. This suggests that efficient chemistry-focused load-balancing schemes can

46 be developed that rely on the parameters of this frequency distribution.

1. Introduction

The spatial and temporal resolutions of geophysical modeling systems are increasing rapidly. As a result, the need to more explicitly resolve many of the physical and chemical processes that previously operated below the resolution and within the uncertainty ranges of these modeling systems is increasing accordingly. Individually, the computational skill of physical and chemical systems is high; but the computational needs of these systems in combination with dynamical and geophysical models has made coupled investigations prohibitive. The capabilities of current high-performance computing platforms available to geoscientific modeling are beginning to permit the coupling of these systems for scientific research. Of particular interest are the interactions between atmospheric chemistry and climate, particularly with respect to the implications of multiphase processes for tropospheric composition, clouds, precipitation, and radiative transfer.

Multiphase interactions, primarily between gases, aerosols and cloud droplets, represent a highly non-linear set of processes that significantly impact the processing and lifetimes of many important tropospheric species. Of increasing interest are chemical transformations involving inorganic, halogenated (Cl and Br) compounds and associated influences on the cycling of NO_x, HO_x, S, O_3, CH_4 and non-methane hydrocarbons (NMHC's), Hg, and other species of both natural and anthropogenic origin.

Accurately resolving interactions that control multiphase processes requires they be evaluated explicitly. The computationally difficult solution of the stiff system of ordinary differential equations (ODEs) derives from multiphase processes (e.g. mass transfer). Computational speed must be optimized in order to execute simulations of sufficient duration to provide time for model equilibration (spin-up) and generation of a sufficient sample size for analysis.

This manuscript describes a coupled atmospheric chemistry and climate modeling system that leverages an efficient multiphase atmospheric chemistry mechanism, MECCA (Module Efficiently Calculating the Chemistry of the Atmosphere; version 2.5; Sander et al., 2005, 2011) within a 3-mode size-resolving aerosol module (Modal Aerosol Module) version of the National Center for Atmospheric Research's (NCAR) Community Atmosphere Model (version 3.6.33; Gent et al., 2009; Liu et al., 2011; hereafter referred to as modal-CAM). The modal aerosol module in CAM was developed to provide a size-resolving aerosol microphysics capability capable of more accurately resolving the direct and indirect impacts of aerosols on climate.

78 Modal-CAM is embedded as the atmosphere component of the NCAR Community Climate

79 System Model (CCSM3.0; Collins et al, 2006). (Note: Since completion of the work presented

80 here, CCSM has been renamed the Community Earth System Model, CESM).

81   The coupled modeling system used in this study was designed to investigate the role of

82 aqueous processes and inorganic halogen cycling through use of their explicit representation in

83 MECCA combined with the size-resolving modal aerosol physics and atmospheric coupling of

84 modal-CAM. Results will be validated and interpreted in detail in a forthcoming manuscript

85 (*Long, M. S., Keene, W.C., Easter, R., Sander, R., Kerkweg, A., Lui, X, Erickson, D.J, Ghan, S.,*

86 *Sensitivity of tropospheric chemical composition to halogen-radical chemistry using a fully*

87 *coupled GCM/size-resolved multiphase chemical system I: Halogen distributions, aerosol*

88 *composition, and sensitivity of climate-relevant gases*).

89

90 2. MECCA Model Description

91   MECCA version 2.5 is a FORTRAN90 compliant atmospheric chemistry module developed to

92 deploy easily as a submodel within base models using the MESSy interface (Modular Earth

93 Submodel System; see http://www.messy-interface.org). Since CAM is not designed as a MESSy

94 compliant base-model, the interface used for this study was designed from scratch to

95 accommodate the complexities of the non-compliant GCM and the needs of the modal aerosol

96 module. MECCA is available at no cost, under the terms of the GNU General Public License

97 (GPL), included within – and not to be confused with – the stand-alone box-model CAABA

98 (Chemistry As A Box-model Application).

99   MECCA contains a comprehensive atmospheric reaction mechanism that includes

100 transformations involving O_3, CH_4, HO_x, and NO_x, NMHCs, halogens (Cl, Br, I), and sulfur. In

101 addition to gas-phase reactions, the scheme includes fully integrated multiphase transformations

102 (both aqueous-phase and heterogeneous pathways) involving aerosols and cloud droplets. Mass

103 transfer is calculated dynamically per Schwartz (1986). Photochemical reaction rates vary as a

104 function of solar zenith angle under clear-sky and cloudy conditions based on Landgraf and

105 Crutzen (1998). MECCA is a MESSy-compliant sub-model within the ECHAM5/MESSy for

106 Atmospheric Chemistry (EMAC) chemistry climate GCM (CCM). Numerous investigations

107 have been performed using this system: These include evaluation of gas-phase chemistry from

108 the surface to the mesosphere (Jöckel et al. 2006), multiphase cycling of marine-derived

109   halogens (Kerkweg et al. 2008a,b), isotopic composition of the atmosphere (Gromov et al.,

110   2010), and influences of chemical processes on polar stratospheric clouds (Kirner et al., 2011).

111   A full list of EMAC applications can be found on http://messy-interface.org. See supplemental

112   Table S1 and Sander et al. (2011) for a complete description of the chemical scheme.

113   MECCA uses the Kinetics PreProcessor (KPP, Sandu and Sander, 2006) to build a solution

114   based on a choice of several predefined numerical methods. KPP was designed to facilitate

115   programming fast and accurate solutions to chemical reaction mechanisms based on user-defined

116   implicit solvers and solver configurations. It relies on sparse linear algebra routines to optimize

117   serial computational performance, and is therefore well suited for atmospheric chemistry

118   problems over a wide range of complexities.

119   The tropospheric chemical mechanism used in the coupled model was based on a subset of the

120   full MECCA mechanism. Other than the addition of gas-phase reactions for non-methane

121   hydrocarbons (NMHCs; based on von Kuhlmann et al. (2003)), the mechanism was identical to

122   that used in Keene et al. (2009) although configured for three rather than eight aerosol size bins.

123   Photochemical rates were calculated using MECCA's JVAL submodel.

124

125   3. Modal-CAM Atmosphere Model

126   Atmospheric processes were simulated in three dimensions (3-D) using CAM at 1.9° x 2.5° lat-

127   long resolution with 26 vertical levels (Gent et al., 2009). CAM is a FORTRAN90 compliant

128   general circulation system built upon an extensive set of high-performance computational

129   routines to preserve scalability and performance of the model across changes in resolution and

130   model physics. The high-performance structure relies upon a message passing interface (MPI),

131   or, at the user's discretion, a combination of MPI and shared-memory process routines.

132   The dynamical core (approximation of the equations of motion on a discrete, spherical grid) is

133   based on a flux-form semi-Lagrangian method (see Lin and Rood, 1996) that is better suited for

134   tracer transport. This approach permits grid-wide stability of the chemistry solution, in contrast

135   to discrete methods that introduce large dispersion and diffusion errors in their approximation of

136   the equations of motion which propagate into and destabilize the chemistry solver.

137   Modal-CAM incorporates a comprehensive set of processes that control the evolution and

138   coupling of three fixed-width log-normally distributed aerosol modes (Aitken, accumulation and

139   coarse). The modal aerosol treatment is described in detail in Liu et al. (2011). Each mode

140   consists of internally mixed populations of non-sea-salt (nss) SO_4^{2-}, organic matter from primary

141   sources (OM), secondary organic aerosol (SOA) from volatile organic precursors, black carbon

142   (BC), inorganic sea salt, and mineral dust. The nss-SO_4^{2-} is assumed to be in the form of

143   NH_4HSO_4. OM and BC are treated only in the accumulation mode. SOA is only in the Aitken

144   and accumulation modes, and mineral dust is only in the accumulation and coarse modes.

145   Aerosol number and aerosol water are also calculated for each mode. Aerosol mass and number

146   associated with stratiform cloud droplets are treated explicitly.

147   The following processes affect aerosols in the model: Grid-resolved transport, sub-grid vertical

148   transport by turbulence and convective clouds, emissions (surface and elevated), sedimentation

149   and dry deposition, cloud droplet activation and subsequent aerosol resuspension, wet removal

150   (in- and below-cloud by stratiform and convective clouds), condensation of H_2SO_4(g) and

151   condensation/evaporation of semi-volatile organics and water, cloud chemistry (oxidation of SO_2

152   to H_2SO_4), transfer (renaming) of particles from Aitken to accumulation mode due to growth via

153   condensation and cloud chemistry, aerosol nucleation, and aerosol coagulation (Aitken and

154   accumulation modes only). Trace gas processes include transport, emission, and dry and wet

155   deposition.

156

157   4. MECCA/Modal-CAM Coupling

158   The coupling involves (1) adding MECCA chemical species to CAM, (2) interfacing MECCA

159   gas, aerosol and cloud chemistry routines within CAM (and disabling the corresponding CAM

160   routines), and (3) as needed, modifying CAM routines for processes that affect MECCA and

161   modal-CAM species (e.g. emission of sea-salt species). This initial implementation is not a

162   complete two-way coupling between MECCA and modal-CAM, as indicated in Fig. 1, since

163   some MECCA aerosol species do not interact directly with the modal-CAM physics. This was

164   done to minimize unnecessary modifications to processes that have little impact from one system

165   to another. The impact of this configuration on memory use and model performance was not

166   evaluated.

167   The MECCA gas and aqueous aerosol species were added to the existing fully-transported

168   trace species in CAM: 96 gas species (4 of which were already treated in modal-CAM), and 31

169   aqueous aerosol species in each of the 3 size modes. The MECCA aqueous cloud-droplet

170   species (31 species for each mode) were also added to the modal-CAM cloud-borne species,

171 which are not fully transported (Liu et al., 2012). This coupling interfaces the bulk inorganic
172 aerosol composition considered by microphysical routines in modal-CAM with chemical
173 speciation evaluated for multiphase processes in MECCA. As such, the system uses redundant
174 chemical species to account for nss-SO_4^{2-} and seasalt between two tracer arrays. Gas-phase
175 species are shared between the MECCA and modal-CAM tracer arrays. Since it was necessary to
176 ensure that the impact of model routines on both bulk species in modal-CAM (e.g. NaCl), and
177 corresponding speciation in MECCA (e.g. Na^+ and Cl^-) are proportional, several model routines
178 operate on both tracer arrays simultaneously (see Fig. 1). Modal-CAM stores information about
179 both sets of species throughout a time-step, and changes are updated accordingly – either from
180 MECCA to CAM (Fig. 1, step 6) or CAM to MECCA (Fig. 1, step 8). The iteration of one model
181 time-step as outlined in Fig. 1 involved 10 discrete steps:

182 Step 1: This step calculates the advective transport for all chemical species.

183 Step 2: Vertical transport of gases and interstitial aerosols in both tracer arrays by shallow
184   convective clouds is calculated. Aerosol activation/resuspension in stratiform clouds is then
185   calculated in conjunction with turbulent vertical mixing, acting on both tracer arrays. The
186   aerosol activation utilizes the modal-CAM aerosol composition (e.g. hygroscopicity
187   calculation neglects MECCA chemical species); but tendencies are applied to all aerosol
188   species.

189 Step 3: Aerosol water uptake is calculated based on modal-CAM's aerosol composition.
190   Resulting aerosol water content is applied to both tracer arrays. Wet deposition of all aerosol
191   species (interstitial and cloud-borne in both arrays) through in-cloud and below-cloud
192   scavenging is then calculated. Next, vertical transport of gases and interstitial aerosols by
193   deep convective clouds is calculated.

194 Step 4: Below-cloud scavenging by rainwater of all soluble gases occurs here.

195 Step 5: Gas, aerosol, and photo chemistry act only on the MECCA tracer array (see Section 2).
196   Total overhead stratospheric O_3 necessary for photochemical rate calculations in MECCA's
197   *JVAL* routine was prescribed. Ion balance is maintained in MECCA by adjusting an inert
198   dummy cation tracer representing the combined charges of Na^+, Ca^+, and Mg^+, which was
199   not coupled to modal-CAM NaCl mass. With the exception of that involving SOA, all gas-
200   aerosol exchange was calculated by MECCA.

201   Step 6: Cloud chemistry includes MECCA-only gas/cloudwater exchange of soluble gas species,

202   equilibrium, and aqueous chemistry in cloud droplets. Cloud chemistry was only activated

203   above a grid-box cloud-fraction threshold of 1×10^{-5}.

204   Step 7: Nss-SO_4^{2-} is passed to modal-CAM after completion of MECCA chemistry. To

205   differentiate total SO_4^{2-} in MECCA, which includes sea-salt SO_4^{2-} from nss-SO_4^{2-} in modal

206   CAM, only the net change in nss-SO_4^{2-} due to MECCA aerosol chemistry ($\Delta SO_{4,Chemistry}$ from

207   aqueous reaction and H_2SO_4 vapor uptake) was considered where

208   nss-$SO_4^{2-}(t+\Delta t)$ = nss-$SO_4^{2-}(t) + \Delta SO_4^{2-}{}_{,Chemistry}$ (1)

209   Nss-SO_4^{2-}, as passed to modal-CAM, is the sum of MECCA's $H_2SO_4(aq)$, HSO_4^-, and SO_4^{2-}

210   species calculated from eq. (1). Nss-SO_4^{2-} for each mode, H_2SO_4 vapor, and corresponding

211   net changes per time-step were calculated here for use by the modal-CAM microphysical

212   routines (step 8).

213   Step 8: The aerosol microphysical processes of condensation (SOA only), intermodal transfer

214   (renaming) after particle growth, nucleation, and coagulation are calculated in modal-CAM

215   routines. Intermodal transfer and coagulation are now applied to both modal-CAM and

216   MECCA aerosol species. Since mass-transfer from the gas to aqueous phase is included in

217   the MECCA chemical ODE, modal-CAM gas-aerosol exchange and condensation routines

218   are switched off for all species except for SOA.

219   Step 9: The only net source of nss-SO_4^{2-} in step 8 was through nucleation of $H_2SO_4(g)$. This

220   increase in nss-SO_4^{2-} due to modal aerosol processing was passed to MECCA as addition of

221        $H_2SO_4(aq)$ to the Aitken mode. In this configuration, both total nss-SO_4^{2-} and H^+ are

222   conserved.

223   Step 10: Emissions of gases, and black carbon, primary organic matter, and NH_4HSO_4 aerosol

224   are driven by offline datasets, while sea salt (and dust?) emissions are calculated online.

225   NH_4SO_4 aerosol are emitted directly as NH_4^+ and HSO_4^{2-} into the MECCA tracer array. The

226   transfer of nss-SO_4^{2-} into the modal-CAM array occurs later (step 6). Sea salt aerosol is as

227   both NaCl in the modal-CAM array and speciated in MECCA as Na^+, Cl^-, SO_4^{2-}, CO_3^{2-}, and

228   Br^-. Sea-salt derived SO_4^{2-} is excluded from modal-CAM (see step 6). Vertical turbulent

229   mixing is applied to all gases. (This is done in step 3 for aerosols.) Dry deposition is

230   includes all aerosol and gas-phase species in both tracer arrays.

231

232   Since impacts on aerosol physical properties due to small changes in abundance of inorganic

233   aerosol species other than Na^+, NO_3^-, NH_4^+ and SO_4^{2-} are limited, and to simplify the modal-

234   CAM aerosol size and inter-modal exchange routines, mass and density of any species specific to

235   MECCA *only* were not considered in calculations of particle mass and size (i.e. density of aged

236   and fresh sea salt are the same). As a result, they only interacted with particle dry diameter

237   through changes in nss-SO_4^{2-}, NH_4^+, and NO_3^-. As well, the volume-weighted hygroscopicities

238   and refractive indices of aerosol modes were calculated using modal-CAM species: bulk NaCl,

239   nss-SO_4^{2-}, dust, BC, POM, and SOA in the 3-mode version, plus NH_4^+ and NO_3^- in the 7-mode

240   version

241

242   5. Computational Configuration and Performance

243   In a global simulation grid that includes the breadth of atmospheric chemical scenarios at any

244   one time-point in the simulation, the use of implicit methods for the multiphase chemistry

245   solution disrupts the scalability of the MPI-based parallel system. In particular, the stiffness of

246   the chemical mechanism, and thus the time and resources needed to reach a solution for a given

247   grid-box, varies geographically in the 3-D domain (e.g., see of Kerkweg et al., 2007). Proximity

248   to large sources and sinks of highly-reactive species or large gradients in physical or chemical

249   conditions complicate the implicit solution. In CAM, systematic, non-random decomposition and

250   allocation of column-subsets of the 3-D grid to the available computational processes segregates

251   a disproportionately large chemical-solution burden into a small subset of processes. Since

252   CAM's time-stepping routines rely on an MPI AllGather routine, model performance is limited

253   by the speed of the slowest column-subset. Model load-balancing optimizations (available since

254   CAM version 3.6) permit the building of MPI column-subsets and allocating them to processes

255   in ways which enhances the distribution of 'difficult' columns across available computational

256   process units (see Mirin and Worley, 2011). The option used for this study (phys_loadbalance =

257   2) builds column-subsets from north/day-south/night grid-point pairs. For example, a grid-point

258   at 45deg N, 0 deg E is paired with the point at 45deg S and 180 deg E. Consequently, since most

259   land area is in the northern hemisphere, this procedure load-balances based across day/night,

260   season, and, to a large extent land/ocean. The set of paired points are then combined into

261   column-subsets and assigned to processes. The maximum number of column-subsets that can be

262   obtained (thus, the number of independent computational processes that can be used

263   simultaneously) is controlled by dynamic limitations and the horizontal grid size. CAM has been

264   designed to permit allocating additional processes to solve model physics separately from the

265   dynamics routines, which allows a much faster computation of the coupled system.

266   To evaluate the computational performance of the coupled system, decomposed as described,

267   three positive-definite, adjustable-timestep Rosenbrock methods were tested for accuracy and

268   performance metrics. Sander et al. (2005) found that, for the MECCA chemical mechanism, 2nd

269   and 3rd order solvers performed best in terms of both stability and computational speed. Other

270   studies have investigated the stability and efficiency of the Rosenbrock solvers in KPP across a

271   range of chemical scenarios (Henze et al., 2007; Verwer et al., 1999; Sandu et al., 1997). To our

272   knowledge, this study is the first in which KPP's Rosenbrock solvers were tested against such a

273   complex chemical mechanism including gas, multiphase, and photochemistry through the entire

274   atmosphere.

275   For stability reasons, the Ros-3 (3-stage, order 3(2), L-stable) solver was employed

276   preferentially in past MECCA simulations (e.g. Keene et al., 2009). Consequently, for these

277   tests, coupled simulation results using Ros-3 are considered the benchmark against which results

278   using Ros-2 (2-stage, order 2(1), L-stable) and RODAS-3 (4-stage, order 3(2), stiffly accurate)

279   solvers are compared (see Hairer and Wanner, 1991). The coupled system was run for 5 years

280   with the Ros-3 solver to stabilize chemistry in the troposphere – defined as a net change in year-

281   to-year total global O_3 mass of less than 1% (actual net O_3 change between years 4 and 5 was

282   0.16% versus 4.7% between years 3 and 4 of the equilibration period). One-month (January)

283   simulations were then executed using the three solvers. Ros-2 and RODAS-3 were compared to

284   Ros-3 for computational speed and reproducibility of several species. Absolute and relative

285   tolerances were set to 10 cm^{-3} and 0.01, respectively.

286   In the implicit solution to the multiphase mechanism, the main sources of instability and

287   stiffness involved complex, fast, multiphase chemistry in the near-surface layers. In addition to

288   high liquid water contents in these layers relative to others, there were large, wind and geography

289   driven 3-D gradients in reactive species and trace intermediates due to reactions in neighboring

290   grid regions, emissions, deposition, microphysical processing, and scavenging. Thus, it is in

291   close proximity to the surface that the limitations of each numerical method – whether in

292   computational stability or accuracy of the solution – was best evaluated.

293   Figure 2 compares mass mixing ratios of the one-month benchmark for O_3, OH, Br_2, and

294   coarse-mode aqueous H^+ for all model layers between the surface and 900mb. These species

295   were selected to reflect climate relevance, source of stiffness, halogen cycle reproducibility, and

296   relevant aqueous processes. Regression statistics are given in Table 1. Ros-2 is able to reproduce

297   O_3 and OH with reasonable confidence, whereas Br_2 and to a much greater extent, H^+ were less

298   precisely reproduced. The reason for the systematic over-prediction of H^+ by Ros-2 is not clear,

299   but may reflect stiffness associated with the aqueous (acid-base) reactions and mass transfer.

300   Conversely, results based on RODAS-3 were more similar to those based on Ros-3 in terms of

301   both absolute (regression slope near 1) and relative differences (higher correlation coefficient;

302   Table 1). The H^+ root mean square error (RMSE; normalized against mean Ros-3 mixing ratios)

303   was still high for the RODAS-3 results. The scatter at higher H^+ mixing ratios generally

304   corresponded to continental regions where sources of atmospheric acids are relatively greater and

305   sea-salt Cl^- and associated regulation of aerosol acidity via HCl phase partitioning is relatively

306   less important. H^+ is highly sensitive to changes in chemistry and circulation in these regions.

307   Circulation changes may also be reflected in the other species due to radiative forcing by O_3 over

308   the benchmark time period. The comparisons demonstrate that RODAS-3 performs markedly

309   better than Ros-2 for all four species.

310   Relative to Ros-3, completion of the one-month benchmark simulation with RODAS-3 was 9%

311   faster and Ros-2 was 18% slower. This is in agreement with a study of KPP solvers in the

312   GEOS-Chem chemistry transport model (Henze, 2007; Eller et al., 2008), although GEOS-Chem

313   uses KPP only for gas-phase calculations and is driven by offline circulation. The frequency

314   distributions of average integration times (or waiting-time for completion of one chemistry

315   timestep) for all grid cells varied among the solvers tested (Fig. 3). Relative to RODAS-3, Ros-2

316   and, to a lesser extent, Ros-3 were skewed towards relatively longer integration times, though

317   there was no systematic change in the peak integration time frequency. These results indicate

318   that the performance gain is due primarily to reduction in frequency of large waiting times and

319   suggest that chemistry-centric grid decomposition and column subsetting that leverages this

320   frequency distribution may yield better model performance. The distribution of waiting times

321   across the global grid demonstrates a physical dependence. While not shown here, chemistry

322   waiting times are inversely dependent upon altitude – the maxima occur in the model surface

323   layer. Further, data show a weak but positive correlation to a combination of total aerosol liquid

324   water and solar zenith angle (as a measure of photochemistry). Based on the benchmark

325   simulation intercomparison, MECCA chemistry for the fully-coupled simulations was solved

326   using the RODAS-3 solver.

327   MECCA, as the chemical operator in CAM, had a substantial impact on model runtime

328   prohibiting the use of this configuration for long-term (century-scale) simulations without a large

329   cost in computational resources. Incorporation of the MECCA species and chemistry routines

330   increased CAM's runtime by a factor of 15 relative to modal-CAM configured with the standard

331   chemical module. Replacing modal-CAM's chemical module with MECCA chemistry slowed

332   overall computational speed by a factor of 8. The transport routines were a factor of 7 slower due

333   to an increase from 25 to 205 active tracers. Further, the data storage needs of a system this

334   extensive were large enough that considerations of Input/Output (I/O) frequency and number of

335   diagnostic quantities was necessary. Monthly-mean output from a 10-year simulation of the

336   coupled system required nearly 850 GB storage, which added an additional computational

337   burden due to the system I/O. I/O is often limiting factor in high-performance system scalability,

338   though it was not a large factor in this system.

339

340   6. Summary

341   A coupled atmospheric chemistry and climate system model was developed to investigate the

342   details of multiphase processes and associated impacts on chemistry and climate. The

343   computational needs of the chemical system required that performance of individual modules be

344   enhanced. Comparison of three implicit Rosenbrock solvers revealed substantial differences in

345   computational performance for coupled simulations that were distinct from similar investigations

346   based on box models alone. This is likely due to the effect of fixed versus variable physical

347   conditions in 0-D versus 3-D global models, combined with the impact of load balancing

348   methods on the net system runtime (solver performance in individual gridboxes was not

349   evaluated). Overall the RODAS-3 solver provided the best performance for the current

350   computational configuration.

351   In addition to optimizations discussed above, such as chemistry-centric load-balancing, several

352   strategies can be pursued to further increase the coupled system's performance. First, chemical

353   species with atmospheric lifetimes shorter than residence-times in a given grid box (so called

354   short-lived species such as $O(_1D)$) can be ignored by the dynamics routines. Prior to including

355 MECCA into CAM for this study, the cost of including additional tracers was the largest factor

356 impacting the system's computational burden. Second, reduction of the size of the chemical

357 mechanism in combination with load-balancing will likely have the greatest impact on runtime.

358 A systematic approach to determining the smallest mechanism necessary to constrain the

359 behavior of a specific subset of chemical species (e.g. O_3 and sulfur) is currently being

360 developed using this system. Lastly, the adoption of optimized or parallel-capable linear algebra

361 routines has the potential to significantly speed up the implicit chemistry, but we are not aware

362 of any successful studies showing this. Doing so would require substantial changes to the

363 existing parallelization strategy in CAM. The development of hybrid systems using stream and

364 conventional processors provides a good opportunity to examine this approach.

365   MECCA, CAM, and the CESM are available for download. The code used here can be made

366 available to users upon request.

367

368 7. References

369

370 Collins, W. D., Bitz, C. M., Blackmon, M. L., Bonan, G. B ., Bretherton, C. S., Carton, J. A.,

371   Chang, P., Doney, S. C., Hack, J. J., Henderson, T. B., Kiehl, J. T., Large, W. G., McKenna,

372   D. S., Santer, B. D., and Smith, R. D.: The Community Climate System Model Version 3

373   (CCSM3). J. Climate, 19, 2122–2143. doi: http://dx.doi.org/10.1175/JCLI3761.1, 2006.

374 Eller, P., Singh, K., Sandu, A., Bowman, K., Henze, D. K., and Lee, M.: Implementation and

375   evaluation of an array of chemical solvers in a global chemical transport model, Geosci.

376   Model Dev. Discuss., 2, 185-207, doi:10.5194/gmdd-2-185-2009, 2009.

377 Gent, P. R., Yeager, S. G., Neale, R. B., Levis, S., and Bailey, D. A.: Improvements in a half

378   degree atmosphere/land version of the CCSM, Clim. Dynam., 34, 6, 819-833,

379   doi:10.1007/s00382-009-0614-8, 2010.

380 Gromov, S., Jöckel, P., Sander, R., & Brenninkmeijer, C. A. M.: A kinetic chemistry tagging

381   technique and its application to modelling the stable isotopic composition of atmospheric

382   trace gases, Geoscientific Model Development, 3, 337–364, doi: 10.5194/gmd-3-337-2010,

383   URL (2010)

384 Hairer, E. and Wanner, G.: Solving Ordinary Differential Equations II. Stiff and Differential-

385   Algebraic Problems, Springer-Verlag, Berlin, 1991.

386 Henze, D.K., Hakami, A., and Seinfeld, J.H.: Development of the adjoint of GEOS-Chem,
387   Atmos. Chem. Phys., 7, 2413-2433, 2007.

388 Jöckel, P., Tost, H., Pozzer, A., Brühl, C., Buchholz, J., Ganzeveld, L., Hoor, P., Kerkweg, A.,
389   Lawrence, M. G., Sander, R., Steil, B., Stiller, G., Tanarhte, M., Taraborrelli, D., van
390   Aardenne, J., & Lelieveld, J.: The atmospheric chemistry general circulation model
391   ECHAM5/MESSy1: consistent simulation of ozone from the surface to the mesosphere,
392   Atmos. Chem. Phys., 6, 5067–5104, doi: 10.5194/acp-6-5067-2006, 2006.

393 Keene, W. C., Long, M. S., Pszenny, A. A. P., Sander, R., Maben, J. R., Wall, A. J., O'Halloran,
394   T. L., Kerkweg, A., Fischer, E. V., and Schrems, O.: Latitudinal variation in the multiphase
395   chemical processing of inorganic halogens and related species over the eastern North and
396   South Atlantic Oceans, Atmos. Chem. Phys., 9, 7361-7385, doi:10.5194/acp-9-7361-2009,
397   2009.

398 Kerkweg, A., Sander, R., Tost, H., Jöckel, P., and Lelieveld, J.: Technical note: Simulation of
399   detailed aerosol chemistry on the global scale using mecca-aero, Atmos. Chem. Phys., 7,
400   2973-2985, 2007.

401 Kerkweg, A., Jöckel, P., Pozzer, A., Tost, H., Sander, R., Schulz, M., Stier, P., Vignati, E.,
402   Wilson, J., & Lelieveld, J.: Consistent simulation of bromine chemistry from the marine
403   boundary layer to the stratosphere Part 1: Model description, sea salt aerosols and pH,
404   Atmospheric Chemistry and Physics, 8, 5899–5917, doi: 10.5194/acp-8-5899-2008, 2008a.

405 Kerkweg, A., Jöckel, P., Warwick, N., Gebhardt, S., Brenninkmeijer, C. A. M., and Lelieveld, J.:
406   Consistent simulation of bromine chemistry from the marine boundary layer to the
407   stratosphere Part 2: Bromocarbons, Atmospheric Chemistry and Physics, 8, 5919–5939, doi:
408   10.5194/acp-8-5919-2008b.Kirner, O., Ruhnke, R., Buchholz-Dietsch, J., Jöckel, P., Brühl,
409   C., and Steil, B.: Simulation of polar stratospheric clouds in the chemistry-climate-model
410   EMAC via the submodel PSC, Geoscientific Model Development, 4, 169–182, doi:
411   10.5194/gmd-4-169-2011, URL, 2011.

412 Landgraf, J. and Crutzen, P. J.: An Efficient Method for online calculations of Photolysis and
413   Heating Rates, J. Atmos. Sci., 55, 863–878, 1998.

414 Lin, S.-J., and Rood, R. B.: Multidimensional flux form semi-Lagrangian transport schemes,
415   Mon. Wea. Rev., 124, 2046–2070, 1996.

416   Liu, X., Easter, R. C., Ghan, S. J., Zaveri, R., Rasch, P., Shi, X., Lamarque, J.-F., Gettelman, A.,
417   Morrison, H., Vitt, F., Conley, A., Park, S., Neale, R., Hannay, C., Ekman, A. M. L., Hess,
418   P., Mahowald, N., Collins, W., Iacono, M. J., Bretherton, C. S., Flanner, M. G., and Mitchell,
419   D.: Toward a minimal representation of aerosol direct and indirect effects: model description
420   and evaluation, Geosci. Model Dev., 5, 709-739, doi:10.5194/gmd-5-709-2012, 2011.

421   Mirin A., Worley, P. H.: Improving the performance scalability of the community atmosphere
422   model, International Journal of High Performance Computing Applications 26, 17-30,
423   doi:10.1177/1094342011412630, 2011.

424   Sander R., and Baumgaertner, A., Gromov, S., Harder, H., Jöckel, P., Kerkweg, A., Kubistin, D.,
425   Regelin, E., Riede, H., Sandu, A., Taraborrelli, D., Tost, H. and Xie, Z.-Q.: The atmospheric
426   chemistry box model CAABA/MECCA-3.0, Geosci. Model Dev. 4, 373-380, 2011
427   http://www.geosci-model-dev.net/4/373

428   Sander, R., Kerkweg, A., Jöckel, P., and Lelieveld, J.:, Technical Note: The new comprehensive
429   atmospheric chemistry module MECCA, Atmos. Chem. Phys., 5, 445-450, 2005.

430   Sander, R., Crutzen, P.J.: Model study indicating halogen activation and ozone destruction in
431   polluted air masses transported to the sea, J. Geophys. Res., 101, 9121-9138, 1996.

432   Sandu A., and Sander, R.: Technical note: Simulating chemical systems in Fortran90 and Matlab
433   with the Kinetic PreProcessor KPP-2.1, Atmos. Chem. Phys., 6, 187-195, 2006,
434   http://www.atmos-chem-phys.net/6/187.

435   Sandu, A., Verwer, J.G., Blom, J.G., Spee, E.J., Carmichael, G.R., Potra, F.A.: Benchmarking
436   stiff ode solvers for atmospheric chemistry problems II: Rosenbrock solvers. *Atmos. Env.*, 31,
437   3459-3472, doi:10.1016/S1352- 2310(97)83212-8, 1997.

438   Schwartz, S. E.: Mass-transport considerations pertinent to aqueous phase reactions of gases in
439   liquid-water clouds, in Chemistry of Multiphase Atmospheric Systems, NATO ASI Series,
440   Vol. G6 , edited by W. Jaeschke, pp. 415–471, Springer Verlag, Berlin, 1986.

441   Strahan, S. E., Douglass, A. R., Stolarski, R. S., Akiyoshi, H., Bekki, S., Braesicke, P., Butchart,
442   N., Chipperfield, M. P., Cugnet, D., Dhomse, S., Frith, S. M., Gettelman, A., Hardiman,
443   S. C., Kinnison, D. E., Lamarque, J.-F., Mancini, E., Marchand, M., Michou, M.,
444   Morgenstern, O., Nakamura, T., Olivié, D., Pawson, S., Pitari, G., Plummer, D. A., Pyle,
445   J. A., Scinocca, J. F., Shepherd, T. G., Shibata, K., Smale, D., Teyssèdre, H., Tian, W., &

446 Yamashita, Y.: Using transport diagnostics to understand chemistry climate model ozone
447 simulations, J. Geophys. Res., 116, D17302, doi: 10.1029/2010JD015360, 2011.

448 Verwer, J.G., Spee, E.J., Blom, J.G., Hundsdorfer, W.: A Second-Order Rosenbrock Method
449 Applied to Photochemical Dispersion Problems. *SIAM J. Sci. Comp.*, 20:1456-1480,
450 doi:10.1137/S1064827597326651, 1999.

451 von Kuhlmann, R., Lawrence, M. G., Crutzen, P., and Rasch, P.: A model for studies of
452 tropospheric ozone and nonmethane hydrocarbons: Model description and ozone results, J.
453 Geophys. Res., 108, 4294, doi:10.1029/2002JD002893, 2003.

454   Figure 1. Schematic showing the order of relevant chemistry, dynamics and physics routines (light gray boxes) over a single model

455   time iteration (Δt) relative to the MECCA (white horizontal bar) and the modal-CAM (gray dark-gray horizontal bar) tracer arrays.

456   Boxes indicating model operations are oriented vertically across the tracer array bars to indicate whether they interact with one or both

457   tracer arrays. Step indices correspond to those described in the text (see Section 4).
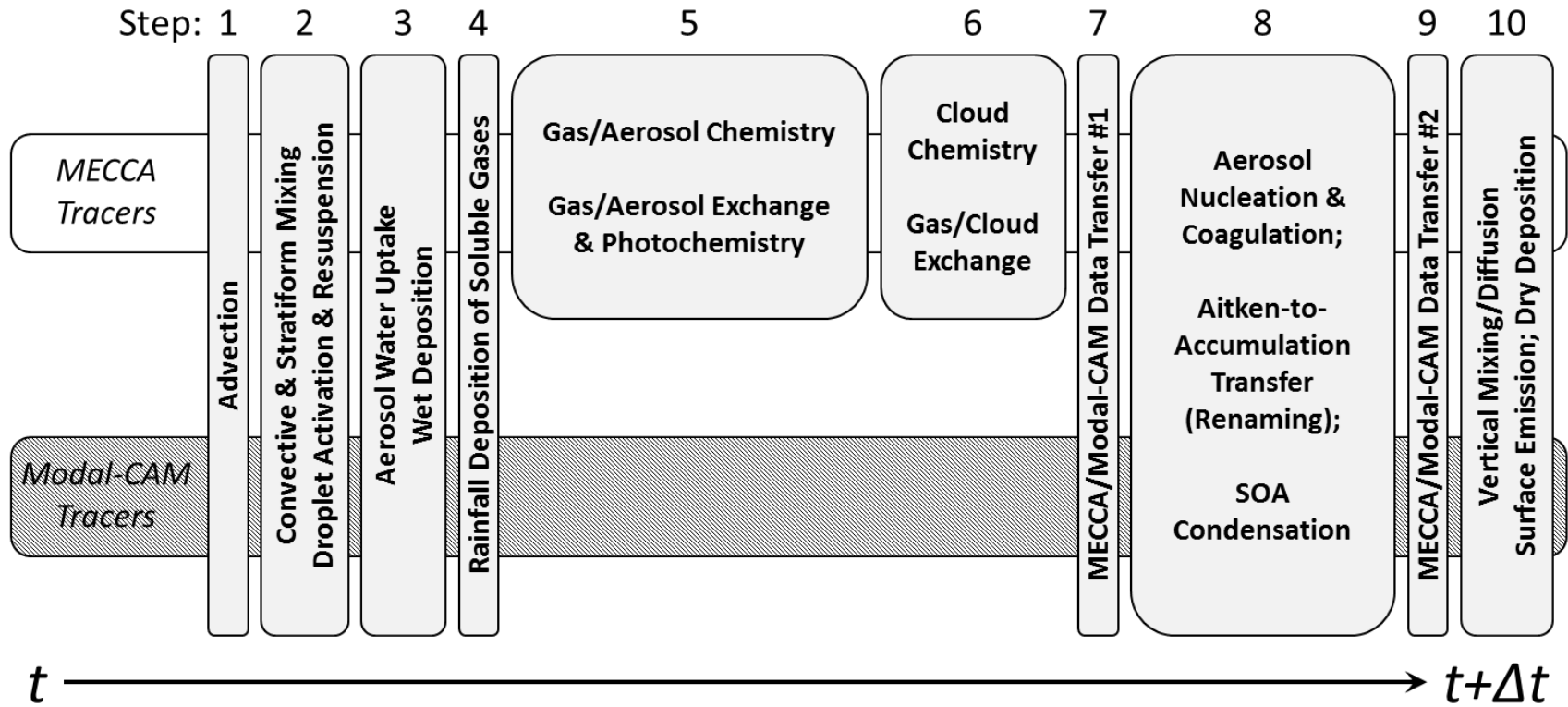

458

459   Figure 2. Comparison of O_3 (a and b), OH (c and d), Br_2 (e and f), and coarse mode H^+ (g and h)

460   at grid boxes between the surface and 900 mb from one-month benchmark simulations using

461   RODAS-3 (left column X axis) and Ros-2 (right column X axis) solvers versus Ros-3 (Y axis)

462   over the same time period. Black lines depict least-squares standard linear regressions (see Table
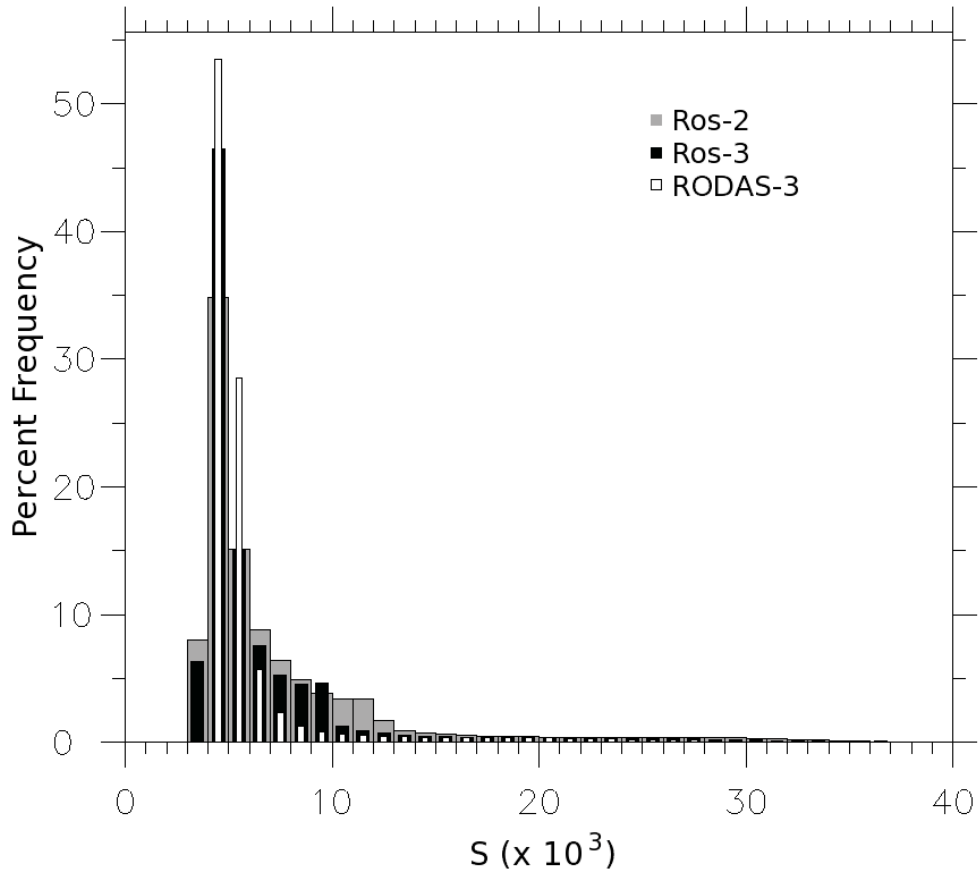
463   1).

464

465
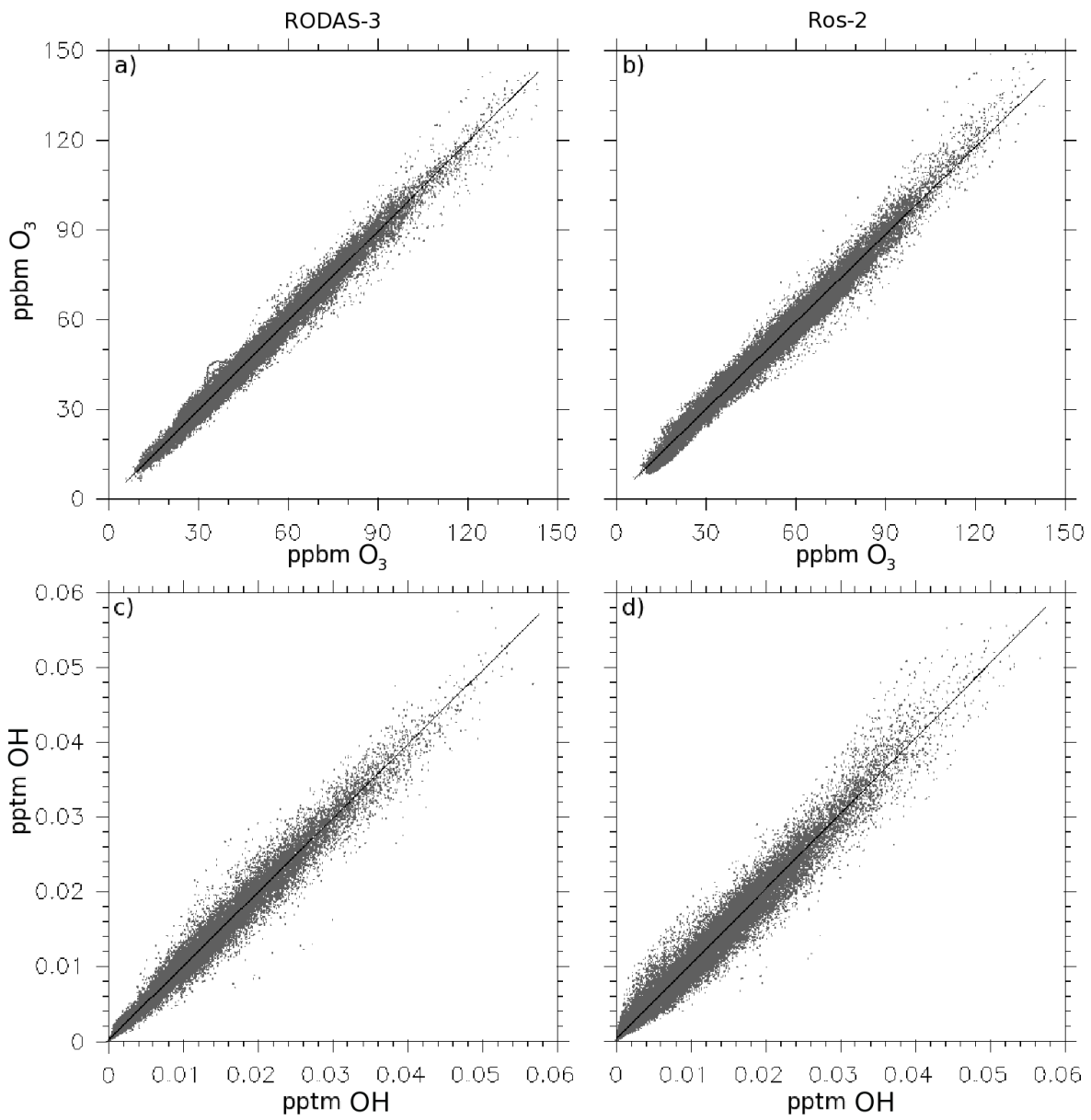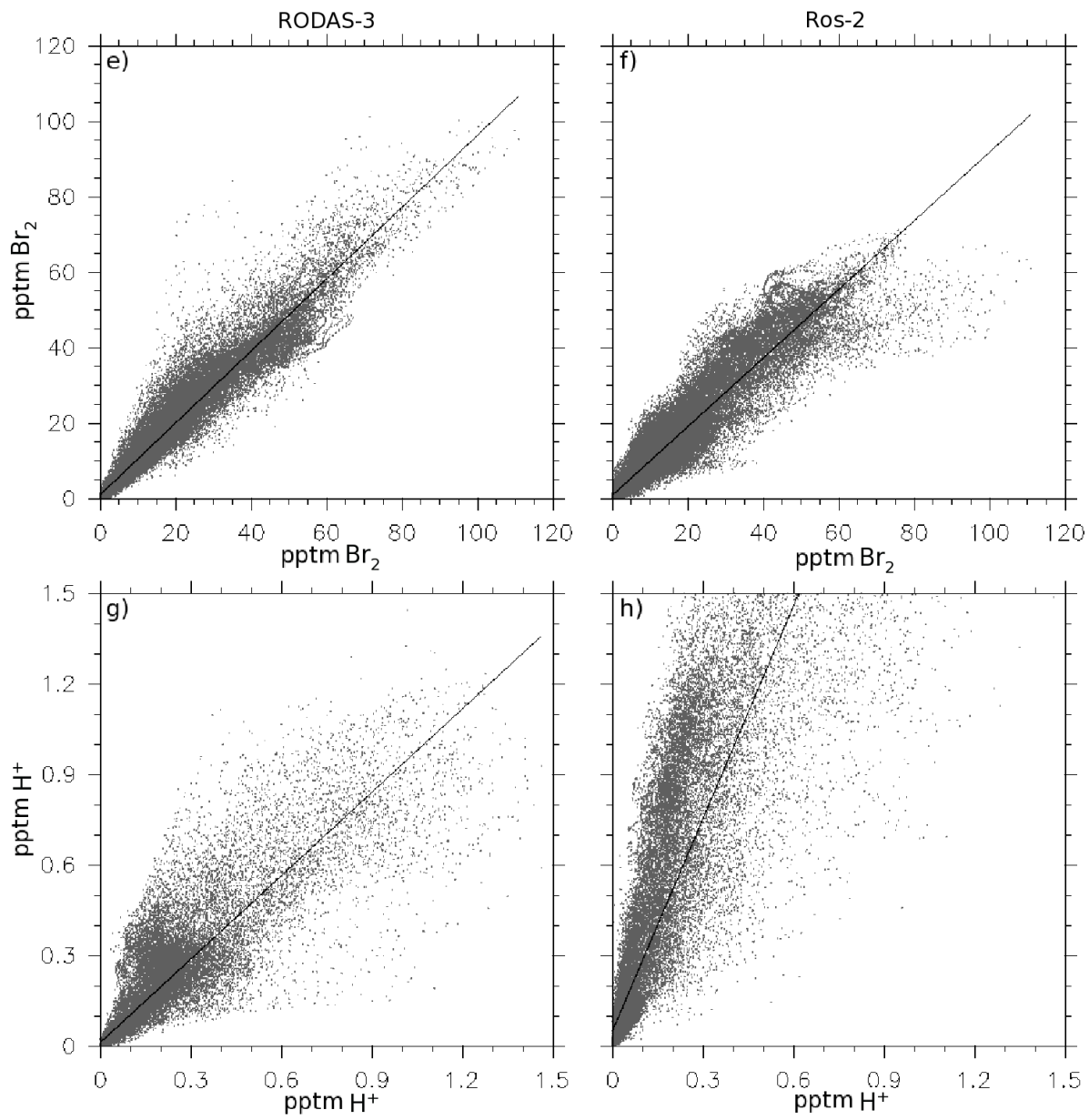
467   Figure 3. Histogram of the percent frequency distribution of per grid-box chemistry integration

468   times (in milliseconds) using MECCA in the modal-CAM global atmosphere for the one-month

469   benchmarks using three different Rosenbrock solvers.

470

471   Table 1. Comparison of one-month benchmark simulations of the coupled modal-CAM/MECCA

472   system for Ros-2 and RODAS-3 solvers versus Ros-3.

	Species	Regression Line	R^2	RMSE (%)
Ros-2	O_3	0.98x + 0.56	0.99	6.5%
	OH	1.0x + 1.5x10^{-4}	0.98	17%
	Br_2	0.91x + 0.87	0.94	42%
	H^+ (Coarse Mode)	2.35x + 0.048	0.93	410%
RODAS-3	O_3	0.98x − 0.36	0.99	5.1%
	OH	0.99 + 7.3x10^{-5}	0.99	11%
	Br_2	0.95x + 0.98	0.97	29%
	H^+ (Coarse Mode)	0.92 + 0.011	0.97	120%

473

Part II: Sensitivity of tropospheric chemical composition to halogen-radical chemistry using a fully coupled GCM/size-resolved multiphase chemical system I: Halogen distributions, aerosol composition, and sensitivity of climate-relevant gases.

M.S. Long (mlong@seas.harvard.edu)

    School of Engineering and Applied Sciences, Harvard University, Cambridge, MA, USA

W.C. Keene (wck@virginia.edu)

    Department of Environmental Sciences, University of Virginia, Charlottesville, VA 22904, USA

R. C. Easter (Richard.Easter@pnnl.gov)

    Atmospheric Sciences and Global Change Division, Pacific Northwest National Laboratory

R. Sander (rolf.sander@mpic.de)

    Air Chemistry Department, Max-Planck Institute of Chemistry, 55020 Mainz, Germany

X. Liu (xiaohong.liu@pnnl.gov)

    Atmospheric Science and Global Change Division, Pacific Northwest National Laboratory, Richland, Washington, USA

A. Kerkweg (kerkweg@uni-mainz.de)

    Institute for Atmospheric Physics, University of Mainz, 55099 Mainz, Germany

D. Erickson (ericksondj@ornl.gov)

    Computer Science and Mathematics Division, Oak Ridge National Laboratory, Oak Ridge, TN USA

498   Abstract

499   Observations and model studies suggest a significant but highly non-linear role for

500   halogens, primarily Cl and Br, in multiphase atmospheric processes relevant to tropospheric

501   chemistry and composition, aerosol evolution, radiative transfer, weather, and climate. The

502   sensitivity of global atmospheric chemistry to the production of marine aerosol and the

503   associated activation and cycling of inorganic Cl and Br was tested using a size-resolved

504   multiphase coupled chemistry/Global Climate model (National Center for Atmospheric

505   Research's Community Atmosphere Model (CAM); v3.6.33). Simulation results showed

506   strong meridional and vertical gradients in Cl and Br species. The simulation reproduced

507   most available observations with reasonable confidence permitting the formulation of

508   potential mechanisms for several previously unexplained halogen phenomena including the

509   enrichment of Br^- in submicron aerosol, and the presence of a BrO maximum in the polar free

510   troposphere. However, simulated total volatile Br mixing ratios were generally high in the

511   troposphere. Br in the stratosphere was lower than observed due to the lack of long-lived

512   organobromine species in the simulation. Comparing simulations using chemical mechanisms

513   with and without reactive Cl and Br species demonstrated a significant temporal and spatial

514   sensitivity of primary atmospheric oxidants (O_3, HO_x, NO_x), CH_4, and non-methane

515   hydrocarbons (NMHC's) to halogen cycling. Simulated O_3 and NO_x were globally lower

516   (65% and 35%, respectively, less in the planetary boundary layer based on median values) in

517   simulations that included halogens. Globally, little impact was seen in SO_2 and non-sea-salt

518   SO_4^{2-} processing due to halogens. Significant regional differences were evident: The lifetime

519   of nss-SO_4^{2-} was extended downwind of large sources of SO_2. The burden and lifetime of

520   DMS (and its oxidation products) were lower by a factor of 5 in simulations that included

521   halogens, versus those without, leading to a 20% reduction in nss-SO_4^{2-} in the southern

522   hemisphere planetary boundary layer based on median values.

25

523

524

525   1. Introduction

526   The development of comprehensive global Earth system models that are able to accurately

527   simulate the climate system requires detailed understanding and treatment of multiphase

528   atmospheric processes relevant to aerosol evolution and radiative transfer. However, due in

529   part to limitations in computational power relative to numerical needs, most current Earth

530   system models treat the physicochemical processing of size-resolved aerosols using

531   parameterizations that are computationally conservative but, in many respects, inadequate to

532   reliably characterize aerosol-climate interactions. These limitations contribute to the large

533   uncertainties in the radiative effects of atmospheric aerosols, which are among the major

534   factors that constrain our current understanding of and ability to predict global climate

535   change.

536   Reliable simulation of the physical and chemical evolution of aerosols in the Community

537   Climate System Model (CCSM) and other Earth systems models requires explicit evaluation

538   of processes as a function of size. Because of direct physical feedbacks, representative

539   simulation of climatic influences also requires an interactive online scheme for aerosol

540   microphysics and multiphase chemistry. A number of major issues must be considered to

541   implement such a scheme. Direct interactions between relatively long-lived and fast-reacting

542   species coupled with large concentration and size gradients of both aerosols and important

543   related atmospheric constituents such as water vapor (e.g., Kerkweg et al., 2007), introduces

544   a high degree of numerical stiffness that is unevenly distributed across the gridded model

545   domain.

546   The size- and composition-dependent properties of aerosols significantly influence

547   radiative fluxes through the atmosphere via two sets of interrelated processes. First, aerosols

548   scatter and absorb incident and outgoing radiation and thereby directly influence net radiative

549   transfer through the atmosphere and the associated distribution and partitioning of heat (and

550   related kinetic and thermodynamic properties). Second, aerosols act as cloud condensation

551   nuclei (CCN) and thereby influence the microphysical properties of clouds including droplet

552   number, size distribution, and lifetime. Through this latter set of processes, aerosols

553   indirectly regulate radiative transfer via the associated modulation of physicochemical

554   evolution and albedo of clouds. These processes also influence precipitation fields and, thus,

555   the hydrologic cycle and related climatic feedbacks.

556   Aerosols also interact directly in the cycling and associated climatic effects of important

557   tropospheric gases, particularly over the ocean. The production from marine-derived

558   precursors and multiphase cycling of halogen radicals represents a significant net sink for

559   ozone in the remote marine boundary layer (MBL) (Dickerson et al., 1999; Galbally et al.,

560   2000; Nagao et al., 2000; Sander et al., 2003; Pszenny et al., 2004; Keene et al., 2009) and a

561   potentially important net source in polluted coastal (Tanaka et al., 2003; Osthoff et al., 2008)

562   and continental air (Thornton et al., 2010). The associated formation and scavenging of

563   halogen nitrates accelerates the conversion of NO_x to HNO_3 and particulate NO_3^- thereby

564   contributing to net O_3 destruction (Sander et al., 1999; Pszenny et al. 2003; Keene et al.,

565   2009). Marine-derived halogen radicals (BrO and atomic Cl) oxidize $(CH3)_2S$ (dimethyl

566   sulfide, DMS) in the gas phase (Toumi, 1994; Keene et al., 1996; Saiz-Lopez et al., 2004)

567   and hypohalous acids oxidize S(IV) in aerosol solutions (Vogt et al., 1996; Keene et al.,

568   1998; von Glasow et al., 2002; von Glasow and Crutzen, 2004). The large surface area of

569   primary marine aerosols also competes efficiently with nuclear clusters (from gas-to-particle

570   reactions) for condensable reaction products from the oxidation of gaseous precursors

571   (including H_2SO_4 from SO_2 oxidation) thereby diminishing the potential for clusters to grow

572   to sustainable size. Consequently, the climatic influences of sulfur cycling may be

573   substantially less than predicted based on models that do not explicitly evaluate interactions

574   involving primary marine aerosols. Chlorine radicals also oxidize methane (an important

575   greenhouse gas) (Platt et al., 2004; Lawler et al., 2009) and non-methane hydrocarbons

576   (Keene et al., 2007; Pszenny et al., 2007), which leads to the production of condensable

577   organic compounds that contribute to aerosol growth and, in the presence of sufficient NO_x,

578   peroxy radicals that enhance oxidation potential. The photochemical processing of marine-

579   derived organic compounds is an important source of OH and other radicals that enhance

580   oxidation potential within aerosol solutions (McDow et al., 1996; Zhou et al., 2006;

581   Anastasio et al., 2007).

582   In terms of mass flux, bursting bubbles produced by breaking waves at the ocean surface

583   are the largest source of aerosols in Earth's atmosphere (Andreae and Rosenfeld, 2008). The

584   nascent droplets dehydrate into equilibrium with ambient water vapor and undergo other

585   rapid (seconds) multiphase transformations involving the scavenging of gases, aqueous and

586   surface reactions, and volatilization of products. (e.g., Chameides and Stelson, 1992;

587 Erickson et al., 1999; Sander et al., 2003). The sub-µm fractions dominate number

588 concentrations and associated direct and indirect influences on radiative transfer and climate

589 (e.g., O'Dowd et al., 1997).

590   In this paper, the sensitivity of global atmospheric chemistry to the production of marine

591 aerosol and the associated activation and cycling of inorganic Cl and Br was tested using a 3-

592 mode size-resolving aerosol module (Modal Aerosol Module) version of the three-

593 dimensional (3-D) National Center for Atmospheric Research's Community Atmosphere

594 Model (CAM version 3.6.33; Gent et al., 2009; Liu et al., 2012; hereafter referred to as

595 modal-CAM) coupled to the multiphase chemical module MECCA (Module Efficiently

596 Calculating the Chemistry of the Atmosphere; Sander et al., 2005). The companion paper by

597 Long et al. (2012) describes the coupled modeling system in detail. A follow-up manuscript

598 will evaluate the sensitivity of climate to halogen cycling and the implications of multiphase

599 processes for aerosol populations and cloud microphysical properties.

600

601   2.   Model Description

602   Atmospheric processes were simulated in 3-D using modal-CAM at 1.9° x 2.5° lat-long

603 resolution with 26 vertical levels (Gent et al., 2009). Modal-CAM is a FORTRAN90

604 compliant general circulation system built upon an extensive set of high-performance

605 computational routines to preserve scalability and performance of the model across changes

606 in resolution and model physics.

607   The dynamical core (approximation of the equations of motion on a discrete, spherical

608 grid) is based on a flux-form semi-Lagrangian method better suited for tracer transport. This

609 approach permits grid-wide stability of the chemistry solution, in contrast to discrete methods

610 that introduce large dispersion and diffusion errors in their approximation of the equations of

611 motion which propagate into and destabilize the chemistry solver.

612   Modal-CAM incorporates a comprehensive set of processes that control the evolution and

613 coupling of three fixed-width log-normally distributed aerosol modes (Aitken, accumulation

614 and coarse). The modal aerosol treatment is described in detail in Liu et al. (2012). Each

615 mode consists of internally mixed populations of non-sea-salt (nss) SO_4^{2-}, organic matter

616 from primary sources (OM), secondary organic aerosol (SOA) from volatile organic

617 precursors, black carbon (BC), inorganic sea salt, and mineral dust. The nss-SO_4^{2-} is assumed

618 to be in the form of NH_4HSO_4. OM and BC are treated only in the accumulation mode. SOA

619 is only in the Aitken and accumulation modes, and mineral dust is only in the accumulation

620   and coarse modes. Aerosol number and aerosol water are also calculated for each mode.

621   Aerosol mass and number associated with stratiform cloud droplets are treated explicitly.

622

623   2.1 Marine Aerosol Source Function

624   Size-resolved emissions of particle number, inorganic sea-salt, and OM mass from the

625   surface ocean were calculated in CAM as functions of wind speed and surface ocean chl a

626   based on Long et al. (2011). Modeled size bins were centered on 0.039, 0.076, 0.15, 0.52,

627   2.4, 4.9, 15.1 and 30-μm diameters at 98% relative humidity (i.e., RH within the laminar sub-

628   layer immediately above the air-sea interface) across bin widths (dD_p) of 0.03, 0.05, 0.1, 0.2,

629   1.0, 3.0, 10.0 and 20.0 μm, respectively. Following dehydration to equilibrium water contents

630   at an average RH of 80% in the mixed layer above the laminar sub-layer, compositions were

631   summed over the three aerosol size modes considered by CAM. Since the 3-mode version of

632   CAM considers OM mass only in the accumulation mode, the OM mass was summed over

633   all particle sizes below 1.0-μm diameter at 80% RH, and emitted directly into the

634   accumulation mode (mode-1).

635

636   2.3 Prescribed Conditions and Initializations

637   CH_4, N_2O, and CO_2 mixing ratios were fixed at 1.77, 0.32, and 378 ppmv, respectively. O_3

638   was calculated online. Direct surface emissions of DMS, SO_2, secondary organic aerosol

639   precursor gases, subgrid-scale NH_4HSO_4 (mode-1 and mode-2), NH_3, and NO_x were based on

640   Dentener et al. (2006). Surface emissions of CO, CH_3OH, C_2H_4, C_3H_6, C_3H_8, and isoprene

641   were based on the Precursors of Ozone and their Effects in the Troposphere (POET) database

642   for 2000 (Granier et al., 2005).

643   The atmosphere model was initialized at January 1, 2000. Due to the heavy computational

644   burden of running the MECCA mechanism, and to reduce model spin-up time, the sea-

645   surface temperature was based on offline data for the 2000 calendar year, and was cycled

646   annually. The sea-ice interface used version 4 of the Community Sea Ice Model (CSIM4;

647   Briegleb et al., 2002). The land interface used version 2 of the Community Land Model

648   (CLM2; Dickenson et al., 2006). Fields of chl a concentrations (in units of mg m^{-3}) in surface

649   seawater were set equal to monthly averages derived from SeaWIFS imagery (1° x 1° ,

650   Gregg, 2008) for the period September 1997 through December 2002, as in Long et al.

651   (2012). The aerosol modes were initialized at zero number with sizes centered log-normally

652   on 0.026, 0.11, and 2.0 μm geometric mean dry diameters for the Aitken, accumulation, and

653   coarse modes, respectively. The corresponding ranges for the log-normal centroids were

654   0.0087 to 0.052, 0.053 to 0.44, and 1.0 to 4.0 μm dry diameter respectively.

655

656   2.4 Global Simulations and Reporting Conventions

657   Results for the coupled MECCA scheme, for which chemical reactions involving halogens

658   were calculated explicitly (denoted *Hal*), were compared with corresponding runs for which

659   halogen chemistry was turned off (denoted *NoHal*). Differences in results were interpreted to

660   evaluate the role of halogens in the physicochemical evolution of the atmosphere.

661   Unless otherwise stated, the following conventions are used. Values are based on grid-box

662   area-weighted spatial fields for the simulated period from January, 1 2005 – December, 31

663   2014. Notation is specified for atmospheric region and time period over which statistics were

664   calculated. Ten-year area-weighted statistics are referred to as ANN for annual, DJF for

665   December/January/February, MAM for March/April/May, and JJA for June/July/August.

666   Spatial statistics for specific atmospheric regions were compiled over the northern and

667   southern hemispheres, (NH and SH, respectively), the entire planetary boundary layer (PBL),

668   the continental-only boundary layer (CBL), marine-only boundary layer (MBL), and the

669   entire free troposphere (FT). Model layers corresponding to these regions are defined below.

670   Analyses based on specific model layers (e.g. the surface layer) are specified as such. Results

671   for a given atmospheric region are based on median and range of 10-year mean climatology

672   for that region and time period (as defined above). For example, the annual O_3 mixing ratio

673   for the planetary boundary layer (ANN-PBL) would be reported as the median and range

674   across the PBL of the 10-year climatological mean.

675   Temporal-only statistics for a given grid box are reported as mean ± standard deviation.

676   The O_3 mixing ratio corresponding to a long-term measurement site would be reported only

677   as a 10-year climatological mean and standard deviation. When necessary to facilitate direct

678   comparison with observations or results from other published simulations, simulated results

679   are reported using the same convention as the reported values.

680   For all discussions here, the tropopause was defined as the minimum pressure level in the

681   model (maximum altitude) above which the temperature lapse rate was positive between

682   levels (70.06 mb or ~18 km), which is consistent with the World Meteorological

683   Organization's tropopause definition. In CAM, the boundary layer is not well resolved, and

684   was therefore defined as the lowest four levels (highest pressure) of the model atmosphere

685   (below 867 mb). The free troposphere was defined as the region between the top of the

686 boundary layer and the tropopause. For comparisons with measurements at surface sites for

687 which altitudes are known, simulated results were interpolated vertically to the corresponding

688 measurement altitudes. Otherwise, the results from the likely nearest model pressure level

689 were used. Unless otherwise noted, comparisons between results for *Hal* relative to *NoHal*

690 simulations are presented as percent deviation defined as (using O_3 as an example),

691
$$\% \, Deviation(O_3) = \frac{[O_3]_{Hal} - [O_3]_{NoHal}}{[O_3]_{NoHal}} \times 100 \qquad (1)$$

692 3. Results

693 3.1 Marine Aerosol Population Characteristics

694 Mean aerosol composition and mixing ratios of gases simulated for each atmospheric

695 region are compiled in supplemental material (Tables S1 and S2). Globally averaged annual

696 marine aerosol production flux, burden, dry and wet deposition for both the *Hal* and *NoHal*

697 (not shown, since these marine aerosol statistics were virtually identical for the simulated

698 time period) simulations fell within the range of published estimates (Table 1). The total Na^+

699 mass flux was 25% less than that reported by Long et al. (2011), which resulted in part from

700 differences in model physics between the different CAM versions used in the two studies

701 (3.5.07 for Long et al., 2011 and 3.6.33 here) and the number of aerosol size bins considered

702 (8 for Long et al., 2011 and 3 here). The corresponding spatial range in mean Na^+ lifetimes

703 against deposition was also within that reported by Pierce and Adams (2006) of 0.46 to 2.72

704 days. Mean dry deposition fluxes are towards the lower end of published estimates whereas

705 wet fluxes fall near the mid-range of published estimates. Available evidence indicates that

706 cloud and precipitation processes are represented reasonably well within CAM3 (e.g. Boville

707 et al., 2006), which implies that simulated deposition fluxes are also reasonable.

708

709 3.2 Model Sensitivity to Inorganic Halogen Cycling

710 For the simulations reported herein, dehalogenation of marine aerosol is the only primary

711 source for volatile inorganic Br and Cl species. Because emissions of halocarbons from

712 marine biogenic sources, biomass- and fossil-fuel combustions, industrial sources, and

713 terrestrial ecosystems, are not considered, the total global emissions of halogens correspond

714 to lower limits. In addition, as discussed in detail by Keene et al. (2009), available evidence

715 suggests that the MECCA scheme as currently configured overestimates rates of Br cycling

716 to some extent and consequently, simulated rates of Br activation and associated impacts are

717   considered upper limits. In the following text and tables, Br_t is defined as the sum of all

718   volatile inorganic Br species and Cl* is defined as all inorganic Cl gases other than HCl,

719   which includes HOCl, 2 x Cl_2, $ClNO_2$, $ClNO_3$, OClO, and BrCl.

720

721   3.2.1 Br Distributions

722   Simulated Br_t averaged over the tropospheric column ranged from 0.038 to 44 pmol mol^{-1}

723   (median 6.1 pmol mol^{-1}). Median Br_t for ANN-FT was 2.5 (0.038 to 32) pmol mol^{-1}. von

724   Glasow et al. (2004) reported Br_t from 1 to 6 pmol mol^{-1} for the FT based on simulations that

725   considered Br sources other than sea-salt aerosol. While these ranges overlap, mixing ratios

726   simulated by von Glasow (2004) are lower limits because the sources do not include marine

727   aerosol production. Simulated zonal median Br_t reveals little Br_t in the upper troposphere and

728   stratosphere, which is inconsistent with observation (e.g. Fitzenberger et al., 2000; see

729   Supplemental Figure S1) and model calculations (von Glasow et al., 2004). Most

730   stratospheric Br is believed to originate from the photolysis of long-lived organic Br species

731   (e.g. CH_3Br) (Montzka et al., 2003), which are not considered in the MECCA chemical

732   mechanism employed for these simulations or the emission fields for Modal-CAM. To

733   achieve observed levels of stratospheric Br_t with the computational resources available for

734   this analysis would have required offline Br sources. The radiative transfer scheme used to

735   calculate photochemical rates was tuned to reproduce stratospheric O_3 climatological means.

736   Consequently, the impact of the upper-atmosphere Br on tropospheric photochemistry is

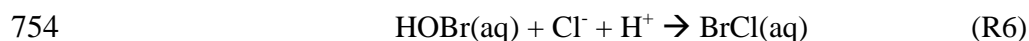737   believed to be negligible.

738   Global median vertical profiles and speciation of Br_t for ANN and JJA (Fig. 1) reveal that,

739   between 700 to 800 mb pressure level (2 to 3 km altitude) and the surface, Br_t is dominated

740   by roughly equal amounts of Br_2 and BrCl on a molecular basis. For DJF , BrCl was higher

741   than Br_2 by a factor of about two. At higher altitudes, HBr (most of which is produced via the

742   reaction of Br + HCHO) increases to become the dominant gas-phase Br species. In the lower

743   troposphere, HBr is efficiently scavenged by liquid aerosol or cloud droplets. In the FT, most

744   Br is recycled in the gas phase via

745                            $Br + O_3 \rightarrow BrO + O_2$ (R1)

746                            $BrO + hv \rightarrow Br + O(_3P)$ (R2)
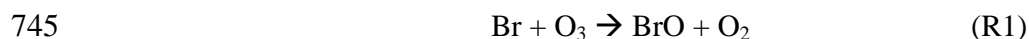
747   with an important secondary pathway (ranging from 5% to 20%) through

748                            $BrO + HO_2 \rightarrow HOBr + O_2$ (R3)

749                            $HOBr + hv \rightarrow Br + OH$ (R4)

750   In the NH-FT, BrO + NO competes with R3 at approximately equal proportions. In the mid

751   and high latitude FT of the NH and SH, 7% to 15% of HOBr is converted to BrCl via the

752   multiphase pathway involving accumulation mode aerosol:

753                             $HOBr(g) \rightarrow HOBr(aq)$ (R5)

754                      $HOBr(aq) + Cl^- + H^+ \rightarrow BrCl(aq)$ (R6)

755                             $BrCl(aq) \rightarrow BrCl(g)$ (R7)

756   In the MBL, 15% to 50% of HOBr reacts via the above pathway.

757   Multiphase recycling is not completely inactive in the FT. For example, a persistent but

758   seasonally variable BrO maximum ranging from 3 to 4 pmol mol^{-1} was evident in the FT

759   around 500 to 600 mb extending from approximately 60°S southward to the pole (Fig. 5a).

760   This was driven by the condensation of HBr transported from the MBL across a band

761   between 40°S to 20°S into the FT, southward, leading to the subsequent production (followed

762   by volatilization and photolysis) of Br$_2$ via

763                      $HOBr(aq) + Br^- + H^+ \rightarrow Br_2(aq)$ (R8)
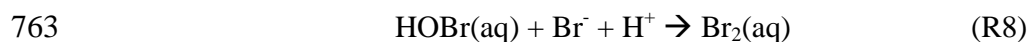
764   Reactions R1 through R4 and R5 through R7 complete the autocatalytic cycle. A recent paper

765   by Roscoe et al. (2012) concluded that a large potential discrepancy between surface and

766   remote-sensing measurements of BrO in Antarctica was resolved by a high abundance of

767   BrO in the FT above the surface. . This conclusion is supported by measured vertical profiles

768   of BrO showing a maximum of nearly 9 pmol mmol^{-1} at an altitude of 2 km (approx. 700 to

769   800 mb). The general consistency between these observations and our moded results suggests

770   that a significant amount of the BrO involved in chemistry over the Antarctic ice sheet is sea-

771   salt derived. Further, McElroy et al. (1999) saw evidence for a high abundance of BrO in the

772   Arctic FT that the authors were only able to conclude was driven by multiphase chemistry.

773   While we cannot confirm that our results are indeed reflective of the true nature of these

774   observations, they demonstrate a consistent regional-scale performance of our model's

775   halogen cycling mechanism.

776   Measurements and model calculations indicate that, in the MBL, volatile inorganic Br

777   typically has a relatively longer atmospheric lifetime against deposition than the parent

778   marine aerosol (e.g., Sander et al., 2003; Keene et al., 2009). In addition, our model

779   calculations indicate that significant amounts of relatively insoluble forms of Br$_t$ are

780   detrained from the MBL and accumulate in the FT whereas most of the highly soluble parent

781   aerosol is largely confined to the MBL. Br cycling in the FT leads to enrichments in

782   particulate Br relative to inorganic sea salt (i.e., EF(Br) > 1) throughout most of the FT (see

783　Supplement Tables S1 and S2). Two pathways lead to accumulation of Br in aerosols: (1) In

784　the FT, secondary Br^- is formed via the oxidation of aqueous SO_2 (in the form of HSO_3^- and

785　SO_3^{2-}) by HOBr, and (2) the condensation of HBr onto newly formed and preexisting aerosol.

786　The subsequent entrainment from the FT into the PBL of both Br-enriched aerosols and HBr,

787　most of which subsequently condenses onto existing MBL aerosols, contributes to Br^-

788　enrichments in the PBL. The role of this dynamic process is evident in a slight but

789　statistically significant ($p<0.10$) negative correlation between HBr and model vertical

790　velocity (not shown). The incorporation of secondary Br^- into fine-mode particles formed via

791　nucleation, and subsequent coagulation into accumulation-mode particles likely affects

792　EF(Br) across the size distribution, as well. However, since the model does not distinguish

793　between fresh and aged aerosols, the relative contributions of different pathways to simulated

794　EF(Br) in the PBL cannot be quantified explicitly.

795　　Br enrichments in sub-µm fraction aerosol have been observed throughout the MBL (e.g.,

796　Sander et al., 2003) but until now models have been unable to explain them. In a CAABA

797　box model, MECCA chemistry predicts efficient activation of particulate Br^- in all aerosol

798　size fractions (e.g., Keene et al., 2009) and, thus, no significant Br enrichment of marine

799　aerosol within the MBL. Our 3-D model calculations suggest that the detrainment of

800　relatively insoluble forms of Br_t from the MBL into the FT, chemical processing within the

801　FT, and the subsequent transport and entrainment of condensed or condensable reaction

802　products back into the MBL accounts for the Br enrichment of sub-µm aerosol size fractions

803　measured in the MBL. While Br is continuously cycled through the aerosol population even

804　in low LWC environments, the equilibration with HBr(g) dominates the net Br exchange

805　leading to steady state enrichments of the smaller (yet more abundant at altitude) aerosols.

806　Both the zonal median EF(Br) for bulk aerosol in the model surface layer and available

807　measurements of EF(Br) (taken from Sander et al., 2003) indicate a slight NH latitudinal

808　gradient at high latitudes, which is more pronounced in the observations (Fig. 2). Sander et

809　al. (2003) suggest that the EF(Br) greater than unity in the NH may result from anthropogenic

810　Br emissions in the region (primarily the N. Sea and Scandinavia) leading to bulk

811　enrichments. While zonal averages are not directly comparable to individual observations,

812　the model suggests a stronger latitudinal trend in the SH. This is likely due to the strong

813　subsidence in the high latitudes, consistent with the hypothesized mechanism of fine aerosol

814　enrichment observed throughout the marine boundary layer. Sparse measurements in that

815　region provide limited information with which to evaluate the simulated pattern.

816   Geographically and seasonally coincident comparisons between simulated and measured

817   EF(Br) for size-resolved marine aerosol indicate strong agreement (Fig 3e-h).

818   Comparison of simulated and observed Br_t reveals a fairly consistent pattern of model

819   over-prediction. With the exception of the NE Atlantic adjacent to N. Africa, where the

820   agreement was good, the model over-predicted Br_t by factors of 2 to 6 (Table 2). It is

821   recognized that MECCA tends to overestimate Br_t as was the case in Keene et al. (2009)

822   where simulated Br_t was high by a factor of about 3 relative to observations. It is important to

823   note that, with the exception of Hawaii, the geographic locations in Table 2 were coincident

824   with large gradients in NO_x and Br_t. The relatively coarse model resolution in these regions

825   constrains the reliability of comparisons between observed and simulated values and

826   probably contributes to the divergence in results..

827   Observations using the OMI instrument aboard NASA's Aura satellite are capable of

828   constraining vertical abundances of BrO (reported as column abundances, cm^{-2}). It is difficult

829   to partition observations into the contribution of BrO from different altitudes to the total

830   column abundance. Vertically integrated simulated BrO (Fig. 4) ranged from 0.011 x 10^{13} to

831   4.9 x 10^{13} cm^{-2} (consistent with von Glasow et al., 2004) over the simulated 10-year annually

832   averaged period. Median BrO column burdens were 0.56 x 10^{13}, 0.97 x 10^{13}, and 0.58 x 10^{13}

833   cm^{-2} for DJF, MAM,and JJA periods, respectively. Corresponding median PBL BrO mixing

834   ratios were 1.1, 2.3 and 1.5 pmol mol^{-1} for DJF, MAM and JJA, respectively. Median FT

835   BrO was 0.15, 0.20 and 0.25 pmol mol^{-1} for DJF, MAM and JJA, respectively. Maximum

836   column integrated BrO for the MAM NH was 4.9 x 10^{13} cm^{-2}. An estimated tropospheric

837   maximum column burden of 3.9 ($\pm$ 2.5) x 10^{13} cm^{-2} was computed based on aircraft-based

838   observed profiles (Salawitch et al., 2010). Typical NH spring-time peak *total* column burdens

839   measured by satellite exceed our maximum values by a factor of ~2 (e.g. Richter et al., 2002).

840   These peaks typically occur over the polar ice-caps and are believed to be due to "bromine

841   explosions" during Arctic springtime (Simpson et al., 2007; Piot and von Glasow, 2008).

842   While all hypothesized sources specific to the Arctic are not considered here, the results

843   depicted in Fig. 4 provide a potentially useful background values for estimating the

844   contribution to total Br from sources other than activation pathways involving marine aerosol

845   (e.g., reactions involving brine films on surfaces, frost flowers, organobromine precursors,

846   downwelling of stratospheric BrO, etc.).

847   A subset of available measurements of BrO in the MBL is compared with the

848   corresponding average values in Table 3. The model output mixing ratios are averaged over

849   diel cycles. To estimate daytime mean mixing ratios from the diel averages, we assumed that

850   BrO mixing ratios dropped to zero at night and adopted the fraction of hours of daylight

851   appropriate for the time of year. Simulated daytime mixing ratios agreed with observations

852   within a factor of about 2 to 3 at all locations. The simulated BrO maxima in the tropical

853   Atlantic and Pacific MBL (Fig. 5b) have not been probed via direct measurement. But, as

854   was the case with simulated Br_t, circulation and the coarse model resolution constrain the

855   reliability of comparisons between measurements and simulated results in regions of strong

856   chemical gradients. For example, mean BrO in grid boxes immediately to the east of that

857   corresponding to Sao Vicente, Cape Verde were a factor of two lower than that reported in

858   Table 3.

859   Throughout most of the lower troposphere and boundary layer, the BrO + NO reaction is

860   the largest source of atomic Br (Table 4). The exception is the southern MBL where BrO +

861   BrO, and HOBr and Br_2 photolysis dominate. In the global free troposphere simulated atomic

862   Br originates primarily from BrO + NO and HOBr photolysis in approximately equal

863   proportions. The dominant sources for simulated HOBr in the free troposphere are BrO +

864   HO_2 (84%) and BrO + CH_3O_2 (16%; primarily from CH_4 oxidation). As the result of low

865   liquid water content, Br radicals in the free troposphere recycle primarily in the gas phase;

866   though as discussed above, heterogeneous recycling is also important.

867

868   3.2.2 Cl Distributions

869   Simulated HCl mixing ratios are high in comparison with available measurements in the

870   MBL. For example, Pszenny et al. (2003) measured HCl ranging from <30 to 250 pmol mol^{-1}

871   (mean, 100 pmol mol^{-1}) in on-shore flow within the Hawaiian MBL, compared to a simulated

872   surface median of 1247 (1046 to 1383) pmol mol^{-1}. The simulated values were driven by in

873   situ acidification of marine aerosol by high volcanic SO_2 emissions which were emitted at the

874   model surface. For comparison, simulated HCl upwind of the volcanic SO_2 plume was more

875   than a factor of two lower. HCl measured along a transect in the E. Atlantic MBL was 682

876   (106 to 1404) pmol mol^{-1} in the vicinity of the European continent, 348 (91 to 746) pmol mol^{-}

877   ^{1} adjacent to N. Africa, 82 (<23 to 207) pmol mol^{-1} in the Intertropical Convergence Zone,

878   and 267 (81 to 453) pmol mol^{-1} adjacent to S. Africa (Keene et al., 2009). Corresponding

879   simulated median surface HCl mixing ratios for these regions were 352 (8 to 1577), 906 (271

880   to 1914), 424 (294 to 697), and 445 (0.11 to 3155) pmol mol^{-1}, respectively. Maximum HCl

881   mixing ratios in the E. Atlantic were generally coincident with acid-displacement reactions

882 involving HNO_3 in marine regions downwind of major NO_x emission sources. As for Br_t, the

883 strong gradients along the cruise track constrain the reliability of comparisons between

884 measured and simulated HCl.

885   Differences between aerosol pH in *Hal* versus *NoHal* simulations reflect the influence of

886 HCl phase partitioning on aerosol solution acidity in the former versus lack thereof in the

887 latter (not shown). Acid displacement of HCl by HNO_3 and other relatively more soluble

888 acids transfers acidity from the aerosol solution to the gas phase and thereby sustains higher

889 solution pHs in the *Hal* simulation (e.g., Keene et al., 1998). For all locations at which

890 published estimates of aerosol pH based on in situ observations were available, simulated

891 pHs based on *Hal* compared better with those estimates than did pHs based on *NoHal* (not

892 shown; also see Keene et al., 2009).

893   Simulated Cl^* mixing ratios in the PBL are higher over much of the NH high-latitudes,

894 relative to other regions, with peak values in marine-influenced air downwind of major

895 population and industrial regions. This is due to interactions with high anthropogenic NO_x

896 emissions (see Section 3.3.3). Simulated Cl^* in the SH-MBL (ranging from less than 0.01 to

897 340 pmol mol^{-1}, median 27 pmol mol^{-1}) was comprised of 46%, 16%, 6% and 1% BrCl, Cl_2

898 (on a molecular basis), HOCl, and $ClNO_2$, respectively, based on median values. Cl^* in the

899 NH MBL was comprised of 20%, 29%, 3% and 10% BrCl, Cl_2, HOCl, and $ClNO_2$,

900 respectively, based on median values. In contrast, over NH continents, $ClNO_2$ made up 69%

901 of Cl^* and was higher than $ClNO_2$ in the NH-MBL by a factor of 10 (see Supplemental Table

902 S4). This reflects the differences in NO_x loadings between both continental and marine

903 troposphere, and the southern and northern hemispheres. In the MECCA chemical

904 mechanism, $ClNO_2$ is produced at night and subsequently photolyzes following sunrise via

905 $$N_2O_5 + Cl^- \rightarrow ClNO_2 + NO_3^- \quad\quad\quad (R9)$$

906 $$ClNO_2 + h\nu \rightarrow Cl + NO_{2;} \quad\quad\quad (R10)$$
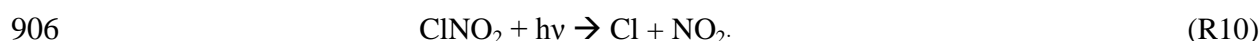
907 Significant production is limited to highly polluted conditions with NO_x mixing ratios greater

908 than ~1 nmol mol^{-1}. There is some evidence of the importance of $ClNO_2$ cycling over coastal

909 and continental regions (e.g. Ostoff et al., 2008, Simon et al. 2009, Thornton et al. 2010;

910 Phillips et al. 2012). Mean simulated $ClNO_2$ mixing ratios in the summer time surface layer

911 adjacent to the U.S. Texas Gulf Coast were 134 (± 51) pmol mol^{-1} and were consistent with

912 both observations made by Osthoff et al. (2008) and non-polluted simulation results (Simon

913 et al., 2009). Mean simulated $ClNO_2$ mixing ratios for February at Boulder, CO USA (40°N

914 105°W) were 129 (± 38) pmol mol^{-1}, which is within the range of $ClNO_2$ mixing ratios

915   observed by Thornton et al. (2010) in this region (ranging from less than 1 to 210 pmol mol[-]

916   [1]). The simulated distribution of $ClNO_2$ over N. America (Fig. 6) is also generally consistent

917   with production patterns based on the GEOS-Chem model (Thornton et al., 2010). $ClNO_2$

918   mixing ratios simulated by Hal are generally higher and extend over broader geographic

919   regions downwind from continents relative those simulated by Erickson et al. (1999), and

920   compare well with limited observations. During a March-April 2008 cruise in the North

921   Atlantic, Kercher et al. (2009) report nighttime $ClNO_2$ mixing ratios from 100 to 250 pmol

922   mol[-1] within the Long Island sound (coordinates not reported; assumed in the vicinity of

923   41.5°N, 70°W), and at or near 25 to50 pmol mol^{-1} further offshore (45°N, 55°W). Simulated

924     $ClNO_2$ mixing ratios within the corresponding grid cells, adjusted by a factor of two to

925   account for day length were 302 (± 88.4) pmol mol^{-1} and 75.6 (± 36.3) pmol mol^{-1},

926   respectively.. The broad distribution of $ClNO_2$ in the high latitudes suggests that its transport

927   and cycling is important as a source for atomic Cl and a nocturnal reservoir for NO_x in

928   polluted continental and marine regions.

929   Simulated atomic Cl in the global MBL ranged from 0 to 8.4 x 10^4 cm^{-3}, which brackets

930   reported values inferred from measurements of NMHCs and C_2Cl_4 (0 to ~10^5 cm^{-3}; Rudolph

931   et al, 1996, Singh et al, 1996). The simulated atomic Cl concentration of 2.6±1.5 x 10^4 cm^{-3} in

932   New England (USA) coast air during summer was within the corresponding range of

933   estimates based on relative concentration changes in NMHCs (2 x 10^4 to 6 x 10^4 cm^{-3};

934   Pszenny et al., 2007). An estimate of 3.3±1.1 x 10^4 cm^{-3} derived from measurements made

935   during a N. Atlantic cruise in June 1992 (Wingenter et al., 1996), was similar to a simulated

936   value of 4.8±1.6 x 10^4 cm^{-3} for the same region. Measurements in the southern ocean MBL

937   yielded estimated atomic Cl concentrations of 720±100 cm^{-3} which is a factor of two lower

938   than our simulated summertime surface mean of 2.0±1.6 x 10^3 cm^{-3} (Wingenter et al., 1999).

939   The ANN-SH-MBL median for simulated values (3.5 x 10^3 cm^{-3}) was within the estimated

940   0.26 x 10^4 to 1.8 x 10^4 cm^{-3} required to sustain observed CH_4 isotope ratios in the southern

941   MBL (Allan et al., 2001; Platt et al., 2004).

942   We note that, unless otherwise indicated, model output is based on monthly averages that

943   do not reflect daytime maxima; and thus peak mixing ratios for species produced

944   photochemically in ambient air are higher. In addition, the simulation did not consider non-

945   marine sources for Cl in the atmosphere and thus the total production fluxes and burdens of

946   Cl should be considered lower limits.

947

948   3.3 Impact of Halogens on O_3, OH, HO_2 and NO_x

949   3.3.1 O_3

950   Deviations between the *Hal* and *NoHal* simulations of zonally averaged surface O_3 (Fig.

951   7) and the corresponding zonal-median vertical distribution fields (see Supplemental Figure

952   S3) reveal less O_3 globally in the *Hal* simulation. These results are driven primarily by (1) the

953   direct destruction of O_3 via reaction with halogen radicals (Table 5) and (2) the net reduction

954   in O3 production resulting from the accelerated oxidation of NO_x via formation and

955   processing of halogen nitrates (discussed in more detail below; Sander et al., 1999; Pszenny

956   et al., 2004; Keene et al., 2009). The largest absolute deviations were in the high latitudes and

957   generally coincident with relatively greater direct destruction of O_3 via reaction with atomic

958   Br and NO (Fig. 7c). The reduction of NO_x and its influence on O_3 was also significant in the

959   free troposphere with a similar latitudinal pattern (mean deviation of -39%; not shown).

960   These results are not consistent with those from previous studies in two respects. First, the

961   geographic distribution of Br-mediated O_3 loss is different. Our simulation yields maximum

962   impacts in high latitudes whereas other studies report that tropical regions are impacted to a

963   greater degree (e.g. Yang et al., 2005; Sais-Lopez et al., 2012). The causes for these

964   differences are not entirely clear. In our study, the negative ozone deviations in high-latitude

965   MBL and polar PBL are coincident with higher NO and lower HO_2 concentrations (see

966   Section 3.3.2) relative to the *NoHal* simulations, which enhanced O_3 destruction via the NO +

967   O_3 reaction path. In regions where NO abundance decreased from *NoHal* to *Hal* (e.g. in the

968   remote tropical MBL) the net O_3 loss was also lower. Second, ozone loss is greater in our

969   simulations. Sais-Lopez et al. (2011) calculate net O_3 loss due to halogens from 6 to 20% in

970   the tropical troposphere. Our results exceed 20% for most of the tropical MBL and are

971   around 15 to 20% for the tropical FT. It is not clear if Sais-Lopez et al. (2012) also consider

972   the indirect destruction of ozone via changes in HO_x/NO_x abundance and partitioning.

973   In addition, the suppression of RO_2 production by BrO leads to a net decrease in RO_2

974   mixing ratios in the PBL. This suppressed the reaction of NO + RO_2 globally by 38% and

975   49% in the PBL and FT, respectively, thereby contributing to net O_3 destruction.

976   O_3 simulated with *Hal* and *NoHal* is compared with O_3 measured in near surface air at

977   Hawaii during September (Pszenny et al, 2004) and along a transect through the E. Atlantic

978   during October and November (Keene et al. 2009) in Figure 9. In all cases, the *Hal*

979   simulations yielded O_3 mixing ratios that were closer to those observed.

980   Annual mean O_3 mixing ratios for World Ozone and Ultraviolet Radiation Data Centre

981   (WOUDC) sites (Table 6) are compared to corresponding simulated O_3 mixing ratios in the

982   PBL and in the FT at the 500 mb pressure level in Fig. 10. Relative to mean mixing ratios

983   measured in the PBL and 500mb levels, deviations in mean (± standard deviation) O_3

984   simulated with *Hal* were -26% (±21%) and -27% (±12%), respectively. Corresponding

985   deviations based on NoHal were 42% (± 25%) and 9.3% (± 15%), respectively. For the PBL,

986   although the correlation coefficient for O3 based on *NoHal* was higher, the *Hal* simulations

987   better reproduce observed O_3 for nearly all stations (Fig. 10). Relative to *Hal*, or O_3 at the

988   500mb level simulated with *NoHal* were closer to observed O_3 mixing ratios.

989

990   3.3.2 OH:HO_2

991   Median OH and HO_2 mixing ratios in the PBL simulated with *Hal* were lower by 41% and

992   18%, respectively, relative to *NoHal*. Differences were greatest in the MBL and resulted

993   primarily from three processes. First, the enhancement of NO + HO_2 and the addition of BrO

994   + HO_2 → HOBr + O_2 (and subsequent uptake of HOBr by liquid aerosol) areHO_2 sinks.

995   HOBr uptake by aerosols in the MBL was approximately equivalent to OH recycling via

996   HOBr photolysis. Second, the accelerated rate of NO_2 oxidation by halogen species (section

997   3.3.3) reduced the production of HO_2. In combination with increased NO in the vicinity of

998   high HO_2 mixing ratios and lower O_3, this led to a net decrease in both OH and HO_2. Third,

999   globally less O_3 reduced the photochemical production of $O(^1D)$. Overall, the OH:HO_2 ratio

1000   decreased 28%, consistent with Keene et al. 2009 (3% to 32% decrease).

1001

1002   3.3.3 NO_x

1003   The cycling of Cl and Br in the *Hal* simulations impacted distribution, speciation, and

1004   lifetimes of NO_x species in two ways. Under polluted conditions at night, N_2O_5 is produced

1005   from

1006 $NO_{2(g)} + O_{3(g)}$ → $NO_{3(g)} + O_{2(g)}$ (R11)

1007 $NO_{3(g)} + NO_{2(g)}$ ↔ $N_2O_{5(g)}$ (R12)
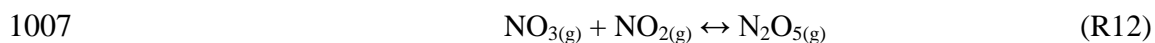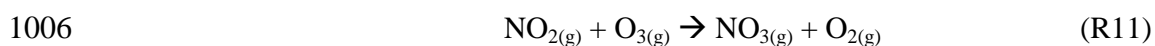
1008   Some N_2O_5 reacts with particulate Cl$^-$ to produce $ClNO_2$ via R9. In addition, N_2O_5 also

1009   hydrolyzes to produce HNO_3, which accounts for 30% to 50% of the total NO_x sink in

1010   polluted regions (Alexander et al., 2009). The photolysis of $ClNO_2$ following sunrise via R10

1011   regenerates half the NO_2 from which the precursor N_2O_5 was formed and also produces

1012 highly reactive Cl atoms. Thus, this pathway acts as both a source for halogen radicals and a

1013 nocturnal reservoir for NO_x that efficiently extends its atmospheric lifetime and thereby

1014 enhancing O_3 production relative to that predicted in the absence of R9 and R10 (as in

1015 *NoHal*). Figure 11a depicts the percent deviation of NO_x ($NO + NO_2$) in the PBL for *Hal*

1016 versus *NoHal* simulations. The increased NO_x lifetime resulting primarily from $ClNO_2$

1017 production and processing is evident in the positive deviations along the primary transport

1018 pathways downwind of major pollution sources.

1019   Under clearer conditions in the MBL, the formation and subsequent hydrolysis of halogen

1020 nitrates via

1021 $$NO_2 + ClO \rightarrow ClNO_3 \qquad \qquad (R13)$$

1022 $$ClNO_3 + H_2O(l) \rightarrow HOCl + HNO_3 \qquad \qquad (R14)$$
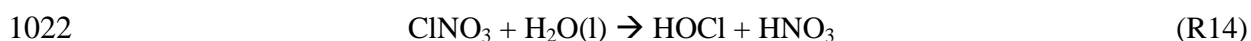
1023 and analogous reactions that produce $BrNO_3$ accelerates oxidation of NO_x (Sander et al.,

1024 1999; Pszenny et al., 2004; Keene et al., 2009). The influence of these reactions is evident in

1025 the negative deviations in NO_x simulated by *Hal* relative to *NoHal* for much of the global

1026 MBL (Fig. 11a) and in differences in median NO_x mixing ratios simulated with *Hal* versus

1027 *NoHal* for the NH MBL, SH MBL, and PBL. As noted above, the accelerated oxidation of

1028 NO_x via these pathways impacts oxidation processes through net O_3 and OH destruction and

1029 modified OH/HO_2 ratios. In the Antarctic region, the presence of increased Br, and less O_3

1030 and HO_x increased the lifetime of NO leading to a positive NO deviation while NO_2

1031 decreases (Fig. 11b & c).

1032

1033   3.4 Impact of Halogens on S Cycling

1034   In general, the global-scale sources, lifetimes, and sinks for major S species compare well

1035 with the modal-CAM standard chemical scheme and other global model studies of the S

1036 budget (Table 7). Major differences between MECCA and modal-CAM are driven in part by

1037 influences of halogens in the oxidation of DMS and SO_2, lower OH concentrations in the

1038 PBL in MECCA-CAM, and differences in the treatment of H_2SO_4.

1039   The primary DMS oxidation pathways in the conventional mechanism considered in most

1040 models are reaction with OH during daytime and reaction with NO_3 at night. DMS burden

1041 and lifetime in *NoHal* are about five times that in the standard modal-CAM, due to lower OH

1042 and NO_3 concentrations (factor of 2 to 3 for both) in the global PBL. The *Hal* and *NoHal*

1043 simulations calculate OH online while standard modal-CAM uses an offline oxidant database

1044   of monthly averages taken from simulations by a chemistry-climate model (Lamarque et al.,

1045   2010).

1046   Oxidation of DMS by BrO has been proposed as an important alternate pathway (Toumi,

1047   1994; von Glasow, 2002) and oxidation by atomic Cl may also be significant at high Cl-atom

1048   concentrations (Keene et al., 1996). Comparison of the major DMS reaction pathways is

1049   presented in Table 8. *Hal* simulations indicate that reaction with BrO is important throughout

1050   the whole atmosphere, and responsible for 84% of all DMS oxidation in the southern

1051   hemisphere MBL. Comparing the total oxidation rate shows that DMS is oxidized faster

1052   globally (Table 8, factor of 1.40 in the PBL) than would be predicted by the reaction with OH

1053   and NO_3 alone. Globally, median DMS mixing ratios were lower by 74% and 89% in the

1054   PBL and FT, respectively. The greatest differences in DMS mixing ratios were coincident

1055   with emissions patterns in the SH MBL (Fig. 13c), reflecting the faster oxidation in the *Hal*

1056   simulations. Positive DMS deviations were coincident with low relative mixing ratios.

1057   The SO_2 budgets for the *Hal* and *NoHal* simulations are quite similar. In comparison to

1058   the standard modal-CAM, the main difference is the lower gas-phase oxidation due to lower

1059   PBL OH concentration in MECCA-CAM, and slower aqueous uptake. In both *Hal* and

1060   *NoHal* simulations, oxidation by H_2O_2 in the cloud water aqueous phase was the single most

1061   important sink for SO_2 globally (Table 8). In the *Hal* simulation, oxidation of S(IV) in

1062   deliquesced aerosols accounted for about 12% of S(IV) oxidation in the SH MBL, but only

1063   1% globally. Aqueous-phase pathways for S(IV) oxidation in aerosol solutions are strongly

1064   pH dependent (Chameides and Stelson, 1992; Keene et al., 1998). For size fractions that

1065   overlap, simulated aerosol pH's based on *Hal* are reasonably representative of available

1066   estimates inferred from direct measurements (Fig. 3). The mediation of pH by acid-

1067   displacement in the *Hal* simulation resulted in a much greater uptake of SO_2 in aerosol (Fig.

1068   13b). $SO_2(g)$ and aerosol S(IV) simulated for the ANN-PBL by *Hal* versus *NoHal* (Fig. 13a,

1069   b) diverged by median values of -7.73% (-77.4% to 686%) and 428% (-99.9% to 1.87 x

1070 10^7%), respectively. These differences are driven primarily by the absence of acid-

1071   displacement reactions involving HCl and the associated low aerosol solution pHs (by 1 to 2

1072   units) in *NoHal*. Significant aqueous-phase oxidation of S(IV) by O_3 in aerosol solutions is

1073   limited to alkaline conditions (Chameides and Stelson, 1992) and, consequently, this pathway

1074   was important only in the SH where persistent high winds sustain high concentrations of

1075   marine aerosol (Long et al., 2011), sources of acidity are relatively low, and, thus pH values

1076   are relatively high (see Supplement). The lower pH of aerosol solutions in other regions

1077 efficiently suppressed aerosol S(IV) oxidation by O_3 in *Hal* simulations (Table 8). Aqueous-

1078 phase oxidation of S(IV) by HOCl and HOBr enhances production of S(VI) in moderately

1079 acidic (pH 5 to 6 aerosol solutions; Vogt et al., 1996; Keene et al., 1998; von Glasow et al.,

1080 2002) but production via these pathways decreases with decreasing pH due to the lower

1081 solubility of SO_2 (Keene et al., 2009). As noted above, aerosol pH values simulated by *Hal*

1082 are reasonably consistent with those derived from observations. The pH range of 5 to 6 is

1083 transient and, in most regions, acidified aerosols rapidly equilibrate with atmospheric acids at

1084 somewhat lower pHs. Consequently, *Hal* simulations indicate oxidation of S(IV) by

1085 hypohalous acids accounts for minor to negligible fractions of S(IV) oxidation in the MBL

1086 globally (Table 8). Differences in our results compared to von Glasow et al. (2002) were due

1087 to the inability to differentiate between cloudy and non-cloudy conditions in our monthly-

1088 mean model datasets, whereas von Glasow et al. (2002) were able to explicitly differentiate

1089 processes under clear-sky and cloudy conditions.

1090   The most noticeable budget differences between CAM/MECCA and the standard modal-

1091 CAM are for H_2SO_4 vapor. In *Hal* and *NoHal*, the H_2SO_4 source (from SO_2 reaction with

1092 OH) is smaller but the burden and lifetime are higher, which was driven by several factors.

1093 First, the lower PBL OH concentrations in *Hal* and *NoHal* result in more SO_2 being mixed

1094 into the FT where the total aerosol surface area and liquid water content are low and

1095 $H_2SO_4(g)$ loss by condensation is relatively slow resulting in higher burdens and lifetimes.

1096 Modal-CAM calculates H_2SO_4 vapor production (by gas-phase chemistry) and uptake by

1097 aerosols sequentially, while *Hal* and *NoHal* calculate them simultaneously, which has been

1098 shown to affect H_2SO_4 vapor concentrations (Kokkola et al., 2009). In addition, modal-CAM

1099 uses the Fuchs-Sutugin equation to calculate H_2SO_4 mass-transfer rates from gas to particle

1100 phases, whereas *Hal* and *NoHal* use the method of Schwartz (1986), yielding mass-transfer

1101 rates generally slower in *Hal* and *NoHal* than in modal-CAM (Sander, 1999). A more

1102 detailed evaluation of differences in the simulated H_2SO_4 vapor concentrations is beyond the

1103 scope of this study. The higher $H_2SO_4(g)$ concentrations in the FT also lead to higher rates of

1104 nucleation and growth of new particles in *Hal* and *NoHal*. Particle number concentrations

1105 based on enhanced nucleation in *Hal* yielded reasonably good agreement with observations

1106 from a wide range of locations (Table 9), while other studies report underestimations of

1107 concentrations under similar conditions (Adams and Seinfeld, 2002; Spracklen et al., 2005).

1108 These differences are important to aerosol microphysics in the FT, and thus deserve further

1109   investigation. However, they do not significantly impact the budget or distribution of nss-

1110 SO_4^{2-} in the simulations.

1111   The global nss-SO_4^{2-} budgets for *Hal* and *NoHal* were nearly indistinguishable, while

1112   compared to a 5-year simulation of the standard modal-CAM, the nss- SO_4^{2-} burden and

1113   lifetimes were 30% to 40% higher (Table 7). Globally, nss- SO_4^{2-} shifted to smaller size bins

1114   driven by transport and subsequent oxidation of SO_2 from the PBL into the FT in the CAM-

1115   MECCA system versus standard modal-CAM. While the *Hal* and *NoHal* global S budgets are

1116   close, there are regional differences approaching ±30% for PBL concentrations. In the NH

1117   PBL, nss-SO_4^{2-} was generally higher in *Hal* (Fig. 12d) due to enhanced gas-phase and

1118   aqueous-aerosol oxidation of SO_2 (Fig. 12b), less oxidation in cloud droplets, and the shorter

1119   lifetime of nss-SO_4^{2-} produced in cloud droplets. Lower nss-SO_4^{2-} in the Indian and SE Asian

1120   PBL was driven in part by an ~10% increase rain and wet removal. Effects of interactions

1121   between chemistry, weather and climate will be addressed in a subsequent paper. The largest

1122   relative (Fig. 12d) and absolute (not shown) nss-SO_4^{2-} positive deviations occurred

1123   immediately downwind of large anthropogenic sources of SO_2 in eastern. China and the

1124   eastern USA. This was due to higher aerosol pH leading to more SO_2 uptake (Fig. 12a & b).

1125   Directly further upwind from these nss-SO_4^{2-} deviation maxima, aqueous S(IV) deviations

1126   become negative, indicating enhanced oxidation of S(IV) by aqueous halogen radicals (HOCl

1127   and HOBr). In addition, a significant positive global correlation between nss-SO_4^{2-} and

1128   aerosol liquid water ($R^2 = 0.55$; $p<0.01$) in the PBL suggests a non-linear positive feedback

1129   link between aerosol hygroscopicity and its ability to take up and oxidize SO_2 in the aqueous

1130   phase. In the SH, the nss-SO_4^{2-} burden decreased by 19% on average, due to faster gas-phase

1131   oxidation of DMS (primarily by BrO) and somewhat lower yield of SO_2, more efficient

1132   uptake of SO_2 in larger aerosol particles with higher pH, and faster deposition of the nss-

1133 SO_4^{2-} formed in the larger particles (see Tables 7 and 8). Based on comparisons with

1134   observations, *Hal* and *NoHal* provided similar resolution in predicting mean annual SO_2 and

1135   nss-SO_4^{2-} (Fig. 13, Table 10).

1136   Relative to the conventional pathways considered in *NoHal* and most other models, the

1137   net global effects of halogen chemistry on S cycling in marine air are accelerated oxidation of

1138   DMS thereby reducing its atmospheric lifetime. Despite relatively large influences on some

1139   pathways in the marine S cycle (Table 7), the domination of S cycling by continental and

1140   anthropogenically influenced air masses (where halogen chemistry is relatively less

1141   important) and by non-halogen aqueous chemistry in clouds limited the overall net effect of

1142   halogens on the atmospheric S budget . However, simulated results suggest potential non-

1143   linear feedbacks that may significantly alter nss-SO_4^{2-} distributions downwind of major

1144   sources.

1145

1146   3.5 Halogen Interactions NMHC, CH_4

1147   The oxidation of CH_4 and NMHC's is the primary source of O_3 in the troposphere through

1148   the production of organic peroxy-radicals that short-circuit the destruction of O_3 by NO.

1149   Relative to the *NoHal*, reactions involving halogens in *Hal* decreased the total rate of CH_3O_2

1150   formation by 9% and 13% in the PBL and FT, respectively, and total CH_3O_2 destruction by

1151   2% and 14% in the PBL and FT, respectively. These reactions resulted in lower steady-state

1152   mixing ratios of CH_3O_2 throughout most of the global troposphere (not shown). CH_3O_2 in the

1153   FT did not vary significantly between the two runs.

1154   Averaged globally, in combination with lower OH plus reaction with atomic Cl, CH_4

1155   oxidation rates decreased by 3% relative to the *NoHal* simulation. The corresponding

1156   oxidation rates in the continental and marine boundary layer were higher by 13% and 9%,

1157   respectively, reflecting the production of atomic Cl in the lower atmosphere. While atomic Cl

1158   mixing ratios were comparable to (sparse) inferred observations, simulated CH_4 mixing ratios

1159   were fixed throughout the atmosphere. As such, these results are considered upper limits.

1160

1161   4. Discussion

1162   The study presented here compared simulated multiphase chemistry of the atmosphere

1163   based on chemical reactions involving inorganic Cl and Br. Comparisons between the *Hal*

1164   and *NoHal* simulations demonstrate that a multiphase chemical mechanism is capable of

1165   reproducing major, and in some cases previously unresolved, characteristics of the aerosol

1166   and gas-phase chemical composition of the atmosphere including gas-phase Cl and Br

1167   species and aerosol pH. Further, this work suggests that much of the observed distribution

1168   and impact of halogens and related chemical cycling in the PBL and lower FT may be

1169   explained with sea-salt derived Cl and Br alone. Results also highlight the role of

1170   meteorology and circulation in observations of reactive halogens and aerosol composition.

1171   The reproduction of observed EF(Br) and EF(Cl), and the model's dependence upon

1172   interactions between the FT and PBL in the enrichment process strongly suggests (1) that

1173   halogen cycling is important in the FT, (2) that FT halogen cycling is tightly coupled with

1174   PBL chemistry, and (3) global-scale circulation and dynamics play a large role in the global

1175   distribution, partitioning and impacts of inorganic Cl and Br species. The results also suggest

1176   that SO_2 oxidation by HOBr and HOCl primarily in the FT plays a central role in this

1177   dynamic connection.

1178   Comparison with observations indicate the *Hal* simulations reproduced tropospheric O_3 in

1179   the MBL with reasonable confidence, and that systematic biases in O_3 simulated with

1180   conventional chemical schemes were directly and indirectly attributable to reactions

1181   involving halogens. Reactions involving halogens destroyed significant quantities of O_3

1182   throughout the MBL and the global troposphere. These pathways included direct destruction

1183   via reaction with halogen radicals and the accelerated regional oxidation of NO_x via the

1184   formation and processing of halogen nitrates. *Hal* simulations indicate that the formation and

1185   processing of $ClNO_2$ in the polluted NH PBL increases the atmospheric lifetime and transport

1186   of NO_x, alters NO/NO_2 partitioning; and activates significant atomic Cl with associated

1187   implication for oxidation processes.

1188   Nss-SO_4^{2-} lifetimes were extended immediately downwind of major sources of SO_2 due to

1189   the enhanced uptake of SO_2 by higher pH aerosol in the *Hal* simulation versus *NoHal*. The

1190   oxidation DMS and to a lesser extent S(IV) by halogens in the MBL significantly modified

1191   regional S cycling relative to that based on conventional chemical pathways considered in

1192   most models. DMS oxidation was enhanced by the reaction with BrO and Cl, accounting for

1193   60% of DMS oxidation throughout the entire troposphere. In the *Hal* simulation, reactions in

1194   aqueous aerosol particles accounted for 12% of the total S(IV) oxidation in the SH MBL, but

1195   only about 1% globally. Reaction with HOCl and HOBr in moderately acidic aerosol

1196   solutions increased S(IV) oxidation rates in the PBL by only 1.2%. Overall, halogen

1197   chemistry increased rates of S(VI) production from precursors.

1198   Systematic differences in Br_t and Br species suggest a high sensitivity of the chemical

1199   system driven by these simulations to multiphase exchange of soluble gas-phase species. It is

1200   important to note that published values of Henry's Law constants (K_H) of several species

1201   governing gas/aerosol partitioning vary by large amounts. Published values K_H's for Br_2,

1202   BrCl and HBr all vary by factors of two or greater (see http:// www.henrys-law.org for a

1203   detailed discussion and compilation of Henry's Law constants).

1204   Major influences of halogen cycling on radiation, precipitation, and related climate

1205   processes will be evaluated in detail in a follow-up manuscript. The results presented here

1206   have important implications for feedbacks between the atmospheric chemistry and climate

1207   system and anthropogenically forced changes in atmospheric composition. The continued

1208   expansion of the human population and global-scale industrialization will certainly result in

1209   increased emissions of acids and acid precursors. The results herein suggest that throughout

1210   most of the unpolluted southern hemisphere, halogen radical chemistry is already important.

1211   The increased acidification of marine aerosol in this region would lead to increased activation

1212   of halogen species with associated implications. It has been hypothesized that, at pH levels

1213   observed in the remote marine atmosphere, modest increases in acidity in this region would

1214   yield disproportionately large increases in Cl and Br activation rates (Sander et al., 2003).

1215   This study suggests that large-scale changes in halogen activation at the surface would

1216   impact the entire troposphere. The long-term implications of increased activation, though,

1217   cannot be assessed in the with short-term simulation studies such as this.

1218   In addition, current projections indicate that climate change will alter global and regional

1219   wind fields. Since marine aerosol production scales exponentially with wind speed, such

1220   changes would have major consequences for the production, atmospheric concentrations, and

1221   processing of marine aerosol.. Although the feedbacks cannot be assessed directly from this

1222   study, our results suggest that they would be significant. For example, in most regions, the

1223   larger size fractions that dominate production fluxes of marine aerosol mass are significantly

1224   debrominated during their atmospheric lifetime (e.g., Keene et al., 2009). Consequently, in

1225   MBL regions with sufficient acidity to titrate marine-derived alkalinity, available evidence

1226   suggests that enhanced wind-driven production of marine aerosols will lead to more vigorous

1227   Br-radical chemistry and associated feedbacks on tropospheric composition. Lastly, inorganic

1228   Br is believed to be a primary Hg oxidant in the atmosphere and may control Hg's

1229   atmospheric lifetime and deposition (Holmes et al., 2010). Large-scale emission of Hg to the

1230   atmosphere in South America associated with artisanal gold mining, combined with the

1231   potential for accelerated release of reactive Br into the Southern Hemisphere due to

1232   industrialization could pose a significant regional- to global-scale hazard.

1233   Future research to address these issues would require the capacity to run century-scale

1234   simulations using a fully-coupled (with an ocean model) configuration. To this end, the

1235   computational limitations of the system used here are prohibitively large. Additional effort is

1236   needed to increase the efficiency of the chemical solution and improve the capacity to store

1237   data.

1238   Still, several immediate research questions are apparent. Available evidence suggests that

1239   the production and processing of some compounds that are not considered in the current

1240   chemical mechanism are or may be import in atmospheric chemistry. These include (1)

1241 organic Cl^- and Br^- containing compounds that are hypothesized to be the major sources of

1242 halogen radicals to the upper troposphere and stratosphere (see Sander et al., 2003 and

1243 references therein) and (2) iodocarbons and perhaps I_2 that are emitted from the ocean surface

1244 and significantly impact photochemistry and redox cycles in the MBL (Read et al., 2008;

1245 Sais-Lopez et al., 2011). Finally, large uncertainties in the parameterization of transfer

1246 coefficients and thermodynamic properties of some compounds (e.g., Henry's Law constants

1247 for Br species) must be resolved to improve our current understanding of and ability to

1248 reliably simulate multiphase processes.

1249

1250 5. References

1251 Adams, P. J., and J. H. Seinfeld, Predicting global aerosol size distributions in general

1252   circulation models, J. Geophys. Res., 107(D19), 4370, doi:10.1029/2001JD001010, 2002.

1253 Alexander, B., Hastings, M. G., Allman, D. J., Dachs, J.: Thornton, J. A., and Kunasek, S. A.,

1254   Quantifying atmospheric nitrate formation pathways based on a global model of the

1255   oxygen isotopic composition ($\Delta^{17}O$) of atmospheric nitrate, Atmos. Chem. Phys., 9, 5043-

1256   5056, doi:10.5194/acp-9-5043-2009, 2009.

1257 Allan, W., Lowe, D. C., and Cainey, J. M.: Active chlorine in the remote marine boundary

1258   layer: Modeling anomalous measurements of d13C in methane, Geophys. Res. Lett., 28,

1259   3239–3242, 2011.

1260 Andreae, M. O., and Rosenfeld, D.: Aerosol-cloud-precipitation interactions. Part 1. The

1261   nature and sources of cloud-active aerosols, Earth Science Reviews 89, 13-41, 2008.

1262 Anastasio, C., and Newberg, J. T.: Sources and sinks of hydroxyl radical in sea-salt particles.

1263   J. Geophys. Res., 112, D10306, doi:10.1029/2006JD008061, 2007..

1264 Birmili, W., Wiedensohler, A., Heintzenberg, J., and Lehmann, K.: Atmospheric particle

1265   number size distribution in central Europe: Statistical relations to air masses and

1266   meteorology, J. Geophys. Res.-Atmos., 106, 32 005–32 018, 2001.

1267 Boville, B. A., Rasch, P. J., Hack, J. J., and McCaa, J. R.: Representation of clouds and

1268   precipitation processes in the Community Atmosphere Model Version 3 (CAM3). J.

1269   Climate, 19(11), 2184-2198, 2006.

1270 Briegleb, B.P., Hunke, E.C., Bitz, C.M., Lipscomb, W.H., Holland, M.M., Schramm, J.L.,

1271   Moritz, R.E.: The sea ice simulation of the Community Climate System Model, version 2.

1272   Nat. Center for Atm. Res. Tech Rep no. NCAR-TN-455, Boulder, CO, 34pp, 2004.

1273 Chameides, W. L., and Stelson, A. W.: Aqueous-phase chemical processes in deliquescent

1274   sea-salt aerosols: A mechanism that couples the atmospheric cycles of S and sea salt, J.

1275   Geophys. Res., 97, 20,565-20,580, 1992.

1276 Clarke, A. D., Owens, S. R., and Zhou, J.: An ultrafine sea salt flux from breaking waves:

1277   Implications for cloud condensation nuclei in the remote marine atmosphere, J. Geophys.

1278   Res., 111, D06202, doi:10.1029/2005JD006565, 2006.

1279 Dentener, F., Kinne, S., Bond, T., Boucher, O., Cofala, J., Generoso, S., Ginoux, P., Gong,

1280   S., Hoelzemann, J., Ito, A., Marelli, L., Penner, J., Putaud, J.-P., Textor, C., Schulz, M.,

1281   Werf, G.v.d., and Wilson, J.: Emissions of primary aerosol and precursor gases in the

1282   years 2000 and 1750 -prescribed data-sets for AeroCom, Atmos. Chem. Phys., 6, 4321-

1283   4344, 2006.

1284 Dickerson, R. R., K. P. Rhoads, T. P. Carsey, S. J. Oltmans, J. P. Burrows, and P. J. Crutzen,

1285   Ozone in the remote marine boundary layer: A possible role for halogens, J. Geophys.

1286   Res., 104, 21385-21395, 1999.

1287 Dickinson, R.E., Oleson, K.W., Bonan, G.B., Hoffman, F., Thornton, P., Vertenstein, M.,

1288   Yang, Z.-L., Zeng, X.: The Community Land Model and it's cliamte statistics as a

1289   component of the Community Climate System Model. J. Clim., 19, 2302-2324, 2006.

1290 Erickson III, D. J., Seuzaret, C., Keene, W.C., and Gong, S.L.: A general circulation model

1291   based calculation of HCl and $ClNO_2$ production from sea salt dechlorination: Reactive

1292   Chlorine Emissions Inventory, J. Geophys. Res., 104(D7), 8347–8372,

1293   doi:10.1029/98JD01384, 1999.

1294 Fitzenberger, R., Bösch, H., Camy‑Peyret, C., Chipperfield, M.P., Harder, H., Platt, U.,

1295   Sinnhuber, B.-M., Wagner, T., and Pfeilsticker, K.: First profile measurements of

1296   tropospheric BrO, Geophys. Res. Lett., 27(18), 2921-2924, 2000.

1297 Galbally, I. E., Bentley, S.T., and Meyer, C.P.: Mid-latitude marine boundary-layer ozone

1298   destruction at visible sunrise observed at Cape Grim, Tasmania, Geophys. Res. Lett., 27,

1299   3841-3844, 2000.

1300 Gent, P. R., Yeager, S. G., Neale, R. B., Levis, S., and Bailey, D. A.: Improvements in a half

1301   degree atmosphere/land version of the CCSM, Climate Dynamics, doi:10.1007/s00382-

1302   009-0614-8, 2009.

1303 Granier, C., Guenther, A., Lamarque, J., Mieville, A., Müller, J., Olivier, J., Orlando, J.,

1304   Peters, 20 J., Petron, G., Tyndall, G., and Wallens, S.: POET, a database of surface

1305   emissions of ozone precursors, available at http://www.aero.jussieu.fr/

1306   projet/ACCENT/POET.php, 2005.

1307   Gregg, W. W.: Assimilation of SeaWIFS global ocean chlorophyll data into a three-

1308   dimensional global ocean model, J. Mar. Sys., 69, 205–225, 2008.

1309   Holmes, C. D., Jacob, D. J., Corbitt, E. S., Mao, J., Yang, X., Talbot, R., and Slemr, F.:

1310   Global atmospheric model for mercury including oxidation by bromine atoms, Atmos.

1311   Chem. Phys., 10, 12037-12057, doi:10.5194/acp-10-12037-2010, 2010.

1312   Kamra, A. K., Murugavel, P., and Pawar, S. D.: Measured size distributions of aerosols over

1313   the Indian Ocean during INDOEX, J. Geophys. Res., 108(D3), 8000,

1314   doi:10.1029/2002JD002200, 2003.

1315   Keene, W. C., Jacob, D. J., and Fan, S.-M.: Reactive chlorine: A potential sink for

1316   dimethylsulfide and hydrocarbons in the marine boundary layer, Atmos. Environ., 30(6),

1317   i-iii, 1996.

1318   Keene, W. C., Sander, R., Pszenny, A. A. P., Vogt, R., Crutzen, P.J., and Galloway, J.N.:

1319   Aerosol pH in the marine boundary layer: A review and model evaluation, J. Aerosol Sci,

1320   29, 339-356, 1998.

1321   Keene, W. C., Stutz, J., Pszenny, A. A. P., Maben, J. R., Fischer, E., Smith, A. M., von

1322   Glasow, R., Pechtl, S., Sive, B. C., and Varner, R. K.: Inorganic chlorine and bromine in

1323   coastal New England air during summer, J. Geophys. Res., 112 (D10), D10S12, 2007.

1324   Keene, W. C., Long, M. S., Pszenny, A. A. P., Sander, R., Maben, J. R., Wall, A. J.,

1325   O'Halloran, T. L., Kerkweg, A., Fischer, E. V., and Schrems, O.: Latitudinal variation in

1326   the multiphase chemical processing of inorganic halogens and related species over the

1327   eastern North and South Atlantic Oceans, Atmos. Chem. Phys., 9, 7361-7385,

1328   doi:10.5194/acp-9-7361-2009, 2009.

1329   Kercher, J. P., Riedel, T. P., and Thornton, J. A.: Chlorine activation by N_2O_5: simultaneous,

1330   in situ detection of $ClNO_2$ and N_2O_5 by chemical ionization mass spectrometry, Atmos.

1331   Meas. Tech., 2, 193-204, doi:10.5194/amt-2-193-2009, 2009.

1332   Kerkweg, A., Sander, R., Tost, H., Jöckel, P., and Lelieveld, J.: Technical Note: Simulation

1333   of detailed aerosol chemistry on the global scale using MECCA-AERO, Atmos. Chem.

1334   Phys., 7, 2973-2985, doi:10.5194/acp-7-2973-2007, 2007.

1335   Kerkweg, A., Jöckel, P., Pozzer, A., Tost, H., Sander, R., Schulz, M., Stier, P., Vignati, E.,

1336   Wilson, J., and Lelieveld, J.: Consistent simulation of bromine chemistry from the marine

1337   boundary layer to the stratosphere, Part I: model description, sea salt aerosols and pH,

1338   Atmos. Chem. Phys., 8, 5899–5917, 2008.

1339   Kokkola, H., Hommel, R., Kazil, J., Niemeier, U., Partanen, A.-I., Feichter, J., and

1340   Timmreck, C.: Aerosol microphysics modules in the framework of the ECHAM5 climate

1341   model – intercomparison under stratospheric conditions, Geosci. Model Dev. Discuss., 2,

1342   209-246, doi:10.5194/gmdd-2-209-2009, 2009.

1343   Lamarque, J.-F., Bond, T. C., Eyring, V., Granier, C., Heil, A., Klimont, Z., Lee, D.,

1344   Liousse, C., Mieville, A., Owen, B., Schultz, M. G., Shindell, D., Smith, S. J.,

1345   Stehfest, E., Van Aardenne, J., Cooper, O. R., Kainuma, M., Mahowald, N.,

1346   McConnell, J. R., Naik, V., Riahi, K., and van Vuuren, D. P.: Historical (1850–2000)

1347   gridded anthropogenic and biomass burning emissions of reactive gases and aerosols:

1348   methodology and application, Atmos. Chem. Phys., 10, 7017-7039, doi:10.5194/acp-10-

1349   7017-2010, 2010.

1350   Lawler, M. J., Finley, B. D. Keene, W. C., Pszenny, A. A. P., Read, K. A., von Glasow, R.,

1351   and Saltzman, E. S.: Pollution-enhanced reactive chlorine chemistry in the eastern

1352   tropical Atlantic boundary layer, Geophys. Res. Lett., 36, L08810,

1353   doi:10.1029/2008GL036666, 2009.

1354   Leitte, A.M., Schlink, U., Herbarth, O., Wiedensohler, A., Pan, X., Hu, M., Richter, M.,

1355   Wehner, B., Tuch, T., Wu, Z., Yang, M., Liu, L., Breitner, B., Cyrys, J., Peters, A.,

1356   Wichmann, H., and Franck, U.: Size-Segregated Particle Number Concentrations and

1357   Respiratory Emergency Room Visits in Beijing, China, Environ. Health Perspect.,

1358   119(4), 508–513, 2011.

1359   Liu, X., Easter, R. C., Ghan, S. J., Zaveri, R., Rasch, P., Shi, X., Lamarque, J.-F., Gettelman,

1360   A., Morrison, H., Vitt, F., Conley, A., Park, S., Neale, R., Hannay, C., Ekman, A. M. L.,

1361   Hess, P., Mahowald, N., Collins, W., Iacono, M. J., Bretherton, C. S., Flanner, M. G., and

1362   Mitchell, D.: Toward a minimal representation of aerosols in climate models: description

1363   and evaluation in the Community Atmosphere Model CAM5, Geosci. Model Dev., 5,

1364   709-739, doi:10.5194/gmd-5-709-2012, 2012.

1365   Long, M. S., Keene, W. C., Easter, R., Sander, R., Kerkweg, A., Erickson, D., Liu, X., and

1366   Ghan, S.: Implementation of the chemistry module MECCA (v2.5) in the modal aerosol

1367   version of the Community Atmosphere Model component (v3.6.33) of the Community

1368   Earth System Model, Geosci. Model Dev. Discuss., 5, 1483-1501, doi:10.5194/gmdd-5-

1369   1483-2012, 2012.

1370 Mårtensson, E.M., E.D. Nilsson, G. deLeeuw, L.H. Cohen, Hansson, H.-C.: Laboratory
1371   simulations and parameterization of the primary marine aerosol production, J. Geophys.
1372   Res., 108 (D9), doi:10.1029/2002JD002263, 2003.

1373 Mäkelä J. M., Koponen, I. K., Aalto, P., and Kulmala, M.: One-year data of submicron size
1374   modes of tropospheric background aerosol in southern Finland, J. Aerosol Sci., 31, 595–
1375   611, 2000.

1376 McDow, S. R., Jang, M., Hong, Y., and Kamens R.M.: An approach to studying the effects
1377   of organic composition on atmospheric aerosol photochemistry, J. Geophys. Res., 101,
1378   19,593-19,600, 1996.

1379 McElroy, C. T., McLinden, C. A., and McConnell, J. C.: Evidence for bromine monoxide in
1380   the free troposphere during the Arctic polar sunrise, Nature, 397, 338–340, 1999.

1381 Monahan, E.C. and O'muircheartaigh, I.G.: Whitecaps and the passive remote-sensing of the
1382   ocean surface, Int. J. Rem. Sens., 7 (5), 627-642, 1986.

1383 Montzka, S. A., Butler, J. H., Hall, B. D., Mondeel, D. J., and Elkins, J. W.: A decline in
1384   tropospheric organic bromine, Geophys. Res. Lett., 30, 1826,
1385   doi:1810.1029/2003GL017745, 2003.

1386 Nagao I., Matsumoto, K., and Tanaka, H.: Sunrise ozone destruction found in the sub-tropical
1387   marine boundary layer, Geophys. Res. Lett., 26, 3377-3380, 1999.

1388 O'Dowd, C. D., and Smith, M. H.: Physico-chemical properties of aerosol over the North
1389   East Atlantic: Evidence for wind speed related sub-micron sea-salt aerosol production, J.
1390   Geophys. Res., 98, 1137-1149, 1993.

1391 O'Dowd, C. D., Smith, M. H., Consterdine, I. E., and Lowe, J. A.: Marine aerosol, sea-salt,
1392   and the marine sulphur cycle: A short review, Atmos. Environ., 31, 73–80, 1997.

1393 Osthoff, H. D., Roberts, J. M., Ravishankara, A. R., Williams, E. J., Lerner, B. M.,
1394   Sommariva, R., Bates, T. M., Coffman, D., Quinn, P. K., Dibb, J. E., Stark, H.,
1395   Burkholder, J. B., Talukdar, R. K., Meagher, J., Fehsenfeld, F. C., and Brown, S. S.: High
1396   levels of nitryl chloride in the polluted subtropical marine boundary layer, Nature
1397   Geosci., 1, 324-328, doi:10.1038/ngeo177, 2008.

1398 Phillips, G. J., Tang, M. J., Thieser, J., Brickwedde, B., Schuster, G., Bohn, B., Lelieveld, J.,
1399   and Crowley, J. N.: Significant concentrations of nitryl chloride observed in rural
1400   continental Europe associated with the influence of sea salt chloride and anthropogenic
1401   emissions, Geophys. Res. Lett., 39, L10811, doi:10.1029/2012GL051912, 2012.

1402   Pierce, J. R. and Adams, P. J.: Global evaluation of CCN formation by direct emission of sea
1403   salt and growth of ultrafine sea-salt, J. Geophys. Res., 111, D06203,
1404   doi:10.1029/2005JD006186, 2006.
1405   Piot, M. and von Glasow, R.: The potential importance of frost flowers, recycling on snow,
1406   and open leads for ozone depletion events: Atmos. Chem. Phys., 8, 2437-2467,
1407   doi:10.5194/acp-8-2437-2008, 2008.
1408   Platt, U., Allan, W., and Lowe, D.: Hemispheric average Cl atom concentration from
1409   13C/12C ratios in atmospheric methane, Atmos. Chem. Phys., 4, 2393-2399,
1410   doi:10.5194/acp-4-2393-2004, 2004.
1411   Pszenny, A. A. P., Moldanová, J., Keene, W. C., Sander, R., Maben, J. R., Martinez, M.,
1412   Crutzen, P. J., Perner, D., and Prinn, R. G.: Inorganic halogens and aerosol pH in the
1413   Hawaiian marine boundary layer, Atmos. Chem. Phys., 4, 147-168, 2004.
1414   Pszenny, A. A. P., Fischer, E.V., Russo, R.S., Sive, B.C., and Varner, R.K.: Estimates of Cl
1415   atom concentrations and hydrocarbon kinetic reactivity in surface air at Appledore Island,
1416   Maine (USA), during International Consortium for Atmospheric Research on Transport
1417   and Transformation/Chemistry of Halogens at the Isles of Shoals, J. Geophys. Res., 112,
1418   D10S13, doi:10.1029/2006JD007725, 2007.
1419   Read, K. A., Majajan, A.S., Carpenter, L.J., Evans, M.J., Faria, B.V.E., Heard, D.E.,
1420   Hopkins, J.R., Lee, J.D., Moller, S.J., Lewis, A.C., Mendes, L., McQuaid, J.B., Oetjen,
1421   H., Saiz-Lopez, A., Pilling, M.J., and Plane, J.M.C.: Extensive halogen mediated ozone
1422   destruction over the tropical Atlantic Ocean, Nature, 453, 1232–1235, 2008.
1423   Richter, A., F. Wittrock, Ladstätter-Weißenmayer, A., and Burrows, J.P.: GOME
1424   measurements of stratospheric and tropospheric BrO, Adv. Space Res., 29(11), 1667-
1425   1672, 2002.
1426   Riley, J. P., Chester, R. and Duce, R. A.: Chemical oceanography. Vol. 10. SEAREX : the
1427   Sea/Air Exchange Program / edited by J.P Riley and R. Chester Academic, 1989.Roscoe,
1428   H. K., Brough, N., Jones, A. E., Wittrock, F., Richter, A., Van Roozendael, M., and
1429   Hendrick, F.: Resolution of an important discrepancy between remote and in-situ
1430   measurements of tropospheric BrO during Antarctic enhancements, Atmos. Meas. Tech.
1431   Discuss., 5, 5419-5448, doi:10.5194/amtd-5-5419-2012, 2012.
1432   Roscoe, H. K., Brough, N., Jones, A. E., Wittrock, F., Richter, A., Van Roozendael, M., and
1433   Hendrick, F.: Resolution of an important discrepancy between remote and in-situ

1434   measurements of tropospheric BrO during Antarctic enhancements, Atmos. Meas. Tech.

1435   Discuss., 5, 5419-5448, doi:10.5194/amtd-5-5419-2012, 2012.

1436   Rudolph, J., Koppmann, R., Plass-Duelmer, C.: The budgets of ethane and tetrachloroethene:

1437   Is there evidence for an impact of reactions with chlorine atoms in the troposphere?,

1438   Atmos. Environ., 3010, 1887–1894, 1996.

1439   Ruuskanen, J., Tuch, T., Brink, H., Peters, A., Khlystov, A., Mirme, A., Kos, G.P.A.,

1440   Brunekreef, B., Wichmann, H.E., Buzorius, G., Vallius, M., Kreyling, W.G., and

1441   Pekkanen, J.: Concentrations of ultrafine, fine and PM2.5 particles in three European

1442   cities, Atmos. Env., 35(21), 3729–3738, doi:10.1016/S1352-2310(00)00373-3, 2011.

1443   Saiz-Lopez, A., Plane, J. M. C., and Shillito, J.A., Bromine oxide in the mid-latitude marine

1444   boundary layer, Geophys. Res. Lett., 31(3), doi:10.1029/2004GL03111, 2004.

1445   Saiz-Lopez, A., Lamarque, J.-F., Kinnison, D. E., Tilmes, S., Ordóñez, C., Orlando, J. J.,

1446   Conley, A. J., Plane, J. M. C., Mahajan, A. S., Sousa Santos, G., Atlas, E. L.,

1447   Blake, D. R., Sander, S. P., Schauffler, S., Thompson, A. M., and Brasseur, G.:

1448   Estimating the climate significance of halogen-driven ozone loss in the tropical marine

1449   troposphere, Atmos. Chem. Phys., 12, 3939-3949, doi:10.5194/acp-12-3939-2012, 2012.

1450   Salawitch, R. J., Canty, T. P., Kurosu, T. P., Chance, K., Liang, Q., Pawson, S., Bhartia, P.

1451   K., Liu, X., Huey, L. G., Dibb, J. E., Simpson, W. R., Donohoue, D., Weinheimer, A. J.,

1452   Flocke, F. M., Neuman, J., Nowak, J. B., Ryerson, T. B., Oltmans, S. J., Blake, D. R.,

1453   Atlas, E. L., Kinnison, D. E., Tilmes, S., Pan, L., Hendrick, F., van Roozendael, M.,

1454   Kreher, K., Johnston, P. V., Pierce, R., Crawford, J. H., Jacob, D. J., A da Silva, Nielsen,

1455   J. E., Rodriguez, J. M., Liao, J., Stickel, R. E., Tanner, D. J., Knapp, D., Montzka, D.,

1456   Gao, R. S., Bui, T. P., Chen, G.: A new interpretation of total column BrO during Arctic

1457   spring, Geophys. Res. Lett., 37, doi:10.1029/2010GL043798, 2010.

1458   Sander, R.: Modeling atmospheric chemistry: Interactions between gas-phase species and

1459   liquid cloud/aerosol particles, Surv. Geophys., 20, 1–31, 1999.

1460   Sander, R., Rudich, Y., von Glasow, R., and Crutzen, P. J.: The role of $BrNO_3$ in marine

1461   tropospheric chemistry: A model study, Geophys. Res. Lett., 26, 2858-2860, 1999.

1462   Sander, R., Keene, W. C., Pszenny, A. A. P., Arimoto, R., Ayers, G. P., Baboukas, V.,

1463   Chainey, J. M., Crutzen, P. J., Duce, R. A., Hönninger, G., Huebert, B. J., Maenhaut, W.,

1464   Mihalopoulos, N., Turekian, V.C., and van Dingenan, R.: Inorganic bromine in the

1465   marine boundary layer: A critical review, Atmos. Chem. Phys, 3, 1301-1336, 2003.

1466   Sander, R., Kerkweg, A., Jöckel, P., and Lelieveld, J.: Technical note: The new
1467   comprehensive atmospheric chemistry module MECCA, Atmos. Chem. Phys., 5,
1468   445-450, doi:10.5194/acp-5-445-2005, 2005.

1469   Savoie, D. L., Arimoto, R., Keene, W. C., Prospero, J. M., Duce, R. A., and Galloway, J. N.:
1470   Marine biogenic and anthropogenic contributions to non-sea-salt sulfate in the marine
1471   boundary layer over the North Atlantic Ocean, J Geophys. Res., 107(D18), 4356,
1472   doi:10.1029/2001JD000970, 2002.

1473   Schwartz, S. E.: Mass-transport considerations pertinent to aqueous phase reactions of gases
1474   in liquid-water clouds, in Chemistry of Multiphase Atmospheric Systems, NATO ASI
1475   Series, Vol. G6 , edited by W. Jaeschke, pp. 415–471, Springer Verlag, Berlin, 1986.

1476   Simon, H., Kimura, Y., McGaughey, G., Allen, D.T., Brown, S.S., Osthoff, H.D., Roberts,
1477   J.M., Byun, R., and Lee, D.: Modeling the impact of ClNO2 on ozone formation in the
1478   Houston area, J. Geophys. Res., 114, D00F03, doi:10.1029/2008JD010732, 2009.

1479   Simpson, W. R., von Glasow, R., Riedel, K., Anderson, P., Ariya, P., Bottenheim, J.,
1480   Burrows, J., Carpenter, L. J., Frieß, U., Goodsite, M. E., Heard, D., Hutterli, M.,
1481   Jacobi, H.-W., Kaleschke, L., Neff, B., Plane, J., Platt, U., Richter, A., Roscoe, H.,
1482   Sander, R., Shepson, P., Sodeau, J., Steffen, A., Wagner, T., and Wolff, E.: Halogens and
1483   their role in polar boundary-layer ozone depletion, Atmos. Chem. Phys., 7, 4375-4418,
1484   doi:10.5194/acp-7-4375-2007, 2007.

1485   Singh, H.B., Gregory, G.L., Anderson, B., Browell, E., Sachse, G.W., Davis, D.D.,
1486   Crawford, J., Bradshaw, J.D., Talbot, R., Blake, D.R., Thornton, D., Newell, R., Merrill,
1487   J: Low ozone in the marine boundary layer of the tropical Pacific Ocean: Photochemical
1488   loss, chlorine atoms, and entrainment, J. Geophys. Res., 101, 1907-1917, 1996.

1489   Spracklen, D. V., Pringle, K. J., Carslaw, K. S., Chipperfield, M. P., and Mann, G. W.: A
1490   global off-line model of size-resolved aerosol microphysics: I. Model development and
1491   prediction of aerosol properties, Atmos. Chem. Phys., 5, 2227-2252, doi:10.5194/acp-5-
1492   2227-2005, 2005.

1493   Stanier, C.O., Khlystov, A.Y., Pandis, S.N.: Ambient aerosol size distributions and number
1494   concentrations measured during the Pittsburgh Air Quality Study (PAQS). Atmos. Env.,
1495   38(20), 3275–3284, 2004.

1496   Tanaka, P. L., Riemer, D. D., Chang, S. H., Yarwood, G., McDonald-Buller, E. C., Apel, E.
1497   C., Orlando, J. J., Silva, P. J., Jimenez, J. L., Canagaratna, M. R., Neece, J. D., Mullins,

1498   C. B., and Allen, D. T.: Direct evidence for chlorine-enhanced urban ozone formation in
1499   Houston, Texas, Atmos. Environ., 37, 1393-1400, 2003.
1500   Textor, C., Schulz, M., Guibert, S., Kinne, S., Balkanski, Y., Bauer, S., Berntsen, T., Berglen,
1501   T., Boucher, O., Chin, M., Dentener, F., Diehl, T., Easter, R., Feichter, H., Fillmore, D.,
1502   Ghan, S., Ginoux, P., Gong, S., Grini, A., Hendricks, J., Horowitz, L., Huang, P., Isaksen,
1503   I., Iversen, I., Kloster, S., Koch, D., Kirkevåg, A., Kristjansson, J. E., Krol, M., Lauer, A.,
1504   Lamarque, J. F., Liu, X., Montanaro, V., Myhre, G., Penner, J., Pitari, G., Reddy, S.,
1505   Seland, Ø., Stier, P., Takemura, T., and Tie, X.: Analysis and quantification of the
1506   diversities of aerosol life cycles within AeroCom, Atmos. Chem. Phys., 6, 1777–1813,
1507   2006.
1508   Thornton, J.A., Kercher, J.P., Riedel, T.P., Wagner, N.L., Cozic, J., Holloway, J.S., Dubé,
1509   W.P., Wolfe, G.M., Quinn, P.K., Middlebrook, A.M., Alexander, B., and Brown, S.S.: A
1510   large atomic chlorine source inferred from mid-continental reactive nitrogen chemistry,
1511   Nature, 464, doi:10.1038/nature08905, 2010.
1512   Toumi, R.: BrO as a sink for dimethylsulfide in the marine atmosphere, Geophys. Res., Lett.,
1513   21, 117-120, 1994.
1514   Vignati E, de Leeuw, G., Berkowicz, R.: Modeling coastal aerosol transport and effects of
1515   surf-produced aerosols on processes in the marine atmospheric boundary layer J.
1516   Geophys. Res. 106, 20,225-20,238, 2001.
1517   Vogt, R., Crutzen, P. J., and Sander, R.: A mechanism for halogen release from sea-salt
1518   aerosol in the remote marine boundary layer, Nature, 383, 327-330, 1996.
1519   von Glasow R., Sander, R., Bott, A., and Crutzen, P. J.: Modeling halogen chemistry in the
1520   marine boundary layer. 2. Interactions with sulfur and cloud-covered MBL, J. Geophys.
1521   Res., 107, 4323, doi:10.1029/2001JD000943, 2002.
1522   von Glasow, R. and Crutzen, P. J.: Model study of multiphase DMS oxidation with a focus
1523   on halogens. Atmos. Chem. Phys., 4, 589 – 608, 2004.
1524   Wingenter, O.W., Kubo, M.K., Blake, N.J., Smith, Jr., T.W., Blake, D.R., and Rowland, F.S.:
1525   Hydrocarbon and halocarbon measurements as photochemical and dynamical indicators
1526   of atmospheric hydroxyl, atomic chlorine, and vertical mixing obtained during
1527   Lagrangian flights, J. Geophys. Res., 101, 4331-4340, 1996.
1528   Wingenter, O.W., Blake, D.R., Blake, N.J., Sive, B.C., Atlas, E., Flocke, F., and Rowland,
1529   F.S.: Tropospheric hydroxyl and atomic chlorine concentrations, and mixing time scales

1530   determined from hydrocarbon and halocarbon measurements made over the Southern

1531   Ocean, J. Geophys. Res., 104, 21,819-21,828, 1999.

1532   Yang, X., Cox, R. A., Warwick, N. J., Pyle, J. A., Carver, G. D., O'Connor, F. M., and

1533   Savage, N. H.: Tropospheric bromine chemistry and its impacts on ozone: A model

1534   study, J. Geophys. Res., 110, D23311, doi:10.1029/2005JD006244, 2005.

1535   Zhou X., Davis, A. J., Kieber, D. J., Keene, W. C., Maben, J. R., Maring, H., Dahl, E. E.,

1536   Izaguirre, M. A., Sander, R., and Smoydzyn, L.: Photochemical production of hydroxyl

1537   radical and hydroperoxides in water extracts of nascent marine aerosols produced by

1538   bursting bubbles from Sargasso seawater, Geophys. Res. Lett., 35, L20803,

1539   doi:10.1029/2008GL035418, 2008.

1540 Table 1. Global annual mean Na$^+$ burden, production flux, lifetime, dry and wet deposition fluxes, and global median (and range)
1541 aerosol number concentration compared with published results based on other marine aerosol source functions. Uncertainties
1542 correspond to year-over-year standard deviation for the 10-year annual mean.
1543

Study	Na$^+$ Burden (Tg)	Na$^+$ Source (10^3 Tg y^{-1})	Na$^+$ Lifetime (d)	Na$^+$ Dry Dep. (10^3 Tg y^{-1})	Na$^+$ Wet Dep. (10^3 Tg y^{-1})	Number Conc. (cm^{-3})
Hal (this work)	2.5 ± 0.03	1.1 ± 0.02	0.86 ± 0.01	0.49 ± 0.01	0.56 ± 0.01	266 (4.0x10^0 – 4.4x10^4)
Clarke et al. (2006)	4.0	2.2	0.66	1.5	0.68	
O'dowd et al. (1997)	5.2	4.1	0.47	2.9	1.2	
Mårtensson et al. (2003)	0.55	1.7	1.2	0.061	0.11	
Monahan et al. (1986)	1.2	0.55	0.79	0.34	0.19	
Kerkweg et al. (2008)	2.4	1.7	0.5	0.76	0.90	
Textor et al. (2006)	2.4	1.6	0.5			

1544

58

1545 Table 2. Median (and range) for total volatile Br (Br_t; pmol mol^{-1}) measured at Hawaii
1546 (Pszenny et al., 2004) and along a transect through the eastern North and South Atlantic
1547 Oceans (Keene et al., 2009) and statistics simulated for the surface layer within the
1548 corresponding grid cells. Reported median and ranges for simulated Br_t along the transect
1549 are based on a box bounded by the North-South/East-West limits of the transect segment,
1550 as reported in Keene et al. (2009).

Location and Time	Measured	Simulated
Hawaii (21°N, 158°W; Sep. 1999)	3.7 (<2 - 9)	22.7 (19.6 – 23.4)
NE Atlantic (43-51°N, 2°E-10°W; Oct. 2003)	7.2 (3.1 - 12.3)	17.5 (2.3 – 63.9)
NE Atlantic (10-33°N, 14-20°W; Oct.-Nov. 2003)	18.8 (8.2 - 30.1)	14.5 (7.2 – 29.5)
E Atlantic (1-10°N, 13-20°W; Nov. 2003)	2.4 (<0.1 - 3.1)	12.7 (8.5 – 22.2)
SE Atlantic (1N-18S, 4°E-13°W; Nov. 2003)	6.2 (4.4 - 10.1)	17.5 (0.1 – 44.4)

1551

Table 3. Measured and simulated BrO mixing ratios (pmol mol^{-1}) ± standard deviations (when available) for sites reported by Sander et al. (2003; Table 4) and Read et al. (2008). Simulated results are based on 10-year temporal means for the surface layer during the sampling month and within the grid-box corresponding to the measurements.

Location and Time	Measured	Simulated	Day/Night	Est. Daytime Mean
Hawaii (20°N, 155°W; Sep. 1999)	< 2	2.2 ± 0.20	1.96	4.2 ± 0.39
Finokalia, Crete (35°N, 26°E; Jul – Aug 2000)	<0.7 – 1.5	0.072 ± 0.040	1.68	0.12 ± 0.067
Made Head, Ireland (53°N, 10°W; Apr – May 1997)	1.1 – 2.5	1.1 ± 0.41	1.60	1.7 ± 0.66
Made Head, Ireland (53°N, 10°W; Sep - Oct 1998)	<1	0.96 ± 0.49	2.04	2.0 ± 1.0
Tenerife, Canary Islands (29°N, 17°W; Jun – Jul 1997)	3	3.0 ± 0.53	1.71	5.2 ± 0.9
Weybourne, Great Britain (53°N, 1°E; Oct 1996)	<2	0.018 ± 0.006	2.29	0.040 ± 0.013
São Vicente, Cape Verde (17°N, 25°W; Oct 2006 – Oct 2007)	2.5 ± 1.1[a]	2.9 ± 0.93	2.00	5.7 ± 2.4

[a]   Maximum daytime values reported by Read et al (2008). Nighttime values were below detection limits (0.5 – 1.0 pmol mol^{-1})

Table 4. Percentage contribution of different production pathways for atomic Br versus sum of all pathways based on ANN climatological means for different regions of the atmosphere.

	PBL	FT	Trop.	NH CBL	SH CBL	NH MBL	SH MBL
$BrO + NO \rightarrow Br + NO_2$	22%	30%	26%	61%	54%	27%	12%
$HOBr + hv \rightarrow Br + OH$	12%	27%	19%	5.6%	7%	9%	12%
$BrCl + hv \rightarrow Br + Cl$	18%	8.5%	14%	9.9%	9.2%	23%	15%
$Br_2 + hv \rightarrow Br + Br$	18%	11%	15%	18%	21%	17%	21%
$BrO + BrO \rightarrow 2\ Br + O_2$	15%	11%	13%	3.0%	5.9%	8.4%	23%
$BrO + ClO \rightarrow Br + OClO$	5.0%	5.8%	5.3%	1.0%	0.4%	5.4%	3.3%
$BrO + ClO \rightarrow Br + Cl + O_2$	4.3%	4.9%	4.4%	0.8%	0.4%	4.8%	2.9%
$BrO + DMS \rightarrow DMSO + Br$	2.9%	0.3%	1.8%	0.1%	0.5%	3.2%	8.0%
$BrO + CH_3O_2 \rightarrow Br + HCHO + HO_2$	2.0%	1.0%	1.6%	0.4%	0.4%	2.1%	2.1%
$BrNO_2 + hv \rightarrow Br + NO_2$	0.0%	0.0%	0.0%	0.4%	0.3%	0.0%	0.0%

Table 5. Relative contributions of different pathways to total direct O_3 destruction in *Hal* and in *NoHal* simulations and the corresponding total O_3 destruction via all pathways in *Hal* relative to *NoHal* simulations expressed as percentages; based on ANN means for different regions of the atmosphere.

	PBL	FT	NH CBL	SH CBL	NH MBL	SH MBL
Hal						
$R_{O3 + h\nu}$ / $R_{Hal\ Total}$	60%	41%	30%	34%	66%	74%
$R_{O3 + NO}$ / $R_{Hal\ Total}$	32%	39%	68%	60%	28%	8.1%
$R_{O3 + Br}$ / $R_{Hal\ Total}$	6.2%	15%	0.8%	1.3%	4.4%	16%
$R_{O3 + Cl}$ / $R_{Hal\ Total}$	0.6%	0.9%	0.2%	0.1%	0.7%	0.7%
NoHal						
$R_{O3 + h\nu}$ / $R_{NoHal\ Total}$	76%	56%	71%	38%	47%	78%
$R_{O3 + NO}$ / $R_{NoHal\ Total}$	23%	40%	27%	60%	49%	21%
$R_{Hal\ Total}$/$R_{NoHal\ Total}$	58%	76%	81%	74%	57%	38%

[1]Relatively lower rates of direct O_3 destruction via all pathways in *Hal* simulations are driven in part by relatively lower steady-state O_3 mixing ratios (see Fig. 7).

Table 6. WOUDC stations (and corresponding periods of record) at which the vertical profiles in O$_3$ evaluated herein were measured.

Station Code	Station Name	LAT	LON	Altitude (m)	Start Date	Stop Date
21	Edmonton	53.6	-114	766	Jan. 1980	Dec. 1993
24	Resolute	74.7	-95.0	40	Jan. 1980	Dec. 1993
67	Boulder	40.0	-105	1634	Jan. 1985	Dec. 1993
432	Tahiti	-18.0	-149	2	Jan. 1998	Dec. 1999
175	Nairobi	-1.27	36.9	1795	Jan. 1998	Dec. 2001
434	San Cristobal	-0.92	-89.6	8	Mar. 1998	Dec. 2001
435	Paramaribo	5.81	-55.2	25	Oct. 1999	Dec. 2001
191	Samoa	-14.3	-170	82	Apr. 1986	Dec. 2002
219	Natal	-5.84	-35.2	32	Jan. 1998	Dec. 2002
265	Pretoria	-25.6	28.2	1524	Jul. 1990	Dec. 2002
436	Reunion	-21.1	55.5	24	Jan. 1998	Dec. 2002
448	Malindi	-2.99	40.2	-6	Mar. 1999	Dec. 2002
437	Java	-7.57	112	50	Jan. 1998	Nov. 2002
438	Fiji	-18.1	178	6	Jan. 1998	Nov. 2002

Table 7. Global annual budgets for SO_2, H_2SO_4, nss-SO_4^{2-}, and DMS, for *Hal*, *NoHal* simulations, and a 5-year simulation using 3-mode modal-CAM (v3.6.33) with its standard chemical module. Ranges of results from previous studies are shown for comparison.

	Hal	*NoHal*	CAM 3.6.33	Previous Studies
SO_2				
Sources (Tg S/y)	79.3	80.6	84.4	83.0 – 124.6[b]
Emission	67.5	67.5	67.5	63.7 - 92.0[a]
DMS Oxidation	11.8	13.1	16.9	10.0 - 24.7[a]
Sink (Tg S/y)	80.5	82.8	87.0	
Dry Deposition	20.3	21.4	22.5	16.0 - 55.0[a]
Wet Deposition	14.7	13.8	14.6	0.0 - 19.9[a]
Gas Oxidation	6.2	6.4	11.9	6.1 - 16.8[a]
Aqueous Oxidation	39.3	41.2	38.0	24.5 - 57.8[a]
Burden (Tg S)	0.57	0.57	0.31	0.20 - 0.61[a]
Lifetime (d)	2.6	2.6	1.5	0.60 – 2.6[a]
H_2SO_4				
Source: SO_2 + OH	6.2	6.4	11.9	6.1 - 22.0[a]
Sink (Tg S/y)	5.9	6.2	11.8	
Nucleation	1.2	1.3	0.01	0.05-0.07[b]
Condensation	4.6	4.8	10.9	13.0 – 15.2[b]
Cloud Scavenging	0.1	0.1	0.9	
Burden (Tg S)	0.0029	0.0032	1.2×10^{-3}	9.0×10^6 - .001[a]
Lifetime (h)	4.1	4.4	0.086	0.12 - 0.17[a]
nss-SO_4^{2-}				
Sources (Tg S/y)	46.9	49.1	50.6	59.7 ± 13.2[a]
Emission	1.7	1.7	1.7	
Aqueous S(IV) Oxidation	39.3	41.2	38.0	
Microphysics[c]	5.9	6.2	10.9	
Sink (Tg S/y)	45.1	47.3	51.8	
Dry Deposition	11.8	12.7	10.3	
Wet Deposition	33.3	34.6	41.5	
Burden (Tg S)	0.86	0.88	0.67	0.66 ± 0.17[a]
Lifetime (h)	5.6	5.4	4.8	4.1 ± 0.74[a]
DMS				
Sources: Emission (Tg S/y)	18.3	18.3	18.3	10.7 - 23.7[a]
Sinks: Gas Oxidation (Tg S/y)	18.3	18.3	18.4	
Burden (Tg S)	0.032	0.15	0.029	0.02 - 0.15[a]
Lifetime (h)	0.64	3.0	0.57	0.024 – 0.13[a]

[a] From Liu et al. (2012) and references therein. [b] From Spracklen et al. (2005) and references therein.
[c] Combined source of nss-SO_4^{2-} due to H_2SO_4(g) nucleation, condensation, and scavenging.

Table 8. Relative contributions of different reaction pathways (R) to total DMS and S(IV) oxidation in *Hal* and in *NoHal* simulations and the corresponding total DMS and S(IV) oxidation via all pathways in *Hal* versus *NoHal* simulations expressed as percentages; based on ANN means, and spatial medians for different regions of the atmosphere. Subscripts *aq* and *cl* designate aerosol and cloud-water reactions, respectively.

	PBL	FT	Troposphere	NH CBL	SH CBL	NH MBL	SH MBL
DMS(Hal)							
$R_{DMS + OH}$ / $R_{DMS\text{-}Hal\text{-Total}}$	6.6%	27%	8.3%	9.3%	18%	12%	4.0%
$R_{DMS + NO3}$ / $R_{DMS\text{-}Hal\text{-Total}}$	11%	14%	11%	69%	53%	24%	3.8%
$R_{DMS + Cl}$ / $R_{DMS\text{-}Hal\text{-Total}}$	14%	8.4%	14%	9.3%	5.0%	20%	9.1%
$R_{DMS + BrO}$ / $R_{DMS\text{-}Hal\text{-Total}}$	68%	50%	67%	12%	24%	44%	82%
DMS(NoHal)							
$R_{DMS + OH}$ / $R_{DMS\text{-}NoHal\text{-Total}}$	54%	74%	57%	13%	31%	34%	66%
$R_{DMS + NO3}$ / $R_{DMS\text{-}NoHal\text{-Total}}$	46%	26%	43%	87%	69%	66%	34%
$R_{DMS\text{-}Hal\text{-Total}}$ / $R_{DMS\text{-}NoHal\text{-Total}}$[1]	140%	52%	122%	73%	43%	118%	227%

[1]Differences are driven in part by corresponding differences in steady state concentrations of DMS and S(IV) in *Hal* and *NoHal* simulation.

	PBL	FT	Troposphere	NH CBL	SH CBL	NH MBL	SH MBL
S(IV)(Hal)							
$R_{SO2 + OH}$ / $R_{S(IV)Total}$	11%	13%	11%	11%	5.7%	18%	6.5%
$R_{S(IV)aq + H2O2}$ / $R_{S(IV)-Hal-Total}$	1.3%	0.6%	1.2%	1.0%	0.2%	2.3%	2.0%
$R_{S(IV)aq + O3}$ / $R_{S(IV)-Hal-Total}$	0.1%	0.0%	0.1%	0.0%	0.1%	0.0%	0.8%
$R_{S(IV)aq + HOCl}$ / $R_{S(IV)-Hal-Total}$	0.9%	0.2%	0.8%	0.1%	0.0%	2.0%	4.9%
$R_{S(IV)aq + HOBr}$ / $R_{S(IV)-Hal-Total}$	0.2%	0.1%	0.2%	0.0%	0.0%	0.0%	2.0%
$R_{S(IV)cl + H2O2}$ / $R_{S(IV)-Hal-Total}$	74%	81%	75%	60%	90%	73%	81%
$R_{S(IV)cl + O3}$ / $R_{S(IV)-Hal-Total}$	12%	1.9%	11%	27%	4.2%	4.8%	2.1%
$R_{S(IV)cl + HOCl}$ / $R_{S(IV)-Hal-Total}$	0.2%	1.3%	0.4%	0.1%	0.0%	0.0%	0.2%
$R_{S(IV)cl + HOBr}$ / $R_{S(IV)-Hal-Total}$	0.6%	1.8%	0.8%	0.8%	0.2%	0.2%	0.5%
$R_{S(IV)aq}$ / $R_{S(IV)cl}$	2.8%	1.1%	2.6%	1.4%	0.3%	5.6%	12%
S(IV)(NoHal)							
$R_{SO2 + OH}$ / $R_{S(IV)-NoHal-Total}$	10%	14%	11%	8.5%	5.0%	17%	9.1%
$R_{S(IV)aq + H2O2}$ / $R_{S(IV)-NoHal-Total}$	1.1%	0.5%	1.0%	0.8%	0.1%	1.5%	1.9%
$R_{S(IV)aq + O3}$ / $R_{S(IV)-NoHal-Total}$	0.2%	0.0%	0.2%	0.0%	0.0%	0.0%	3.1%
$R_{S(IV)cl + H2O2}$ / $R_{S(IV)-NoHal-Total}$	76%	81%	76%	59%	90%	74%	83%
$R_{S(IV)cl + O3}$ / $R_{S(IV)-NoHal-Total}$	13%	5.1%	12%	31%	5.3%	7.5%	2.8%
$R_{S(IV)aq}$ / $R_{S(IV)cl}$	1.5%	0.6%	1.4%	0.9%	0.1%	1.9%	5.9%
$R_{S(IV)-Hal-Total}$ / $R_{S(IV)-NoHal-Total}$[1]	88%	88%	89%	88%	87%	86%	89%

[1]Differences are driven in part by corresponding differences in steady state concentrations of DMS and S(IV) in *Hal* and *NoHal* simulation.

Table 9: Mean particle number concentrations ± standard deviations when available (cm^{-3}) measured at surface locations and the median and range for number concentrations simulated with *Hal* in the surface layer of the corresponding grid cells. Simulated values are summed across all three particle modes.

| Location | Observed | Simulated (*Hal*) | | | Source |
		Median	Max	Min	
Alkmaar, Netherlands	25800±11300	2597	23508	815	Ruuskanen et al. 2001
Erfurt, Germany	25900±12200	2767	35180	759	Ruuskanen et al. 2001
Helsinki, Finland	20300±8200	2628	13134	610	Ruuskanen et al. 2001
Pittsburg, PA, USA	16470	13037	48678	2592	Stanier et al., 2004
Beijing, PRC	29000±10000	11340	66393	1697	Leitte et al., 2011
Indian Ocean (North of ITCZ)	856±232	324	1393	151	Kamra et al., 2003
Indian Ocean (ITCZ)	418±151	232	1277	74	Kamra et al., 2003
Indian Ocean (South of ITCZ)	334±20	277	884	104	Kamra et al., 2003
Melpitz, Germany	4830	2767	35180	759	Birmili et al. 2001 (as reported by Spracklen et al., 2005)
Hyytiälä, Finland	1813±1525	1708	7846	415	Mäkelä et al., 2000

Table 10. Correlation coefficients (R), normalized mean square error (NMSE), and mean deviations of measured $SO_2(g)$ and nss-SO_4^{2-} versus mean simulated values in the surface layer of the corresponding grid cell with *Hal* and *NoHal*, as plotted in Fig. 13. Continental measurement are from the IMPROVE network; and marine measurements are from the Atmosphere-Ocean Chemistry Experiment (AEROCE, Savoie et al., 2002), U.S. Department of Energy as the Environmental Measurements Laboratory (DOE-EML), and the Sea-Air Exchange Experiment (SEAREX, Riley et al., 1989).

		R	NMSE	Mean Deviation
	$SO_2(g)$	0.53	2.9	2.7 ($\pm$ 8.8)
Hal	Continental nss-SO_4^{2-}	0.87	0.083	0.59 ($\pm$ 2.0)
	Marine nss-SO_4^{2-}	0.93	0.083	1.9 ($\pm$ 2.6)
	$SO_2(g)$	0.54	2.8	2.6 ($\pm$ 8.8)
NoHal	Continental nss-SO_4^{2-}	0.82	0.095	0.55 ($\pm$ 2.2)
	Marine nss-SO_4^{2-}	0.89	0.086	2.1 ($\pm$ 2.6)
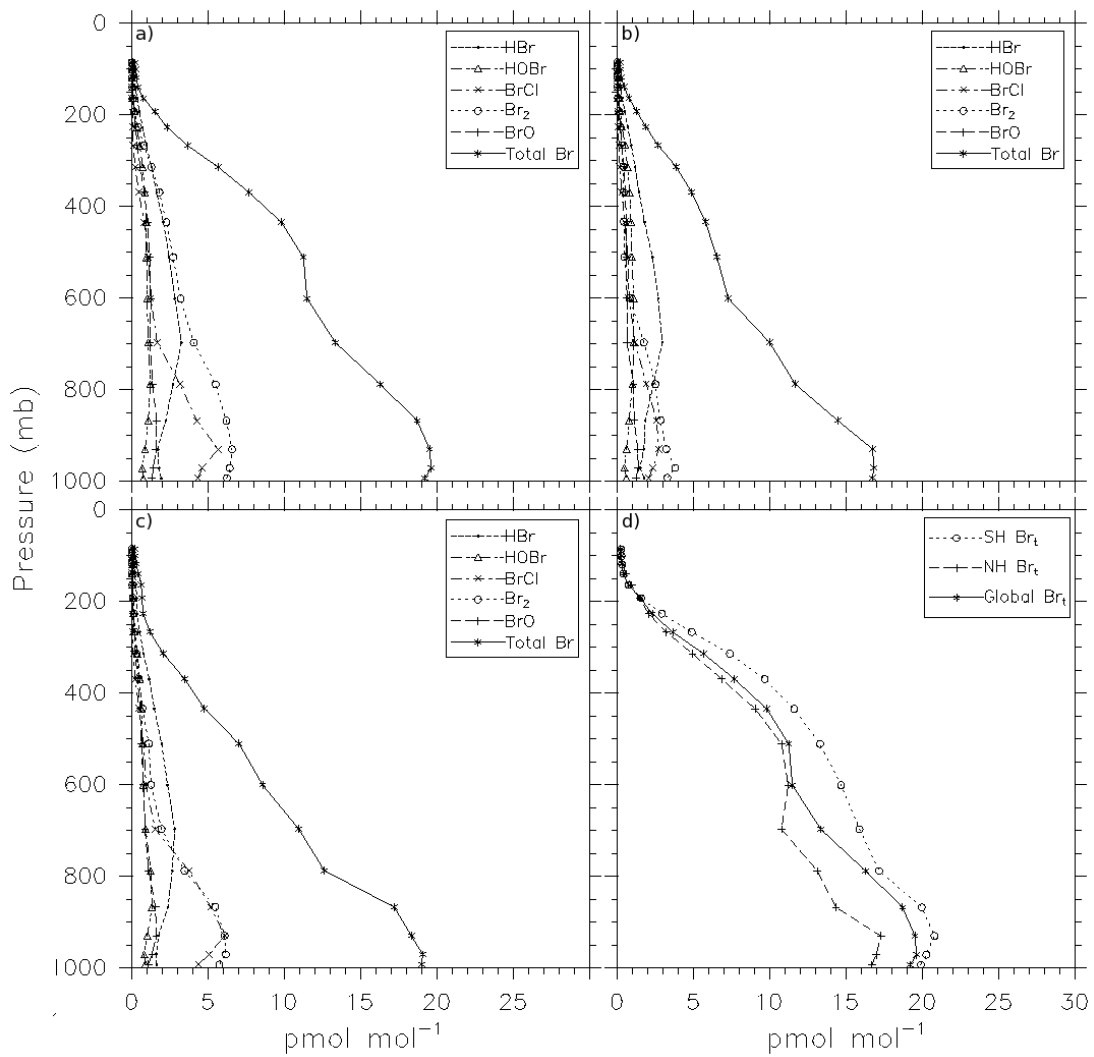
Figure 1. Spatial median vertical profiles of Br_t and its component gases for (a) ANN, (b) JJA, and (c) DJF; (d) ANN Br_t for NH, SH and global regions.
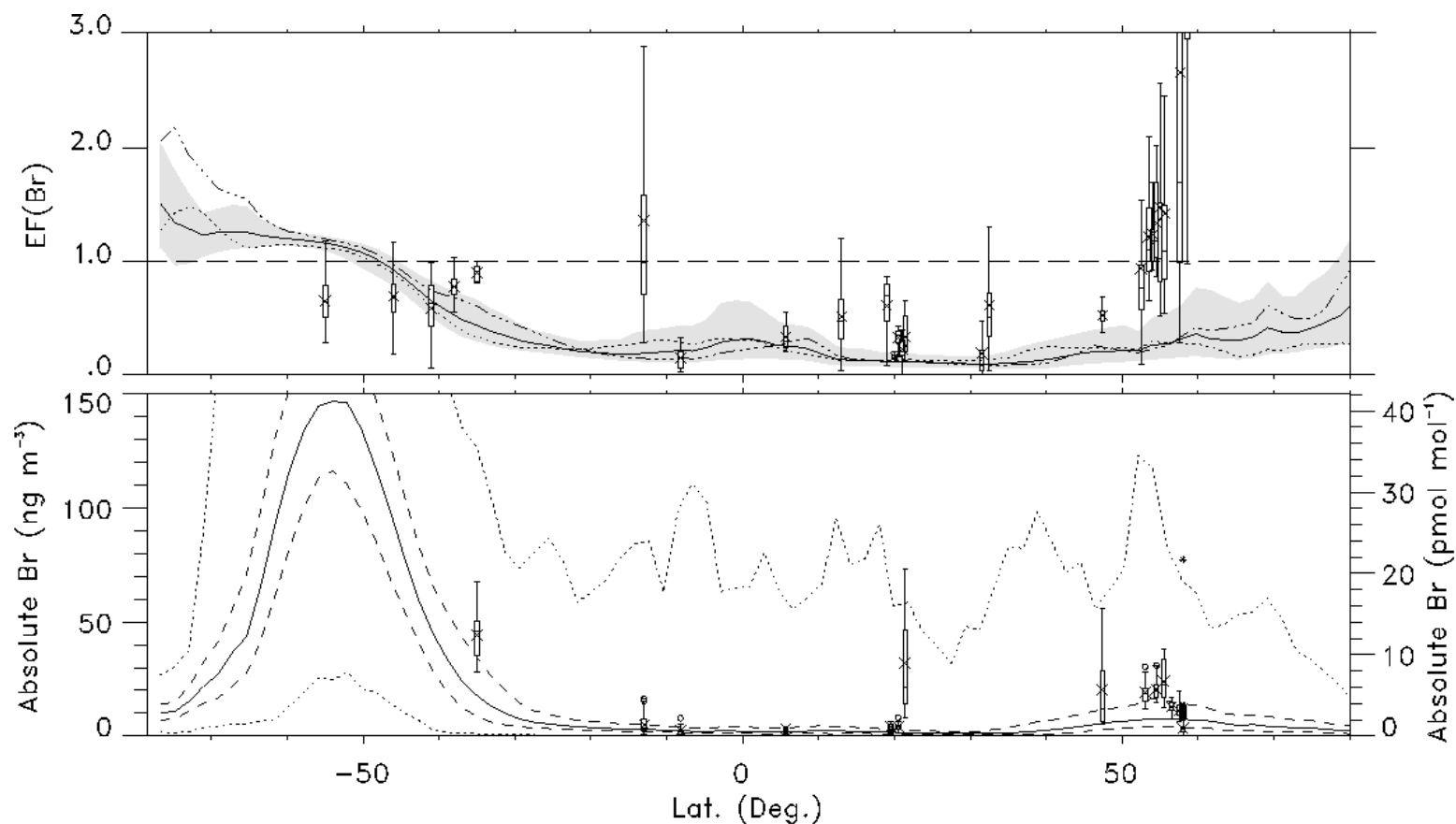
Figure 2. Simulated zonal (a) EF(Br) and (b) absolute Br⁻ concentration and the corresponding measurement values reported by Sander et al. (2003) and Keene et al. (2009). See Appendix A for a listing of measurement sources. Box-and-whiskers indicate minimum, 25th quartile, median, 75th quartile and maximum values where maxima and minima are of data within 1.5 times the 25th-75th quartile range. Crosses indicate means. In (a), simulated media are indicated by the solid line, the shaded area depicts 25th-75th quartile range, the dash-dotted line depicts the JJA median, and the dotted line depicts the DJF median. The horizontal dashed line indicates unity (i.e., no enrichment or depletion relative to conservative sea-salt species). In (b) simulated media are indicated by the solid line, 25th and 75th quartiles by the dashed lines, and maxima and minima by the dotted lines.

70
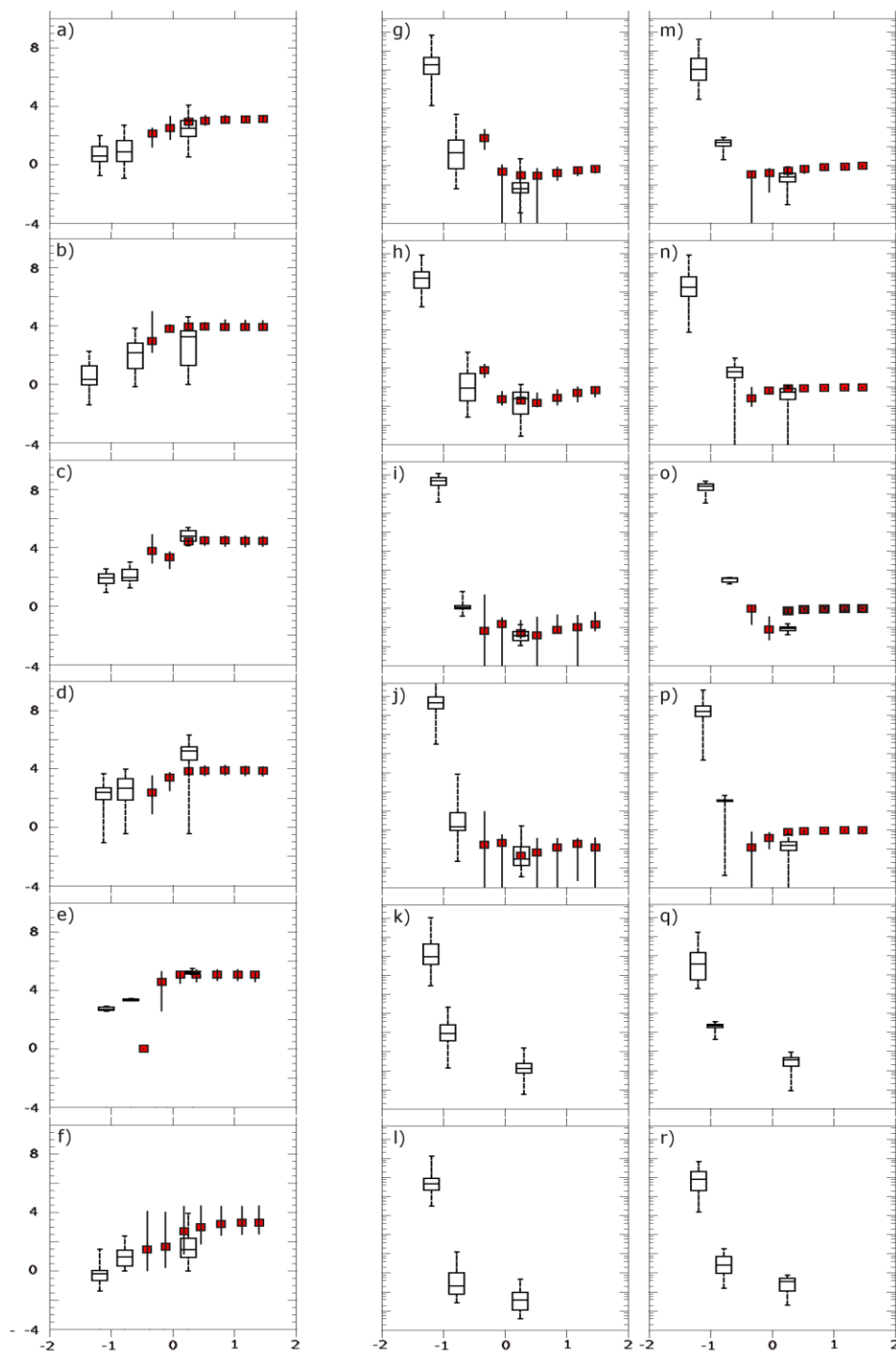
Figure 3. Size-resolved (a through f) pH inferred from measurements (g through j) and (where available) measured EF(Br) and (k through n) EF(Cl) (in red) and the corresponding values simulated with *Hal* (in black). Box-and-whiskers depict maximum, 75th quartile, median, 25th quartile, and minimum values. The top four rows correspond to the regions in the eastern North and South Atlantic Oceans reported by Keene et al. (2009): Row 1 is EURO, 2 is NAFR, 3 is ITCZ, and 4 is SATL. Row 5 corresponds to Hawaii (Pszenny et al., 2004), and Row 6 corresponds to the New England Air Quality Study (NEAQS) along the U.S. East Coast (Keene et al., 2004).
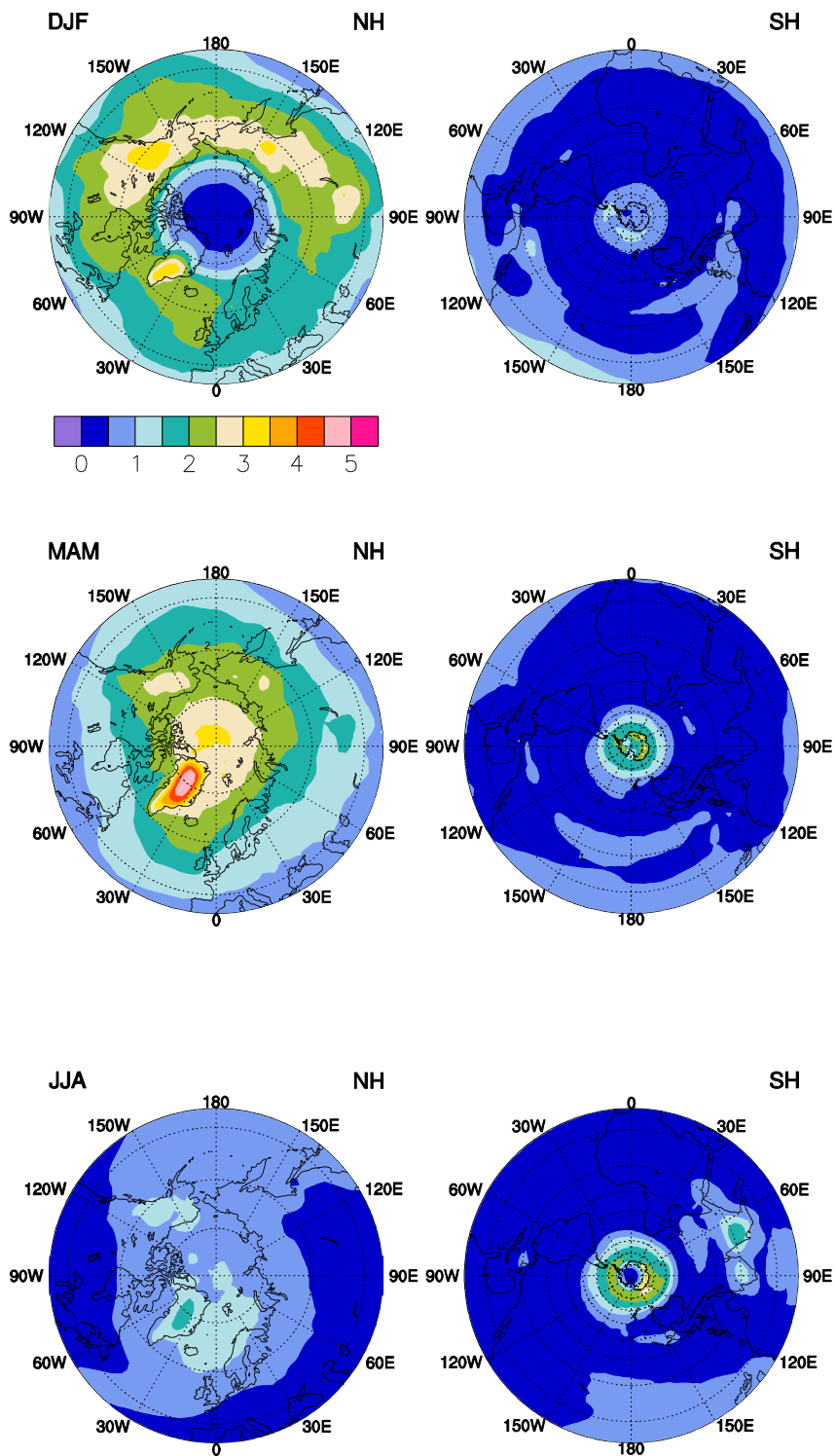
Figure 4. Vertically integrated BrO (10^{13} cm^{-2}) for the northern and southern hemispheres (NH, SH), averaged over winter (DJF), spring (MAM; March-April-May), and summer (JJA).
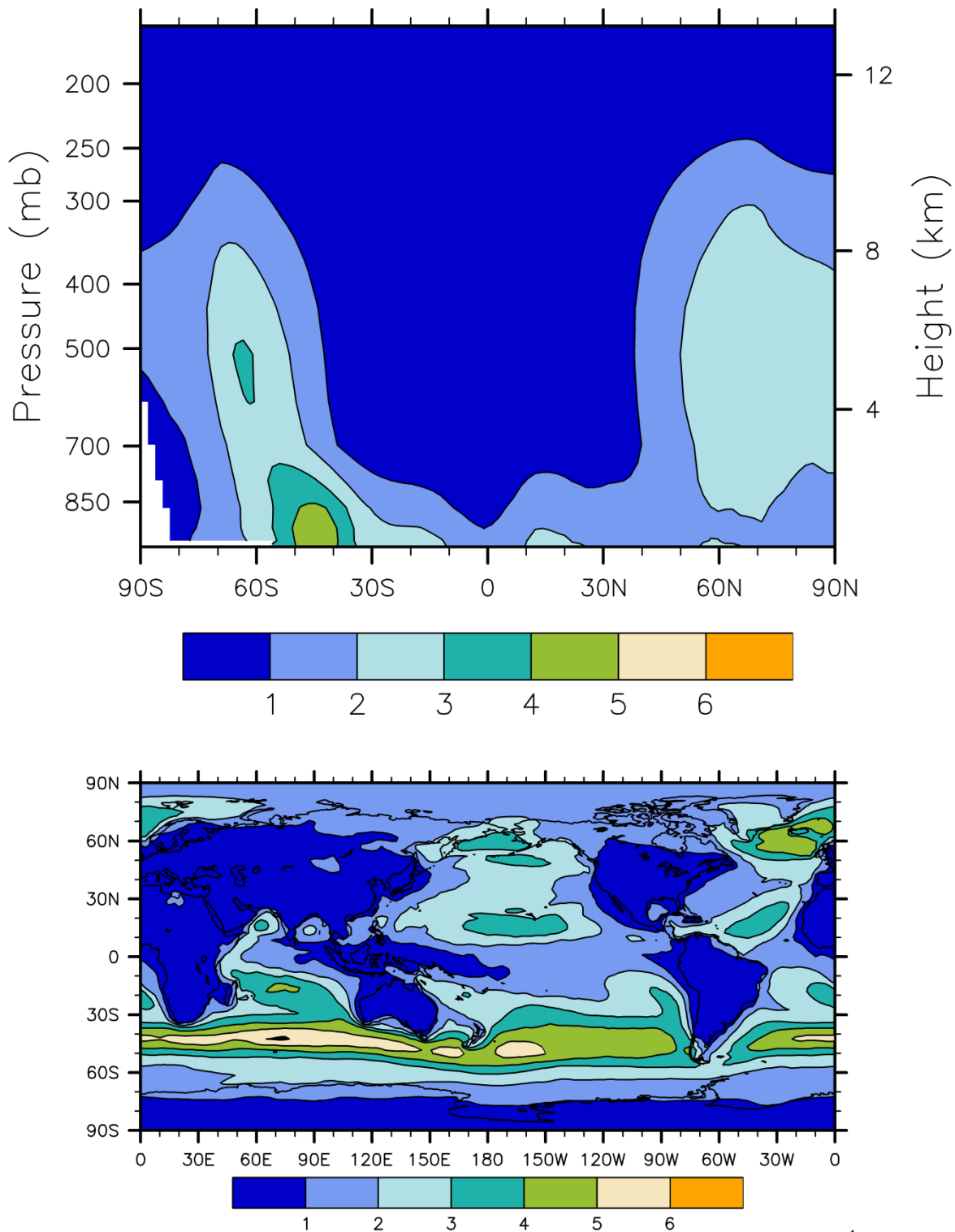
Figure 5. Annual mean a) zonal and b) PBL BrO mixing ratios (pmol mol^{-1}).
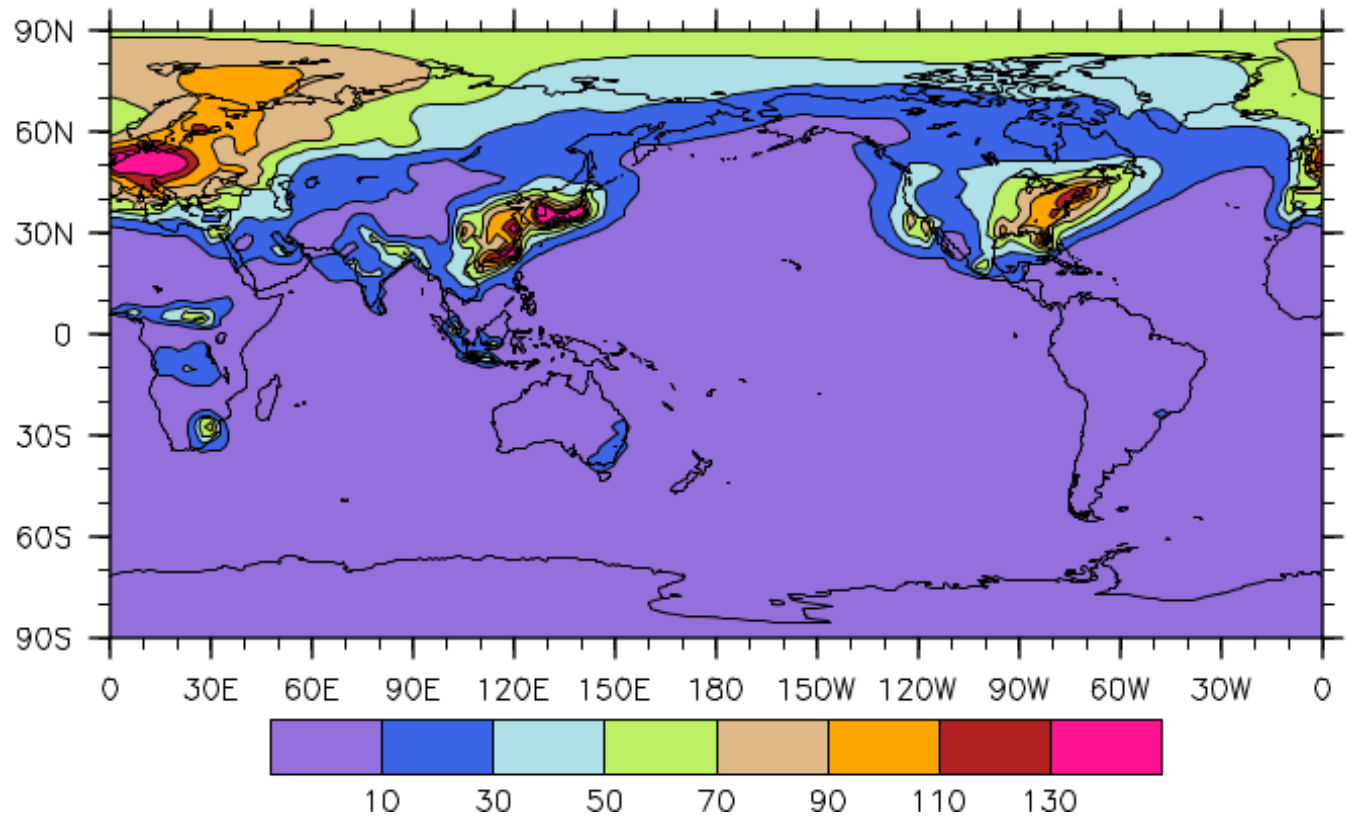
Figure 6. ANN-PBL ClNO$_2$ mixing ratio (pmol mol^{-1}).
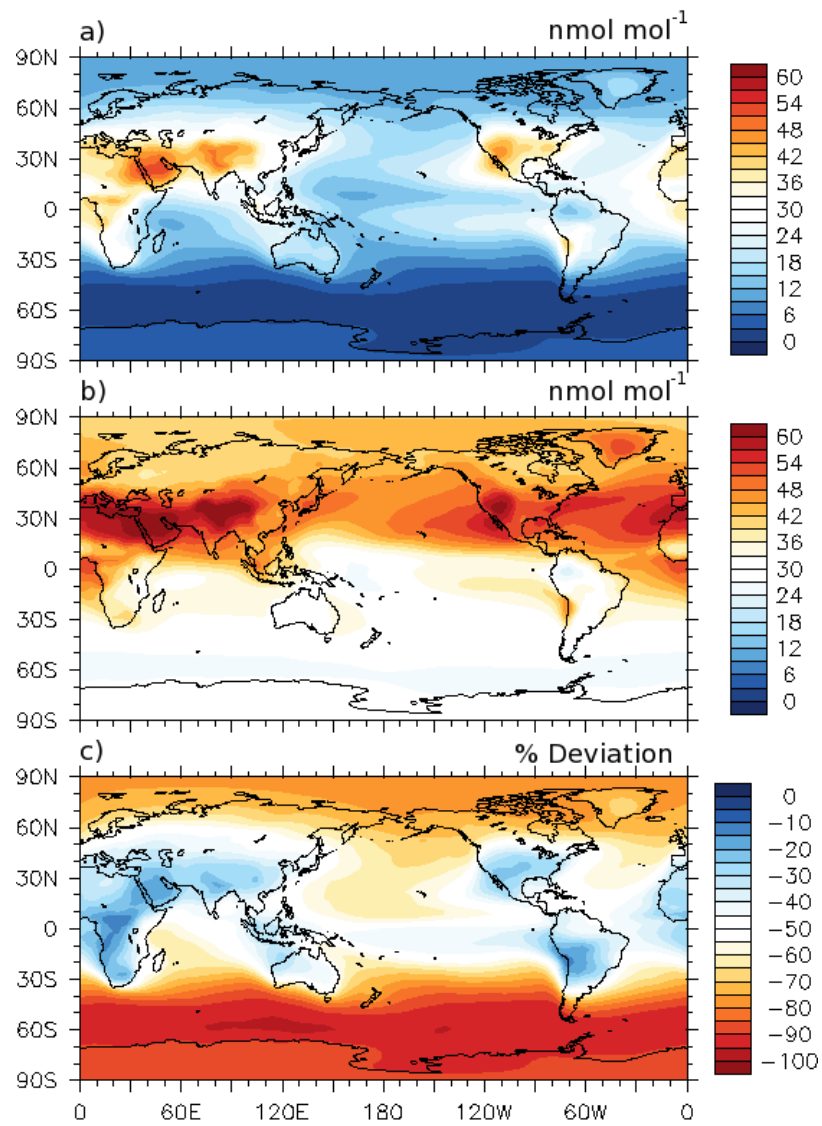
Figure 7 ANN-PBL O_3 (nmol mol^{-1}) for (a) *Hal* and (b) *NoHal*, and (c) the corresponding percent deviations.
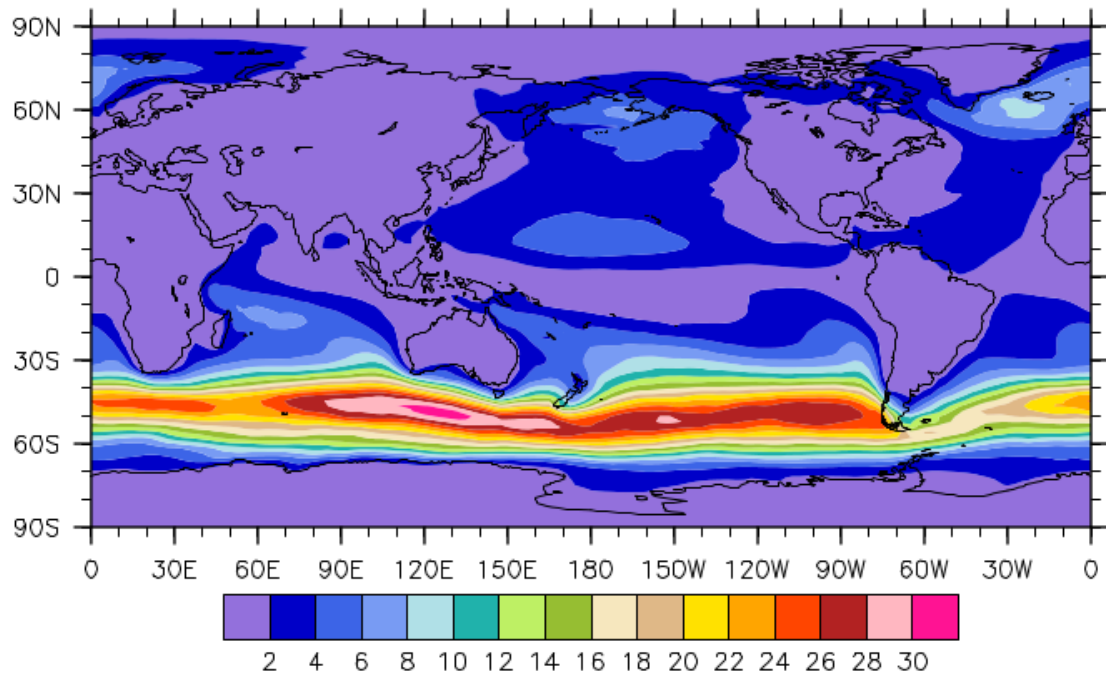
Figure 8. Percent contribution of Br + O_3 to total O_3 destruction in PBL (See Table 5).
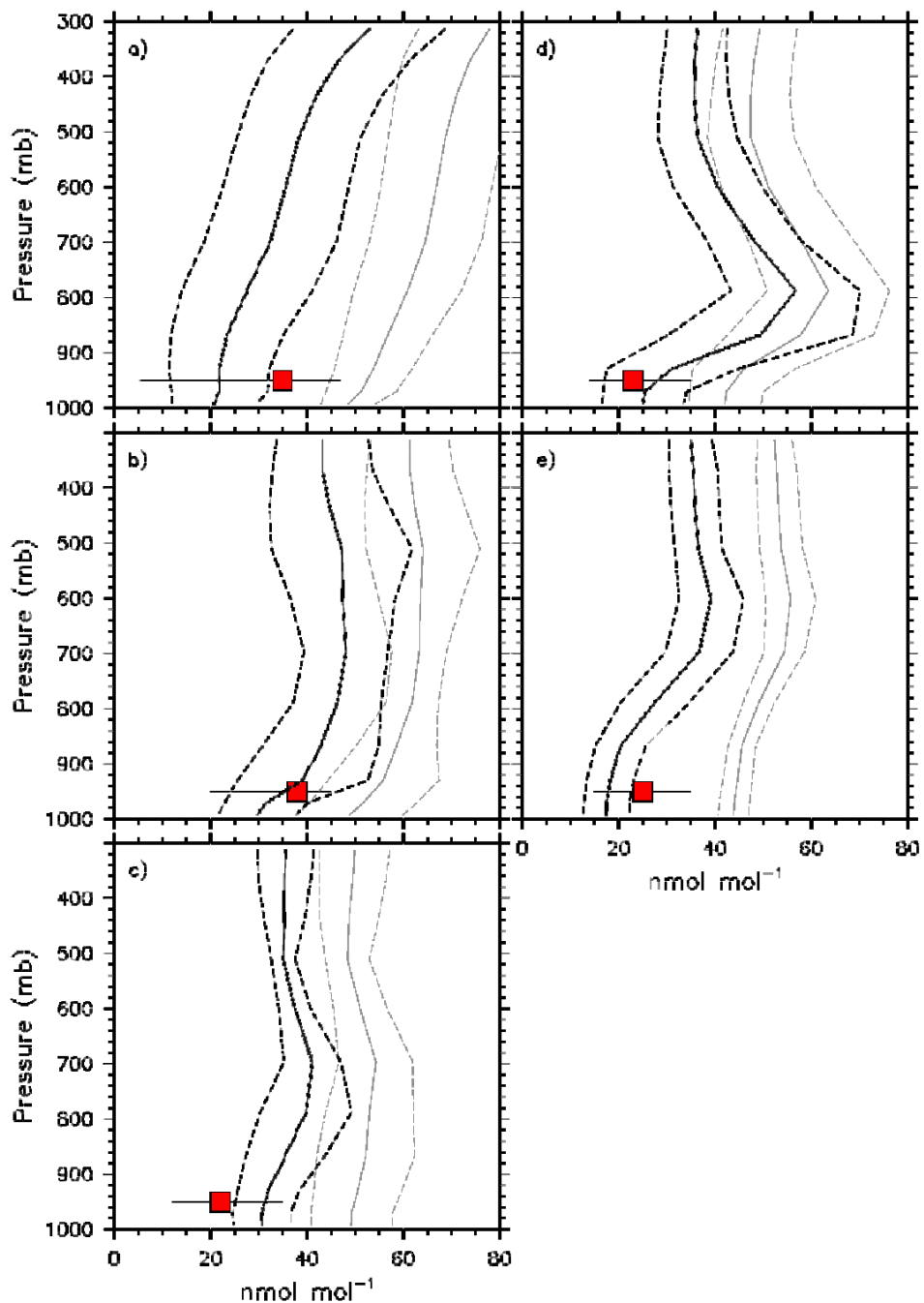
Figure 9. Vertical profiles of mean O_3 (nmol mol^{-1}; solid) and standard deviation (dashed) simulated with *Hal* (black) and *NoHal* (gray) and the corresponding mean O_3 measured in near-surface air (red boxes) for the (a) EURO, (b) NAFR, (c) ITCZ, and (d) SATL regimes as reported by Keene et al. (2009) and at (e) Hawaii (Pszenny et al., 2004). Bars depict measurement ranges.
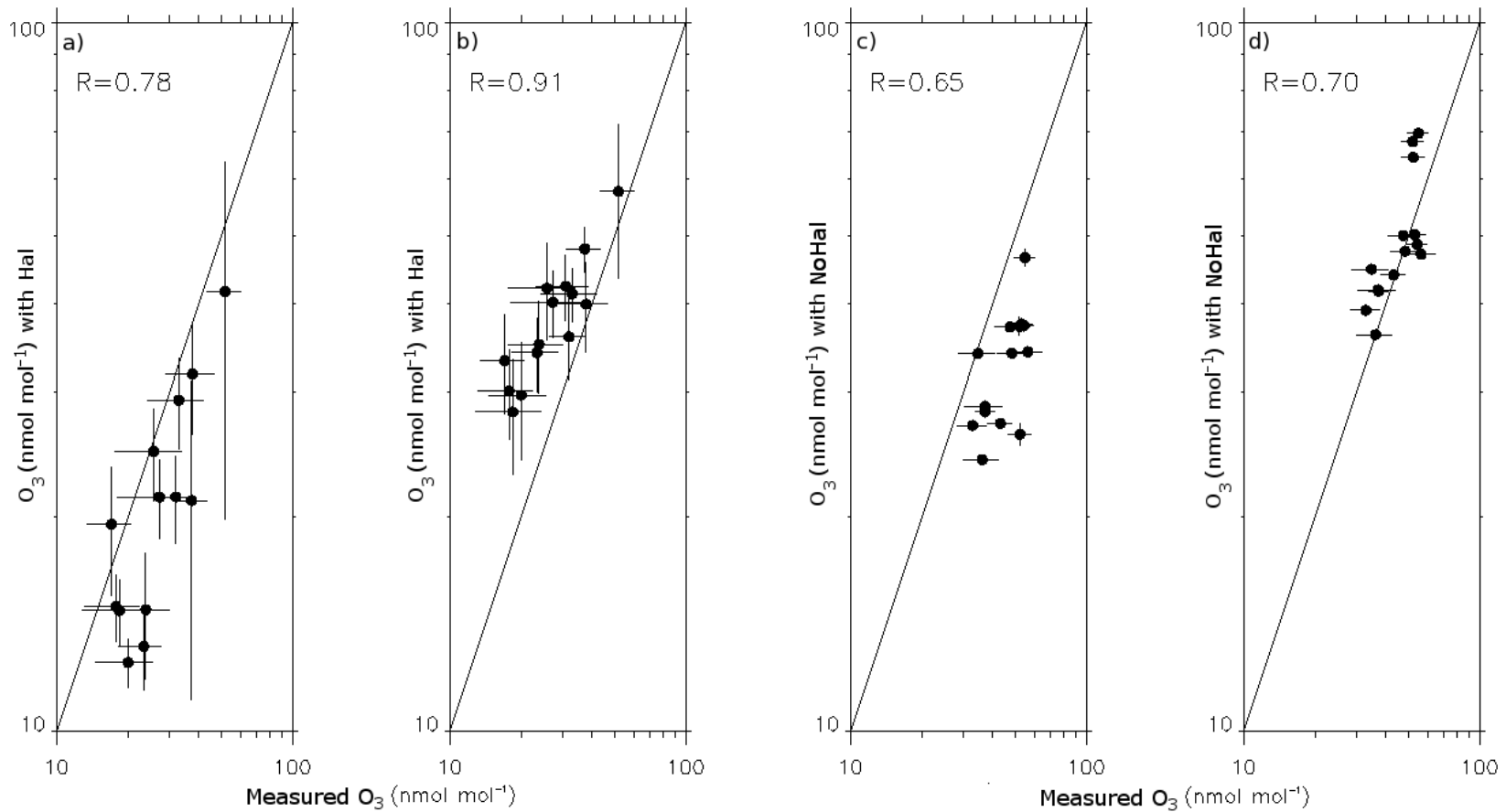
Figure 10. O_3 simulated in the PBL with (a) *Hal*, and(b) *NoHal* and at the 500 mb pressure height for (c) *Hal* and (d) *NoHal* versus the WOUDC O_3 climatology. Horizontal and vertical bars represent measurement and simulated standard deviations, respectively. The corresponding correlation coefficients (R) are shown.
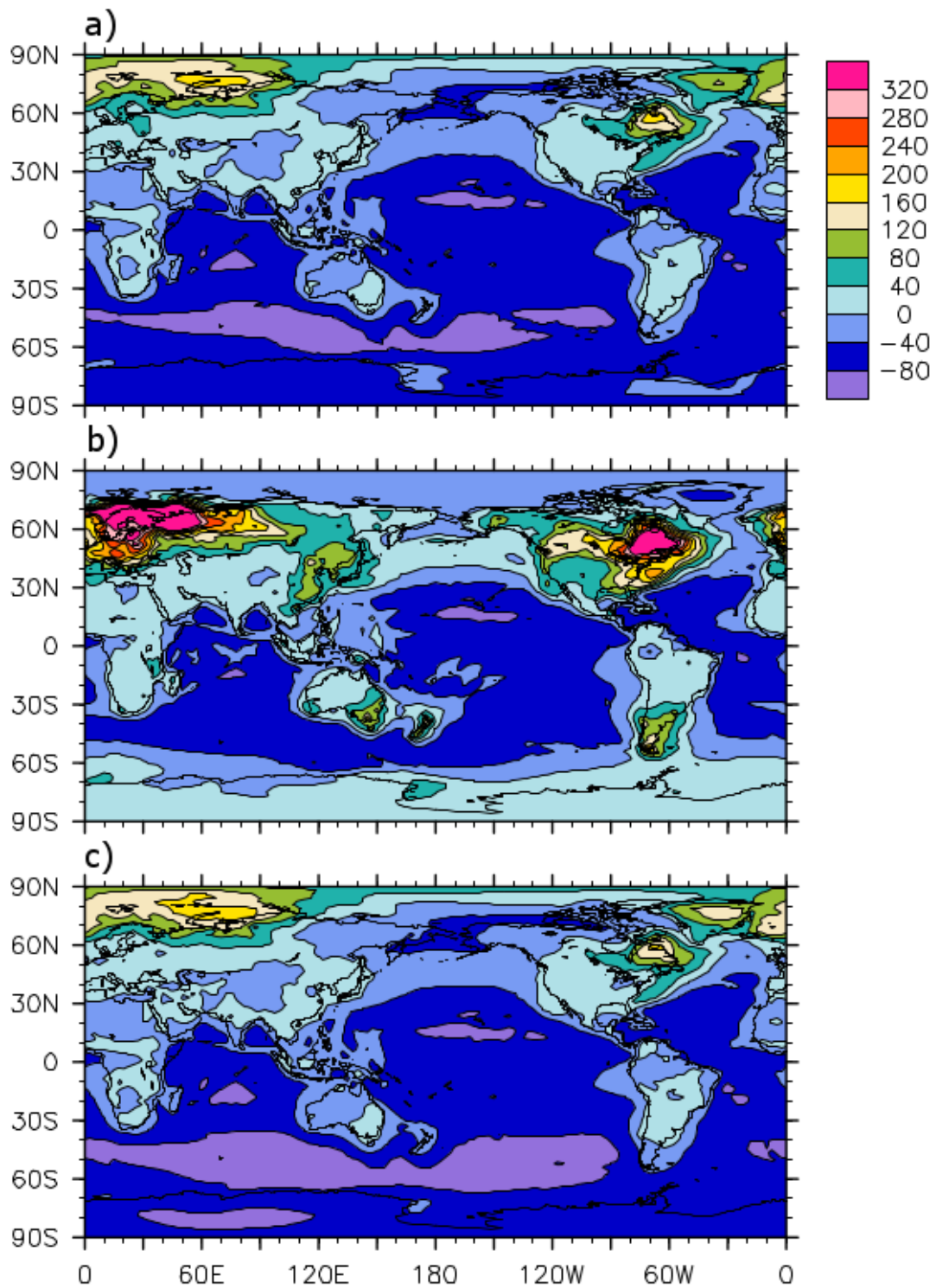
Figure 11. Percent deviation of a) NO_x (NO + NO_2), b) NO, and c) NO_2 in the PBL for *Hal* versus *NoHal* simulations. Dashed contour lines indicate negative contour values.

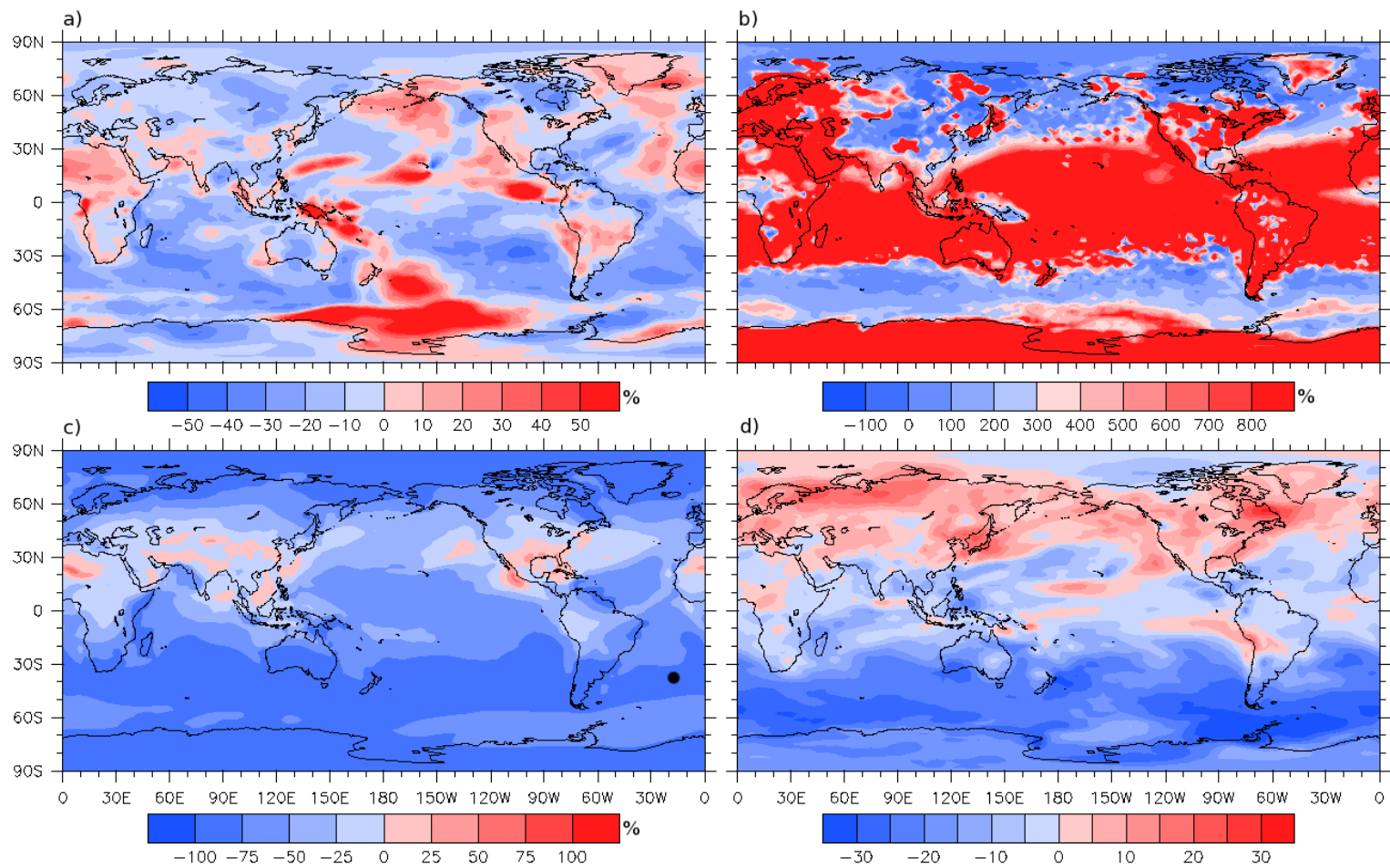Figure 12. Percent deviations in ANN-PBL (a) SO_2, (b) aggregate aqueous $S(IV)$ ($SO_{2(aq)}$, HSO_3^-, and SO_3^{2-} summed over the three simulated size bins), (c) DMS and (d) aggregate nss-SO_4.
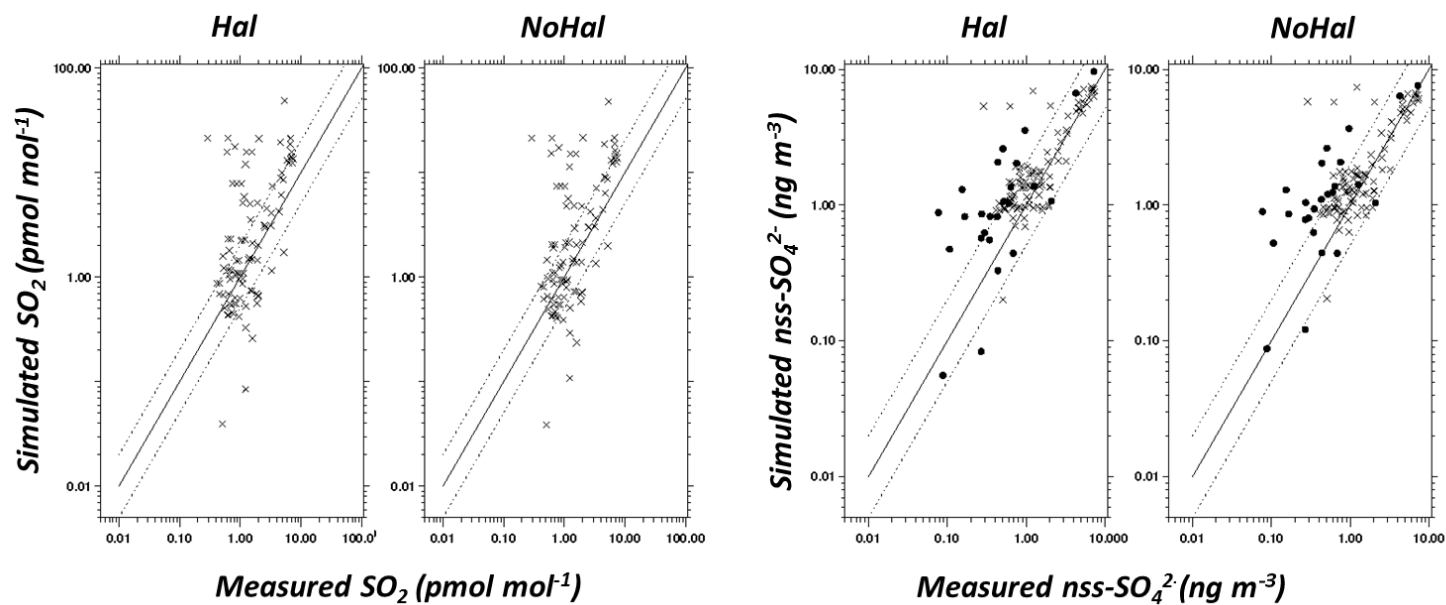
Figure 13. Mean SO$_2$ measured by the IMPROVE network at continental sites in the US versus mean SO$_2$ in the surface layer of the corresponding grid cell simulated with (a) *Hal* and (b) *NoHal*. Mean nss-SO$_4^{2-}$ measured at continental sites by the IMPROVE network (designated by x's) and at marine sites by Atmosphere-Ocean Chemistry Experiment (AEROCE, Savoie et al., 2002), U.S. Department of Energy as the Environmental Measurements Laboratory (DOE-EML), and the Sea-Air Exchange Experiment (SEAREX, Riley et al., 1989) (designated by dark circles) versus mean nss-SO$_4^{2-}$ in the surface layer of the corresponding grid cells simulated with (c) *Hal* and (d) *NoHal*.